Design of Highly Efficient Non-Noble Electrocatalysts for Water Reduction and Oxidation

A thesis presented for the award of the degree of

Doctor of Philosophy

from

University of Technology Sydney

By

Xingxing Yu, B. Sc., M.Sc.

July, 2020

CERTIFICATE OF ORIGINAL AUTHORSHIP

I, Xingxing Yu, certify that the work presented in this thesis has not previously been submitted for a degree nor has been submitted as part of requirements for a degree except as fully acknowledged within the text.

I also certify that the thesis has been written by me. Any help that I have received in my research work and the preparation of the thesis itself has been acknowledged. In addition, I certify that all information sources and literature used are indicated in the thesis.

This research is supported by an Australian Government Research Training Program.

Xingxing Yu

Production Note:
Signature removed prior to publication.

Sydney, Australia

July, 2020

DEDICATION

This thesis is dedicated to my family. Thank you all very much for your love and support.

ACKNOWLEDGEMENTS

During the period of my precious PhD study, I want to express my feeling of special gratitude for my supervisor, Professor Guoxiu Wang, for his kind help and guidance, continuous support and invaluable advice throughout the whole PhD study process. I am also very grateful and would like to thank Professor Shu-Hong Yu and Professor Min-Rui Gao, for their valuable guidance and unselfish help during my visit to University of Science and Technology of China (USTC). Besides, I also would like to appreciate Dr. Jane Yao for her kind help and essential support for our laboratory -- Centre for Clean Energy Technology (CCET).

My deep gratitude and special thanks are expressed to my kind and nice colleagues: Dr. Dawei Su, Dr. Bing Sun, Dr. Hao Liu, Dr. Huajun Tian, Dr. Xin Xu, Dr. Jinqiang Zhang, Dr. Yufei Zhao, Dr. Xin Guo, Dr. Weizhai Bao, Ms. Xiaochun Gao, Mr. Yi Chen, Mr. Kang Yan, Mr. Xiao Tang, Mr. Fan Zhang and Mr. Tianyi Wang from our CCET group for their kind friendly assistance and helpful collaboration. Furthermore, I also want to thank my lovely and nice friends in USTC, Dr. Yu Duan, Dr. Zi-You Yu, Mr. Xiao-Long Zhang, Mr. Fei-Yue Gao, Dr. Ya-Rong Zheng, Dr. Fei Zhou, Dr. Qiang Gao, Dr. Rui Wu, Dr. Lu-An Shi, Mr. Ren Liu, Mr. Peng-Peng Yang and Mr. Zhuang-Zhuang Niu, Miss Li-Ping Chi, Mr. Shuai Qin and Mr. Zhi-Zheng Wu from Professor Yu's and Professor Gao's groups. Thanks for their unselfish help and valuable collaboration, I really appreciate the good memories in USTC.

Additionally, I want to express my appreciation to Dr. Ronald Shimmon, Dr. Linda Xiao, and all the staffs from Faculty of Science for their administrative and technical support. Thanks for the DFT assistance received from Dr. Peng Li from Nanjing University of

Aeronautics and Astronautic and Professor Chenghua Sun from Swinburne University of Technology. The financial support from UTS to help me process my research work during the process of my PhD study are highly appreciated.

I also want to exhibit the grateful feeling to my best friends: Yixiao Xi, Yao Yao, Mengjiao Wang, Qing Li, Peipei Li, Jiayan Liao and Haiyan Chen. You are the warm light during my life to help me go through the difficulties and tribulations. Finally, I also would like to say thanks to all the members of my family. Thanks for your support throughout the whole PhD study and also my life in general, especially my brother for your understanding and tolerant character no matter how bad my temper. I love you all and I wish all good happens in your life.

Xingxing Yu

RESEARCH PUBLICATIONS

1. **X. Yu**, Z. Yu, X. Zhang, Y. Zheng, Y. Duan, Q. Gao, R. Wu, B. Sun, M. Gao, G. Wang, S. Yu, "Superaerophobic" Nickel Phosphide Nanoarray Catalyst for Efficient Hydrogen Evolution at Ultrahigh Current Densities, ***J. Am. Chem. Soc*.., 2019**, 141, 18, 7537-7543.

2. **X. Yu**, Z. Yu, X. Zhang, P. Li, B. Sun, X. Gao, K. Yan, H. Liu, Y. Duan, M. Gao, G. Wang, S. Yu, Highly Disordered Cobalt Oxide Nanostructure Induced by Sulfur Incorporation for Efficient Overall Water Splitting, ***Nano Energy*, 2020**, 71, 104652.

3. X. Zhang, S. Hu, Y. Zheng, R. Wu, F. Gao, P. Yang, Z. Niu, C. Gu, **X. Yu**, X. Zheng, C. Ma, X. Zheng, J. Zhu, M. Gao, S. Yu, Polymorphic Cobalt Diselenide as Extremely Stable Electrocatalyst in Acidic Media via a Phase-mixing Strategy, ***Nat. Commun.*, 2019**, 5338.

4. P. Yang, X. Zhang, F. Gao, Y. Zheng, Z. Niu, **X. Yu**, R. Liu, Z. Wu, S. Qi, L. Chi, Y. Duan, T. Ma, X. Zheng, J. Zhu, H. Wang, R. Gao, S. Yu, Protecting Copper Oxidation State via Intermediate Confinement for Selective CO_2 Electroreduction to C^{2+} Fuels, ***J. Am. Chem. Soc*.., 2020**, 142, 13, 6400-6408.

TABLES OF CONTENTS

LIST OF FIGURES

LIST OF TABLES

ABSTRACT

To satisfy the increasing energy demand and solve the global warming issue, renewable clean energy sources were in the urgent requirement. Hydrogen energy was regarded as the most potential clean energy suppliers. Electrocatalytic water splitting as one of the most promising approach for hydrogen production, has been rapidly blossomed. Tremendous efforts have been devoted into the electrocatalysts' development. However, the design of highly efficient non-noble electrocatalysts for large-scale hydrogen production was still a tough challenge. In the doctoral work, a series of non-noble metal electrocatalysts were prepared and investigated.

In the first project, we prepared the "superaerophobic" Ni_2P nanoarray catalyst grown on a nickel foam substrate. The Ni_2P catalysts demonstrate an outstanding electrocatalytic activity and stability in alkaline electrolyte. Their high catalytic activities can be attributed to the favorable electron transfer, superior intrinsic activity and the intimate connection between the nanoarrays and their substrate. Moreover, the unique "superaerophobic" surface feature of the Ni_2P nanoarrays enables a remarkable capability to withstand internal and external forces and timely release the in-situ generated vigorous H_2 bubbles at large current densities (such as > 1000 mA cm^{-2}). Our results highlight that an aerophobic structure is essential to catalyze large-scale gas evolution.

The second project concentrates on tuning the internal structure of nanomaterials to boost their intrinsic catalytic properties. We reported an incorporation of sulfur ion into crystalline cobalt oxide (S-CoO_x) to create structural disorder via a facile room-temperature ion exchange strategy. Compared with its crystalline form, the disorder in S-CoO_x catalyst endows it remarkable catalytic activities for hydrogen evolution reaction (HER) and oxygen evolution reaction (OER). The water electrolyser adopting S-CoO_x as cathode and anode requires mere 1.63 V to reach 10 mA cm^{-2} in 1 M KOH. Charaterizations and analysis demonstrate that the enhanced electrocatalytic properties could be attributed to increased low oxygen coordination, more defect sites and modified electron densities characteristics. This work provides the new insight on designing structural disordered catalysts for energy storage areas.

In this thesis, the two projects are both about the design of the freestanding and three-dimensional materials. Their advantages could be concluded into two aspects. One is the more effective electron and mass transfer pathway, providing the effective intrinsic catalyst properties. Other is the solid connection, guaranteeing their stabilities even at the high current densities. These findings spotlight the usage of freestanding catalysts in the energy storage and conversion devices.

Chapter 1 Introduction

1.1 Background

Due to the rapidly increasing intense concerns on global warming, deteriorative environmental pollutions and incremental energy crisis, the demand for clean and sustainable energy supplies becomes extremely urgent.[1-3] Current dominating energy resources still depend on the traditional fossil fuels, including coal, petroleum and natural gas. However, the limited stock, global warming effect and non-renewable nature make the fossil fuels to be the inferior choices during energy systems.[4,5] To diminish the usage of fossil fuels and address energy crisis, the sustainable energy sources based on clean, carbon-neutral, renewable and abundant properties has attracted the increasing research interest.[6,7] Hydrogen as one of the most potential new energy sources, is a clean and green energy carrier alternative. However, seeking for an efficient approach to realize the large-scale hydrogen production was still a formidable challenge.[8-10] Coal gasification and partial oxidation as the current major commercial processes to produce hydrogen are suffering from CO_2 emissions and greenhouse effect.[11] Therefore, it is an urgent need to explore a more environmentally friendly approach to produce hydrogen.

In order to provide a practicable approach for achieving this objective, various research fields have been developed.[12-17] Electrocatalytic water splitting provides a sustainable and desirable access for hydrogen generation because the only consumables is water. However, several major technical hurdles such as inactive property, low efficiency, poor stability and high cost are still difficult to solve. Catalysts are vital elements in many important scientific and technological areas, thus the design of affordable and active catalytic materials to

accelerate electrocatalytic water splitting systems was very important. The whole water splitting system consist of two half-reactions, which include hydrogen evolution reaction (HER) and oxygen evolution reaction (OER). Between the two half-reaction systems, OER activity is considered as a more complex and difficult process because of its four-electron transfer behavior. The sluggish kinetics caused by the higher energy barrier for O-H bond-breaking and the formation of O-O bond, makes OER activity the key part during electrocatalytic water splitting device. The Nernstian potentials (E) for H_2O/O_2 and H_2O/H_2 half-reactions are as followings, NHE is the normal hydrogen electrode:[11,18,19]

Water oxidation reaction: $O_2 + 4H^+ + 4e^- \rightarrow 2H_2O$ $E_{anodic} = 1.23\ V - 0.059 \cdot pH\ V$ vs. NHE (1)

Water reduction reaction: $4H^+ + 4e^- \rightarrow 2H_2$ $E_{cathodic} = 0\ V - 0.059 \cdot pH\ V$ vs. NHE (2)

Overall water splitting: $2H_2O \rightarrow 2H_2 + O_2$ $E_{rxn} = -1.23\ V$ (3)

Thus, seeking for the stable and efficient catalyst materials was the key items to accelerate electrocatalytic water splitting systems.

Currently, the highest active electrocatalysts to catalyze hydrogen evolution and oxygen generation during water splitting systems were mainly dependent on noble metals or noble metals compounds, such as Pt for HER and Ir, Ru oxides for OER, which severely limits the widespread energy supply due to their scarcity and high cost.[20-27] Hence, searching for the low-cost and earth-abundant catalysts has attracted the focus of research workers. In nature, oxygen gas could be generated during the photosystem process.[28-31] To analyze and figure out the chemistry mechanism for oxygen generation in the photosystem II, numerous efforts have been devoted. The Mn_4Ca-cluster was found to be effective for the catalytic

water oxidation.[32] This finding provides attracting and promising alternatives to noble metals for electrocatalytic water splitting using the design of low-cost and earth-abundant transition metal oxides or their compounds. In 2008, Nocera's group reported that a catalyst made of electrodeposited cobalt ion in KPi solution demonstrates a high catalytic performance in neutral environment.[18] Subsequently, the electrodeposited nickel-Bi film obtained under benign condition (pH 9.2), also shows the potential to efficiently catalyze oxygen generation.[33] Besides, other first-low transition metal oxides or compounds such as copper oxides, nickel oxides, cobalt oxides, iron metal compounds also have exhibited the effectively catalytic activities for water splitting.[19,34-39] Thus, the usage of transition metal compounds during catalytic water splitting system for the production of hydrogen and oxygen shows great potential. However, the electrocatalytic performances of these transition metal compounds still can't satisfy the requirement to replace the highly active noble metal catalysts.

In order to explore efficient strategies for the enhanced catalytic properties of transition metal materials during electrochemical water splitting, a variety of research efforts have been devoted. The reported research results demonstrate that the bi-metals or multifold metal catalysts usually show a better catalytic performance for oxygen generation or hydrogen production with the single metal materials as comparison.[38,40,41] Dai's group has reported a famous combination between nickel and iron, which has been explored to catalyze oxygen evolution under alkaline electrolyte. The special and unique Fe-Ni layered double hydroxide shows an excellent catalytic performance with a low required onset potential of ~1.45 V vs. RHE (reversible hydrogen electrode) where the current density is at ~ 5 mA cm^{-2} in the electrolyte of 1 M KOH.[42] Yao's group further broadened that the

coupling of the exfoliated Ni-Fe hydroxide nanosheet to the usage for both OER and HER.[43] This combination idea could be extended into various design routes, such as doping, anion or cation incorporation in the areas of transition metal oxides,[44, 58] (oxy)hydroxides,[44] chalcogenides,[45] phosphides,[46] nitrides,[47] or other types.

To improve the insufficient activity of non-noble metal catalysts, carbon materials were also the excellent choices. Carbon, as the supporting material, has been widely used to accelerate electron or proton transfer and enhance the conductivity, which were also the crucial factors during electrochemical systems. [48,49] Numerous research studies exhibit that the non-noble metals catalysts connected with carbon substrate materials demonstrate a preferable catalytic performance for water splitting.[50-54] The synthesis of the hybrid materials to form strongly coupled non-metals catalysts on the carbon materials, was usually prepared via the direct nucleation, growth and anchoring of non-noble metal materials onto the functional carbon substrates.[19,55,56] This preparation technique provides strong chemical attachment and electrical coupling, thus leading to beneficial catalytic activities.

To fasten the powder catalyst materials onto the conductive substrates (such as carbon paper or glassy carbon electrode), the polymer binders (such as Nafion) without any catalytic performance were added, inevitably reducing the mass transfer contact between the catalysts and electrolyte, thus diminishing the catalytic properties of the used catalysts. Meanwhile, the three-dimensional catalyst electrodes provide the direct connection between the catalysts and their substrate without any influence of binder addition, thus the three-dimensional catalysts were boosting in rapid and vigorous development stage. The strategy to directly integrate the active materials onto substrates affords a fortified interface

connection, thus providing more advantages to catalyze water splitting. The improved mass and electron transfer and enhanced tight interface contact properties of three-dimensional freestanding catalyst materials exhibit the enhanced catalytic activities during the water splitting systems. For example, Zhang's group has prepared a three-dimensional material electrocatalyst consisting of internal carbon paper, carbon tube and external cobalt-sulfide which exhibits an excellent catalysis for both OER and HER.[3] The paramount property of the freestanding catalyst could be attributed to the retentive intrinsic catalytic nature during the catalysis process, also resulting in a commendable stability. Thus, three-dimensional catalysts might have huge potential to be used at high current densities where the gas bubbles were rapidly produced. The routes and methods to establish freestanding materials also could be widely adopted in various energy fields.

1.2 Aims of the Research

Electrocatalytic water splitting was one of the most potential approaches for the clean energy hydrogen production. To realize the large-scale hydrogen production or improve HER activities, diversified methods have been utilized. In this PhD thesis, to reduce costs, the low-cost and earth-abundant transition metal compounds were chosen to be further studied. To eliminate of the influence from the polymer binders, we mainly focus on the design of freestanding three-dimensional catalytic materials. In the first project, the nickel phosphide nanoarray which was grown on the nickel foam substrate was used as the electrocatalyst during water reduction reaction to produce hydrogen under alkaline electrolyte. The nickel phosphide was selected as the electrocatalyst which was based on the reported highly active intrinsic catalytic properties of transition metal phosphides. Although the research studies about the usage of transition metal phosphides during

electrocatalytic water splitting systems for HER or OER under alkaline or acidic electrolytes have been widely reported. The dominating research studies were basically staying in the experimental period at low current densities. To realize the applications of the electrocatalysts at high current densities was a challenging issue and was also vital to proceed the industrialization of hydrogen production. Hence, we wanted to establish a catalyst design which can be active to catalyze hydrogen generation even at high current densities.

To realize this project aim, the precursor was firstly achieved via the direct reaction between $(NH_4)_2HPO_4$ and the clean nickel foam to build a nanowire array structure during a facile hydrothermal process. Then the precursor was transferred into nickel hydroxide phase during another hydrothermal strategy under alkaline solution when the hydrothermal temperature is higher than 100 ^oC. Besides, the morphology has also changed from the simple nanowire arrays into the unique nickel hydroxide nanoarrays which consist of nanosheet arrays and nanowire arrays, the nanosheet arrays were uniformly grown on the nanowire arrays. The nickel phosphide was achieved via a facile phosphorization annealing process, using the as-prepared nickel hydroxide nanoarrays and sodium hypophosphite monohydrate as the reactants. The nanoarray structure of nickel phosphide was retained from the nickel hydroxide nanoarrays. The contact angle test demonstrates that a "superaerophobic" surface structure was formed on the nickel phosphide nanoarrays. The electrochemical hydrogen evolution system was constructed with the unique nickel phosphide as the catalyst. This Ni_2P/NF catalyst shows highly active catalytic activities and the excellent stabilities even at large current densities (such as > 1000 mA cm^{-2}). The two-electrode water splitting systems consist of Ni_2P/NF and Ni-Fe layered double hydroxide

(LDH) as the cathode and anode electrodes. Their efficient electrocatalytic performance further reveals the potential application of the unique "superaerophobic" structure at high current densities. This project spotlights the design of "superaerophobic" surface structure as the promising path for hydrogen industrialization.

Besides the design of the unique surface structure, we were also interested in the study of internal structure transfer and control during the catalyst materials. Thus, in the second project, we chose the low-cost transition metal compound -- cobalt oxide as our research objective. To tune its internal structure, electronegative sulfur ion was incorporated into the high crystalline cobalt oxide via a room-temperature ion exchange method. The resultant phenomena reveal that an interesting transfer process happens during sulfur incorporation. After sulfur incorporation, the long-range lattice arrangement in crystalline cobalt oxide was broken, the disordered lattice distribution was formed in the sulfur ion incorporated cobalt oxide (S-CoO_x) catalyst accompanied with the enhanced defect sited and more low oxygen coordination. Density functional theory (DFT) calculation also show a preferable electronic state was also generated. The highly disordered S-CoO_x exhibits the superior catalytic properties for both HER and OER when was compared with its crystalline cobalt oxide. This project shows a facile structural disorder approach during the advanced electrocatalyst design for the energy storage and conversion systems. The above results provide the guidance for the applications of unique morphology surface design or structure transfer control during electrocatalytic water splitting systems or other energy storage and conversion fields.

1.3 Thesis Structure

For the objective to enhance the electrocatalytic water splitting system for the high-efficiency hydrogen production, the design of unique morphology or induced structural disorder was utilized to boost the catalytic properties of the low-cost and earth-abundant transition metal compounds. To explore the influence of the prepared catalyst design towards the catalytic hydrogen evolution or overall water splitting system, a series of control experiments and their influence relationship on the catalytic activities were operated. Various structural analysis and characterizations were also investigated for the deep understanding of the achieved catalysts. In this doctoral study, the outline of each chapter is briefly listed as the followings:

1) Chapter 1 gives the introduction of the energy crisis background, the various approaches to produce clean hydrogen energy, the mechanism in two-half reactions during electrocatalytic water splitting system and the development of the catalysts, also uncovers the objective and significance of our research work.
2) Chapter 2 displays a literature review about the research development of recent water electrolysis, the challenging dilemma in current water electrolysis, the large-scale synthesis of electrode design, and the design of electrodes used at high current densities during the hydrogen industrialization.
3) Chapter 3 reveals the various analysis and characterization methods used in the experimental parts. Material synthesis and preparation strategies were also included.
4) Chapter 4 presents the synthesis of the unique "superaerophobic" nickel phosphide nanoarrays. The preparation of the freestanding precursor, and the whole phase and morphology transfer process from the precursor to nickel hydroxide, then turn in nickel

phosphide. The detailed structure and morphology analysis and characterizations of the obtained samples. The "superaerophobic" property was examined via the contact angle test.

5) Chapter 5 investigates the electrocatalytic HER activities using nickel phosphide nanoarrays under alkaline electrolyte, which were operated at high current densities. The two-electrode water splitting device was also constructed to simulate the practical hydrogen production.
6) Chapter 6 demonstrates the disordered structure transfer from crystalline cobalt oxide to the disordered S-CoO_x via a room-temperature ion exchange strategy. Experimental and theoretical analysis were utilized to uncover the internal change in the S-CoO_x catalyst, and its electrochemical properties were also investigated.
7) Chapter 7 summarizes the research works in this doctoral thesis and offers some accessible routes for the morphology and structure design to develop newly advanced catalysts for water splitting system or other energy areas in the future scope.

1.4 References

1. Sivula, K., F. Le Formal, and M. Gratzel, *Solar water splitting: Progress using hematite (alpha-Fe_2O_3) photoelectrodes.* Chemsuschem, 2011. **4**(4): p. 432-449.
2. Swaminathan, J., R. Subbiah, and V. Singaram, *Defect-rich metallic titania ($TiO_{1.23}$)-An efficient hydrogen evolution catalyst for electrochemical water splitting.* Acs Catal., 2016. **6**(4): p. 2222-2229.
3. Wang, J., et al., *Integrated three-dimensional carbon paper/carbon tubes/cobalt-sulfide sheets as an efficient electrode for overall water splitting.* Acs Nano, 2016. **10**(2): p. 2342-2348.

4. Dubale, A.A., et al., *A highly stable CuS and CuS-Pt modified Cu_2O/CuO heterostructure as an efficient photocathode for the hydrogen evolution reaction.* J. Mater. Chem. A, 2016. **4**(6): p. 2205-2216.

5. Lu, Q.P., et al., *2D transition-metal-dichalcogenide-nanosheet-based composites for photocatalytic and electrocatalytic hydrogen evolution reactions.* Adv. Mater., 2016. **28**(10): p. 1917-1933.

6. Yan, Z.P., et al., *Noble-metal-free $Ni(OH)_2$-modified CdS/reduced graphene oxide nanocomposite with enhanced photocatalytic activity for hydrogen production under visible light irradiation.* J. Phys. Chem. C, 2014. **118**(40): p. 22896-22903.

7. Zhang, T., et al., *Hybrids of cobalt/iron phosphides derived from bimetal-organic frameworks as highly efficient electrocatalysts for oxygen evolution reaction.* Acs Appl. Mater. Interf., 2017. **9**(1): p. 362-370.

8. Chen, J., et al., *$MgCl_2$ promoted hydrolysis of MgH_2 nanoparticles for highly efficient H_2 generation.* Nano Energy, 2014. **10**: p. 337-343.

9. Kato, H., K. Asakura, and A. Kudo, *Highly efficient water splitting into H_2 and O_2 over lanthanum-doped $NaTaO_3$ photocatalysts with high crystallinity and surface nanostructure.* J. Am. Chem. Soc., 2003. **125**(10): p. 3082-3089.

10. Kato, H. and A. Kudo, *Water splitting into H_2 and O_2 on alkali tantalate photocatalysts $ATaO_3$ (A = Li, Na, and K).* J. Phys. Chem. B, 2001. **105**(19): p. 4285-4292.

11. Tang, C., et al., *Fe-doped CoP nanoarray: A monolithic multifunctional catalyst for highly efficient hydrogen generation.* Adv. Mater., 2017. **29**(2): p. 1602441.

12. Ao, C.H. and S.C. Lee, *Indoor air purification by photocatalyst TiO_2 immobilized on an activated carbon filter installed in an air cleaner.* Chem. Engin. Sci., 2005. **60**(1): p. 103-109.

13. Armand, M. and J.M. Tarascon, *Building better batteries.* Nature, 2008. **451**(7179): p. 652-657.

14. Cai, X.Y., et al., *Graphitic-C_3N_4 hybridized N-doped $La_2Ti_2O_7$ two-dimensional layered composites as efficient visible-light-driven photocatalyst.* Appl. Catal. B-Environ., 2017. **202**: p. 191-198.

15. Dempsey, J.L., et al., *Hydrogen evolution catalyzed by cobaloximes.* Acc. Chem. Res., 2009. **42**(12): p. 1995-2004.

16. Tarascon, J.M. and M. Armand, *Issues and challenges facing rechargeable lithium batteries.* Nature, 2001. **414**(6861): p. 359-367.

17. Turchi, C.S. and D.F. Ollis, *Photocatalytic degradation of organic-water contaminants - Mechanisms involving hydroxyl radical attack.* J. Catal., 1990. **122**(1): p. 178-192.

18. Kanan, M.W. and D.G. Nocera, *In situ formation of an oxygen-evolving catalyst in neutral water containing phosphate and Co^{2+}.* Science, 2008. **321**(5892): p. 1072-1075.

19. Liang, Y.Y., et al., *Co_3O_4 nanocrystals on graphene as a synergistic catalyst for oxygen reduction reaction.* Nat. Mater., 2011. **10**(10): p. 780-786.

20. Duan, L.L., et al., *A molecular ruthenium catalyst with water-oxidation activity comparable to that of photosystem II.* Nat. Chem., 2012. **4**(5): p. 418-423.

21. Guayaquil-Sosa, F., et al., *Photocatalytic hydrogen production using mesoporous TiO_2 doped with Pt.* Appl. Catal. B-Environ., 2017. **211**: p. 337-348.

22. Lee, Y., et al., *Synthesis and activities of rutile IrO_2 and RuO_2 nanoparticles for oxygen evolution in acid and alkaline solutions.* J. Phys. Chem. Lett., 2012. **3**(3): p. 399-404.

23. Reier, T., M. Oezaslan, and P. Strasser, *Electrocatalytic oxygen evolution reaction (OER) on Ru, Ir, and Pt catalysts: A comparative study of nanoparticles and bulk materials.* Acs Catal., 2012. **2**(8): p. 1765-1772.

24. Concepcion, J.J., et al., *Making oxygen with ruthenium complexes.* Acc. Chem. Res., 2009. **42**(12): p. 1954-1965.

25. Duan, L.L., et al., *Isolated seven-coordinate Ru(IV) dimer complex with [HOHOH]- bridging ligand as an intermediate for catalytic water oxidation.* J. Am. Chem. Soc., 2009. **131**(30): p. 10397-+.

26. Tee, S.Y., et al., *Amorphous ruthenium nanoparticles for enhanced electrochemical water splitting.* Nanotechnology, 2015. **26**(41): p. 415401.

27. Yamada, H., et al., *Mechanisms of water oxidation catalyzed by the cis, cis-$[(bpy)_2Ru(OH_2)]_2O^{4+}$ ion.* J. Am. Chem. Soc., 2004. **126**(31): p. 9786-9795.

28. Bard, A.J. and M.A. Fox, *Artificial photosynthesis - Solar splitting of water to hydrogen and oxygen.* Acc. Chem. Res., 1995. **28**(3): p. 141-145.

29. Gust, D., T.A. Moore, and A.L. Moore, *Solar fuels via artificial photosynthesis.* Acc. Chem. Res., 2009. **42**(12): p. 1890-1898.

30. McEvoy, J.P. and G.W. Brudvig, *Water-splitting chemistry of photosystem II.* Chem. Rev., 2006. **106**(11): p. 4455-4483.

31. Nocera, D.G., *The artificial leaf.* Acc. Chem. Res., 2012. **45**(5): p. 767-776.

32. Barber, J., *Photosynthetic energy conversion: natural and artificial.* Chem. Soc. Rev., 2009. **38**(1): p. 185-196.

33. Dinca, M., Y. Surendranath, and D.G. Nocera, *Nickel-borate oxygen-evolving catalyst that functions under benign conditions.* P. Natl. Acad. Sci. U. S. A., 2010. **107**(23): p. 10337-10341.

34. Cesar, I., et al., *Translucent thin film Fe_2O_3 photoanodes for efficient water splitting by sunlight: Nanostructure-directing effect of Si-doping.* J. Am. Chem. Soc., 2006. **128**(14): p. 4582-4583.

35. Du, P.W. and R. Eisenberg, *Catalysts made of earth-abundant elements (Co, Ni, Fe) for water splitting: Recent progress and future challenges.* Energy Environ. Sci., 2012. **5**(3): p. 6012-6021.

36. Hara, M., et al., *Cu_2O as a photocatalyst for overall water splitting under visible light irradiation.* Chem. Commun., 1998(3): p. 357-358.

37. Li, Y.Y., et al., *Mechanism of water oxidation catalyzed by a mononuclear manganese complex.* Chemsuschem, 2017. **10**(5): p. 903-911.

38. Sun, X.H., et al., *A general approach to synthesise ultrathin NiM (M = Fe, Co, Mn) hydroxide nanosheets as high-performance low-cost electrocatalysts for overall water splitting.* J. Mater. Chem. A, 2017. **5**(17): p. 7769-7775.

39. Yu, X.X., et al., *Direct growth of porous crystalline $NiCo_2O_4$ nanowire arrays on a conductive electrode for high-performance electrocatalytic water oxidation.* J. Mater. Chem. A, 2014. **2**(48): p. 20823-20831.

40. Maruthapandian, V., et al., *Study of the oxygen evolution reaction catalytic behavior of $Co_xNi_{1-x}Fe_2O_4$ in alkaline medium.* Acs Appl. Mater. Interf., 2017. **9**(15): p. 13132-13141.

41. Zhang, M.W., et al., *Ni-Co layered double hydroxides cocatalyst for sustainable oxygen photosynthesis.* Appl. Catal. B-Environ., 2017. **210**: p. 454-461.

42. Gong, M., et al., *An advanced Ni-Fe layered double hydroxide electrocatalyst for water oxidation.* J. Am. Chem. Soc., 2013. **135**(23): p. 8452-8455.

43. Jia, Y., et al., *A heterostructure coupling of exfoliated Ni-Fe hydroxide nanosheet and defective graphene as a bifunctional electrocatalyst for overall water splitting.* Adv. Mater., 2017. **29**(17): p.1700017.

44. Bode, H., K. Dehmelt, and J. Witte, *Zur kenntnis der nickelhydroxidelektrode—I.Über das nickel (II)-hydroxidhydrat.* Electrochim. Acta, 1966. **11**(8): p. 1079-1087.

45. Lai, C.-H., M.-Y. Lu, and L.-J. Chen, *Metal sulfide nanostructures: synthesis, properties and applications in energy conversion and storage.* J. Mater. Chem., 2012. **22**(1): p. 19-30.

46. Kupka, J. and A. Budniok, *Electrolytic oxygen evolution on Ni-Co-P alloys.* J. Appl. Electrochem., 1990. **20**(6): p. 1015-1020.

47. Chen, P., et al., *Metallic Co_4N porous nanowire arrays activated by surface oxidation as electrocatalysts for the oxygen evolution reaction.* Angew. Chem. Int. Ed., 2015. **54**: p. 14710-14714.

48. Sun, Y.Q., Q.O. Wu, and G.Q. Shi, *Graphene based new energy materials.* Energy Environ. Sci., 2011. **4**(4): p. 1113-1132.

49. Wang, P.F., et al., *The fundamental role and mechanism of reduced graphene oxide in rGO/Pt-TiO_2 nanocomposite for high-performance photocatalytic water splitting.* Appl. Catal. B-Environ., 2017. **207**: p. 335-346.

50. Das, R.K., et al., *Extraordinary hydrogen evolution and oxidation reaction activity from carbon nanotubes and graphitic carbons.* Acs Nano, 2014. **8**(8): p. 8447-8456.

51. Dong, Q.C., et al., *Free-standing NiO@C nanobelt as an efficient catalyst for water splitting.* Chemcatchem, 2016. **8**(22): p. 3484-3489.

52. Hou, Y., et al., *Co_3O_4 nanoparticles embedded in nitrogen-doped porous carbon dodecahedrons with enhanced electrochemical properties for lithium storage and water splitting.* Nano Energy, 2015. **12**: p. 1-8.

53. Shi, W.N., et al., *Carbon coated Cu_2O nanowires for photo-electrochemical water splitting with enhanced activity.* Appl. Surf. Sci., 2015. **358**: p. 404-411.

54. Wu, X.Q., et al., *Control strategy on two-/four-electron pathway of water splitting by multidoped carbon based catalysts.* Acs Catal., 2017. **7**(3): p. 1637-1645.

55. Liang, Y.Y., et al., *Strongly coupled inorganic/nanocarbon hybrid materials for advanced electrocatalysis.* J. Am. Chem. Soc., 2013. **135**(6): p. 2013-2036.

56. Wang, D.W. and D.S. Su, *Heterogeneous nanocarbon materials for oxygen reduction reaction.* Energy Environ. Sci., 2014. **7**(2): p. 576-591.

Chapter 2 Literature Review

2.1 General Challenges

Reliable and affordable energy was the essential power to satisfy the rapid energy consumption for the development of the modern society.[1,2] Tranditional fossil fuels such as coal, oil or gas was considered as the dominating energy sources for its high-effiency conversion capacity from chemical energy to electrical energy or heat.[3] In 2004, the global energy consumption was about 11.7 Gtoe, 82% of the energy supply was provided by fossil fuels accompanied with the 7Gton of carbon of CO_2 emissions, and the generated CO_2 emissions were predicted to be 14 Gton of carbon in 2050.[4,5] The increasing nettlesome global warming and environmental pollution which were caused during the consumption of exhaustible fossil fuels, have drawn the scientists' attention to seek for the clean and sustainable new energy sources.[6,7] Currently, clean energy could be divided into various categories of sources including hydrogen, hydraulic, wind, geothermal, tide, solar or biomass.[8] As shown in **Figure 2.1**, among them, hydrogen energy has been considered as one of the highest potential clean energy sources since 1970s,[9] which could be applied in diverse areas such as ammonia production,[10] refining[11], chemical synthesis[12] or other fields.[4,13] To meet the requirement of massive hydrogen energy, various hydrogen generation technologies were explored. Among them, the four main industrial synthetic routes which were utilized to produce large-scale hydrogen energy were: 1. Electrolytic saturated salt solution ($2NaCl + 2H_2O \rightarrow 2NaOH + Cl_2 + H_2$). During the reaction, the produced hydrogen was usually accompanied with the chlorine generation. 2. Brewing industrial byproducts, low efficieny is its fatal flaw. 3. Fossil fuels producing hydrogen which also includes the steam methane reforming[14,15] or coal gasification ($C + H_2O \rightarrow CO +$

H_2)[16,17]. This method was the most common approach to produce hydrogen, however, the usage of the fossil fuels was still unavoidable. 4. Water electrolysis ($2H_2O \rightarrow O_2 + H_2$). [18-20] The water electrolysis was regarded as the most promising, simplest and cleanest manner to generate hydrogen energy because it only depends on the water consumables. However, the existence of several predicaments limits the wholescale application of the water electrolysis. For example, the high cost, poor efficiency or the current small-scale hydrogen production were challenging to solve. These concerns also provide the main research priorities to proceed the water electrolysis system.

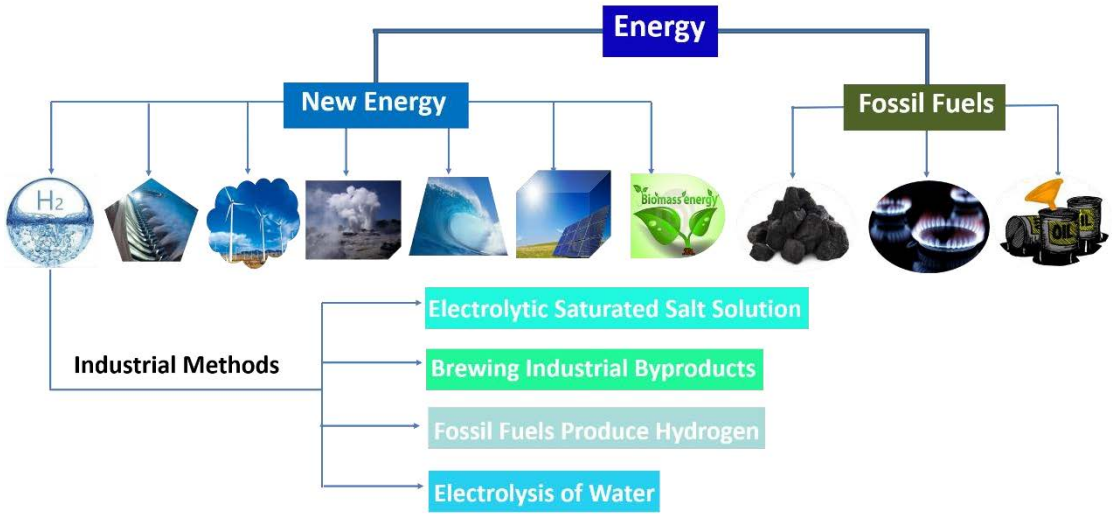

Figure 2.1 The current energy system and the main industrial methods to produce clean hydrogen energy.

2.2 Scope of The Literature Review

The scope of this review mainly focuses on how to realize the large-scale hydrogen generation during the water electrolysis system. First, we provide a brief summary of the current research advance of the water electrolysis system including the reaction devices or electrolysis progress. Then, we mainly emphasize the electrode design which was essential

and vital during the water electrolysis system. The enhanced catalytic activities of the electrode design based on the large-scale synthesis or high-efficiency methods and the various electrodes were brieftly discussed. At the last, the conlusion and outlook on the design of electrodes which could be still active at the large current densities, the exploration of the new high-active catalyst preparation and the standardized large-current-density activity parameters were also provided with the prediction of the further design thought directions.

2.3 Water Electrolysis

In the electrolyser device, the water molecules was splitted into hydrogen and oxygen with the usage of electricity, the process was called water electrolysis. The water electrolysis was firstly observed by van Troostwijk and Deinman in 1789, in 1800 Alessandro Volta invented the pile which was then being used during electrolytic splitting of water process by William Nicholson and Anthony Carlisle.[21,22] With the development of electrochemistry, in 1833, Faraday's law was defined to describe the proportional relationship between the generated gas amount and the electrical energy comsumption, thus resulting in the scientifical concept definition of water electrolysis.[21] Then, more than 400 insustrial water electrolyzers were already put into service until 1902 which were based on the Gramme machine invention by Zénobe Gramme in 1869 and the the developed industrial synthesis technique by Dmitry Lachinov in 1888.[21,23] The early water electrolysis plants were shown in **Figure 2.2**. From 1920s to 1970s, the water electrolysis technique was in its explosive development period.[21,24] For example, the water electrolysis plant was developed into a large capacity of 10,000 N m^3 H_2 h^{-1} in 1939 and the pressurized industrial electrolyzer in 1948.[23] Besides, the commercial asbestos membrane was also gradually repaced with the

usage of more healthy and chemically stable perfluorosulfonic acid or other material polymers.[21,25,26] With the more than two hundreds' development, the exploration of low-cost and high efficiency water electrolysis technologies becomes the current new challenge.

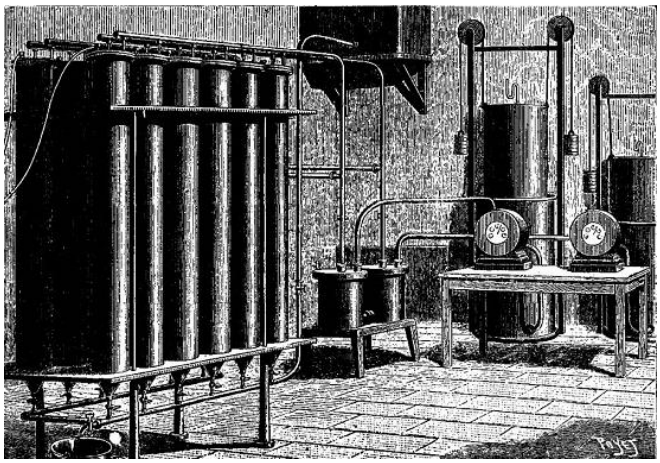

Figure 2.2 The early plants for industrial water electrolysis.[21]

2.4 Water Splitting Mechanisms

The water electrolysis device consists of two electrodes -- the anode and cathode which were both immersed into the conductive electrolyte. When the electricity is applied, the hydrogen gas was formed on the cathode and oxygen was generated on the anode. Electrolytic water electrolysis can be divided into two-half reactions: oxygen evolution reaction (OER) and hydrogen evolution reaction (HER). To improve the conductivity of the electrolytes, various high-monility ions would be added into the aqueous electrolytes.[27] According to the different electrolytes, the mechanisms of water splitting were in different models. In the acidic or neutral aqueous solution, the reaction formula on the anode and cathode were as follows:[28,29]

$$\text{OER: } 2\ H_2O \rightarrow O_2 + 4\ H^+ + 4\ e^-$$

$$E_{anodic} = 1.23\ V - 0.059 \cdot pH\ V \text{ vs. NHE} \quad (1)$$

$$HER: 4\ H^+ \rightarrow 4\ e^- + 2\ H_2$$

$$E_{cathodic} = 0\ V - 0.059 \cdot pH\ V \text{ vs. NHE} \quad (2)$$

Where the NHE is the normal hydrogen electrode.

The overall water splitting equation could be resulted from the sum of the above two formula, as shown in the following:

$$\text{Overall water splitting}: 2\ H_2O \rightarrow 2\ H_2 + O_2 \quad E_{rxn} = -1.23\ V \quad (3)$$

When the conductive electrolyte is the alkaline aqueous solution, potassium hydroxide was usually chosen to provide the hydroxyl ion due to its preferable conductivity of the formed electrolyte.[30] In the alkaline aqueous solution, the electrolytic water splitting reactions were as the following:[31]

$$OER: 4OH^- \rightarrow O_2 + 2H_2O + 4e^-$$

$$E_{anodic} = 1.23\ V - 0.059 \cdot pH\ V \text{ vs. NHE} \quad (4)$$

$$HER: 2\ H_2O + 2\ e^- \rightarrow H_2 + 2OH^-$$

$$E_{cathodic} = 0\ V - 0.059 \cdot pH\ V \text{ vs. NHE} \quad (5)$$

The sum of the above two formula demonstrates the equation during the overall water splitting equation as the following:

$$\text{Overall water splitting}: 2\ H_2O \rightarrow 2\ H_2 + O_2 \quad E_{rxn} = -1.23\ V \quad (6)$$

The constant value of -1.23 V is the required theoretical cell votage to proceed the overall water splitting system. Alkaline electrolytes for the water splitting systems were preferable

due to the corrosion problems caused by the acidic solution or low-efficiency troubles arised by the usage of neutral solution.[32] The schematic diagram for the alkaline overall water splitting device was shown in **Figure 2.3**.

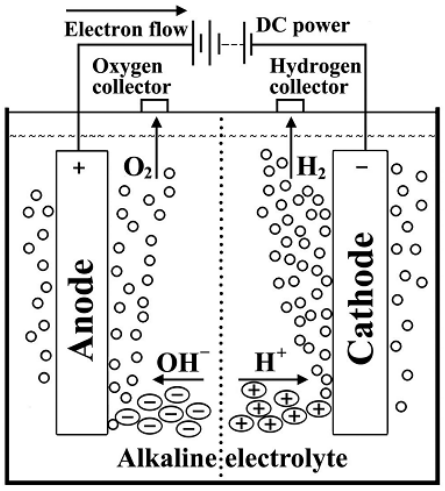

Figure 2.3 The schematic diagram for water electrolysis system under the alkaline electrolyte.[21]

2.5 Water Splitting Devices

Water electrolysis was one of the most promising routes to produce clean hydrogen energy. The suitable and advanced water splitting devices were crucial to accelerate the current water splitting systems. The current used water electrolysis devices to generate hydrogen were the two main device types of alkaline electrolyzer (AEL) and proton exchange membrane electrolyzer (PEMEL).[33-37] Besides, the hydroxide exchange membrane electrolyzer (HEMEL) was also gradually developed. Among them, AEL were in the mature technique and applied in various fields with the large-scale hydrogen production. The technology of the PEMEL was in its speedy development period with the current small-scale hydrogen generation applications. The HEMEL was designed to combine the advantages of bothe AEL and PEMEL devices and was considered as one of the promising

alternatives. The development of the water splitting devices was shown in the **Figure 2.4**.[38] The three different devices would be discussed in following separate sections.

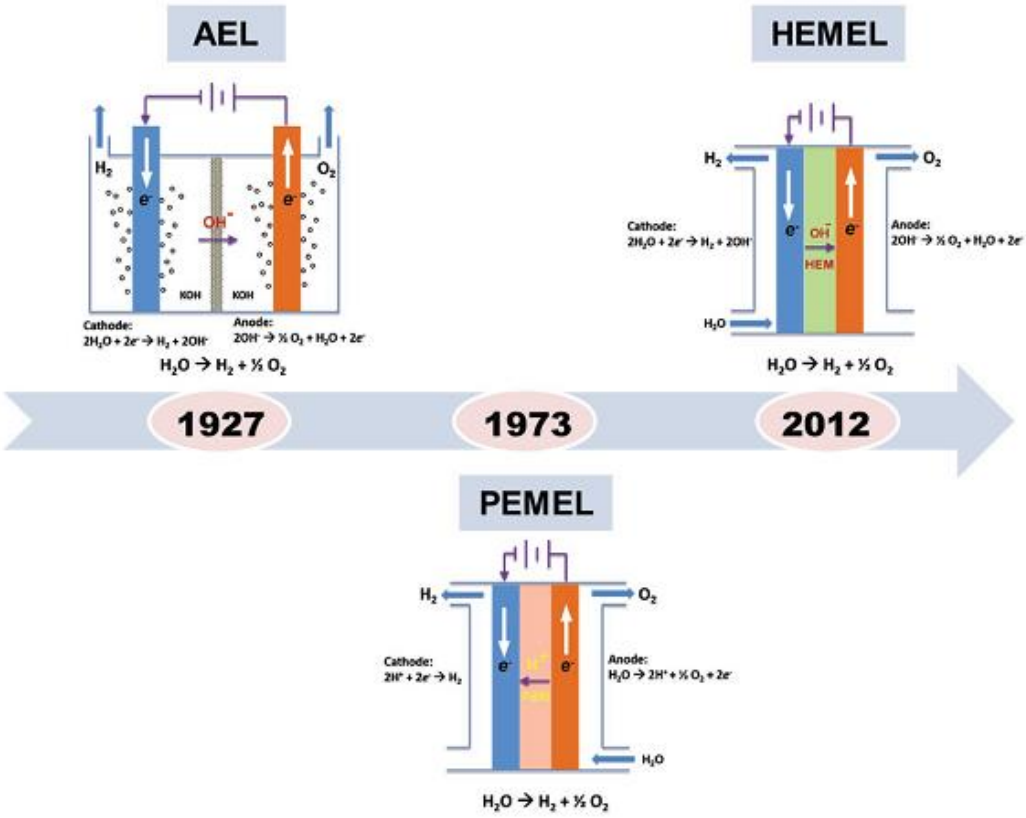

Figure 2.4 The development of low-temperature electrolysis technology devices.[38] AEL: alkaline electrolyzer. PEMEL: proton exchange membrane electrolyzer. HEMEL: hydroxide exchange membrane electrolyzer.

2.5.1 Alkaline Electrolyzer

AEL was the existing mature and advanced industrial techonology with a long development histrory since its establishment in 1927 by NEL Hydrogen.[32,39] The liquid electrolytes of the AEL was used with the alkaline electrolytes - the high concentrated patassium hydroxide aqueous solution (25%-40%).[40] The electrodes were made of the low-cost and earth-abundant nickel-based materials.[41] And the used membranes were dependent on the

chemically and thermally stable Ryton or Zirfon.[42] The current AEL devices were widely applied in numerous areas and occupied the main market share during the global water electrolysis systems with the annual hydrogen production amount of ~ 2 million tons.[43] Although the current AEL technology was in the widespread applications due to the mature technique, the usage low-cost noble-metal free electrodes, long lifetime system of 30-40 years or the large capacities, several existing negative disadvantages were still difficult to solve. For example, the limited efficiency and the reduced electrolytic performance of the AEL device system when the current densities were too high, causing by the sluggish release of formed gas bubbles or the usage of thick diaphragms.[39,44] The modified reaction models or the design of unique electrode surface to fleetly release the numerous produced gas bubbles should be paid attentions.

2.5.2 Proton Exchange Membrane Electrolyzer

To advoid the disadvantages during the AEL technique, the concept for proton exchange membrane electrolyzer (PEMEL) was built by Russell et al. in 1973 with the usage of the special material membrane – solid perfluorinated sulfonic acid membrane.[45-47] The PEMEL technique has the obvious modified advantages including the lower thickness compared with the AEL device and the high proton conductivity. Besides, the high current densities also could be operated and the higher efficiency were achieved in the PEMEL device system due to the faster dynamic response, which could be attributed to that the liquid alkaline electrolyzer used in AEL system has been replaced by the solid PEM polymer.[33] However, the harsh corrosive acidic environment causing by the usage of PEM leads to the rigorous and limited material requirement of the electrode catalysts.[46] The current electrocatalysts which were used in the PEMEL technology mainly consist of the noble

electrocatalysts such as iridium based materials as the anode and the platium based materials as the cathode. Besides, All the drawbacks including the short system lifetime of 5-20 years, high-cost membranes, costly noble metal based electrodes or the expensive stack components hinder the large-scale commercial applications for the PEMEL systems.[33,48] To address these problems, various strategies have been developed such as the connection of noble metal based electrocatalysts onto an anticorrosive substrate or the low-price advanced materials used as the membranes and other components. Until now, 60% of the cost during the PEMEL technology has been reduced which opens an accessible promising path to proceed an more advanced PEMEL system.[36]

2.5.3 Hydroxide Exchange Membrane Electrolyzer

To collect the advantages of both the AEL and PEMEL device techniques, the hydroxide exchange membrane (HEM) was applied into the electrolyzer devices to provide an alkaline condition. This advancing technique was called the hydroxide exchange membrane electrolyzer (HEMEL) which was put forward in 2012.[49,50] The HEMEL technology was in the primary development stage due to its short development history. Therefore, a huge array of problems exists during the developing HEMEL system including the high-cost setup, the complexity, electrocatalyst choices or HEM degradation. Besides the above challenging issues, the reaction technologies and mechanisms were still unclear. Based on the above current problems and the desired technique targets, massive research efforts should be invested to realize an advanced HEMEL technology system for the large-scale hydrogen commercialization.

2.6 Electrode Design

During the water splitting system, an efficient electrocatalyst was required to reduce the overpotential and enhance the reaction kinetics, thus promoting the two half-reactions including both the OER and HER. The current active electrocatalyst systems were mainly dependent on the usage of noble-metal-based materials. For example, the ruthenium-based or iridium-based materials were operated during the catalytic water oxidation reaction[51] and platinum-based materials work for the water reduction reaction.[52-55] The high cost of the noble metal materials causing by the limited scarity of their sources seriously hamper the widespread applications. Low-cost and earth-abundant material catalysts have drawn the research's attention. Inspired by the finding of water splitting sites which were made of Mn_4CaO_4 during the natural photosystem II,[56] as illustrated in **Figure 2.5a**, the transition metal based materials have been rapidly explored to simulate this reaction process. For example, various maganese oxide materials[62] have been studied for the electrocatalytic water splitting system. Besides the other transition metal based materials including the nickel based materials,[57,58] cobalt based materials,[59,60] or iron based materials[61] all have entered their rapid development stages, as shown in **Figure 2.5b-d**. However, these low-cost and earth-abundant transition metal based materials were suffering from their low active catalytic properties during water splitting systems. To enhance their catalytic activities, various strategies have been explored and applied. Herein, we give a brief disscussion with the usual used methods such as morphology design, composition control, three-dimensional electrode design or the potential usage of "superaerophobic" surface, these sections are decribed as the followings.

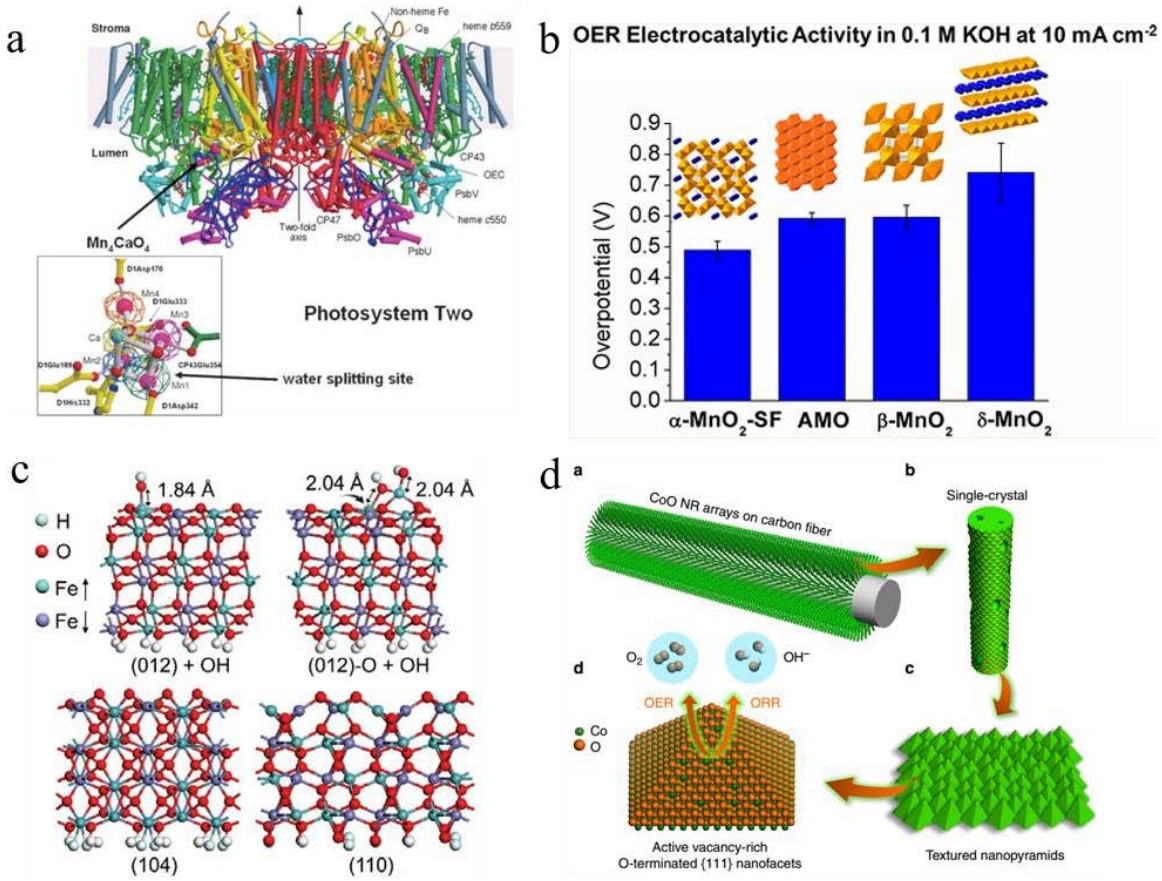

Figure 2.5 (a) Side view of Photosystem II structure.[56] (b) Manganese oxides in various structures including α-, β-, δ-MnO_2 and amorphous form were explored during OER.[62] (c) Optimized atomic structures for OH binding on different facets of hematite nanocrystals.[61] (d) The schematic illustration of engineering the surface of single-crystal CoO nanorods for OER and oxygen reduction reaction (ORR).[59]

2.6.1 Morphology Design

Efficient electrocatalysts including the HER and OER catalysts were essential to construct the water splitting devices. To boost the performance of water electrolysis system, various methods have been designed. Among them, the morphology design is the available controlled synthesis method, which plays a vital role to adjust the catalytic efficacy of the electrocatalysts. The bulk materials usually exhibit low-efficiency catalytic property due to

the limited exposed active sites or blocked transfer capacity. Thus, to relax its intrinsic catalytic property, the structure size should be reduced. Furthermore, to enhance the property performance of the promising low-cost and earth-abundant electrocatalysts, nanostructure could be operated into the applications. Common morphology structure for the nanomaterials was including the nanoparticles, nanosheets, nanowires, nanobelts or other material morphologies. Accompanied with the tailored morphology structure of the electrocatalysts, the roughness, surface areas, the accessible exposed catalytic sites or other catalytic properties also have been altered. The design of three different morphology

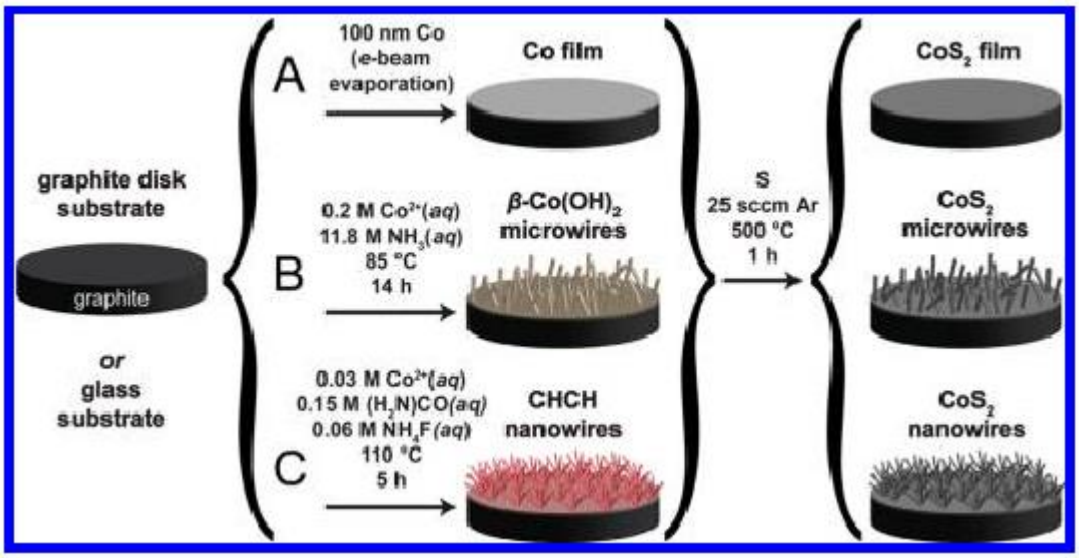

Figure 2.6 Schematic depictions of the different morphology preparation of the cobalt pyrite (CoS_2). (A) Film, (B) microwire (MW) array, and (C) nanowire (NW) array which was on a graphite disk or glass substrate.[63]

structures for the cobalt pyrite (CoS_2) catalysts was chosen to be investigated, as shown in **Figure 2.6**.[63] During the reported research of Jin's group, the modified microwire or nanowire morphologies of CoS_2 show the enhanced catalytic activities and improved stability due to the facilitated charge transfer and superior electrode contact surface. This morphology design method provides an available route to improve the catalytic property of

the low-cost and earth-abundant electrocatalyst, thus making them the alternatives to the noble metal catalysts.

2.6.2 Composition Control

The exploration of low-cost and high-efficiency material catalysts occupies an important place for electrocatalytic water splitting system to produce clean hydrogen energy. The tremendous efforts have been devoted into the development of the transition metal-based materials, as the alternatives to high-cost noble metal catalysts. Besides the development of the potential transition metal oxide/hydroxides,[64-68] or other transition metal compounds including transition chalcogenides,[69-71] transition metal phosphides,[72-74] transition metal nitrides[75-77] or transition borides[78-80] were also explored. To enhance their catalytic performances, the formation of the preferable electronic state, more defects or the enhanced exposed active sites was required.[81] The composition control strategy such as cation or anion incorporation was the promising approach for the superior catalytic activities.[82,83] With the induced suitable heterogeneous atoms, the lattices were distorted due to strain causing by the different atom radiuses or the electro-state, then leading to more defects, enhanced lattice vacancies, improved exposed active sites or superior electronic energy state, which would improve the catalytic water splitting performances. Furthermore, the combined dual or multifarious heterogeneous atoms also show the synergistic effect would demonstrate the stronger effects with a further improved catalytic performance. For example, As shown in **Figure 2.7**, the dual-cation iron and cobalt works together to provide a more superior water splitting system.[84] The composition control strategy was always one of the most promising routes for the material design due to its excellent effect and flexibility.

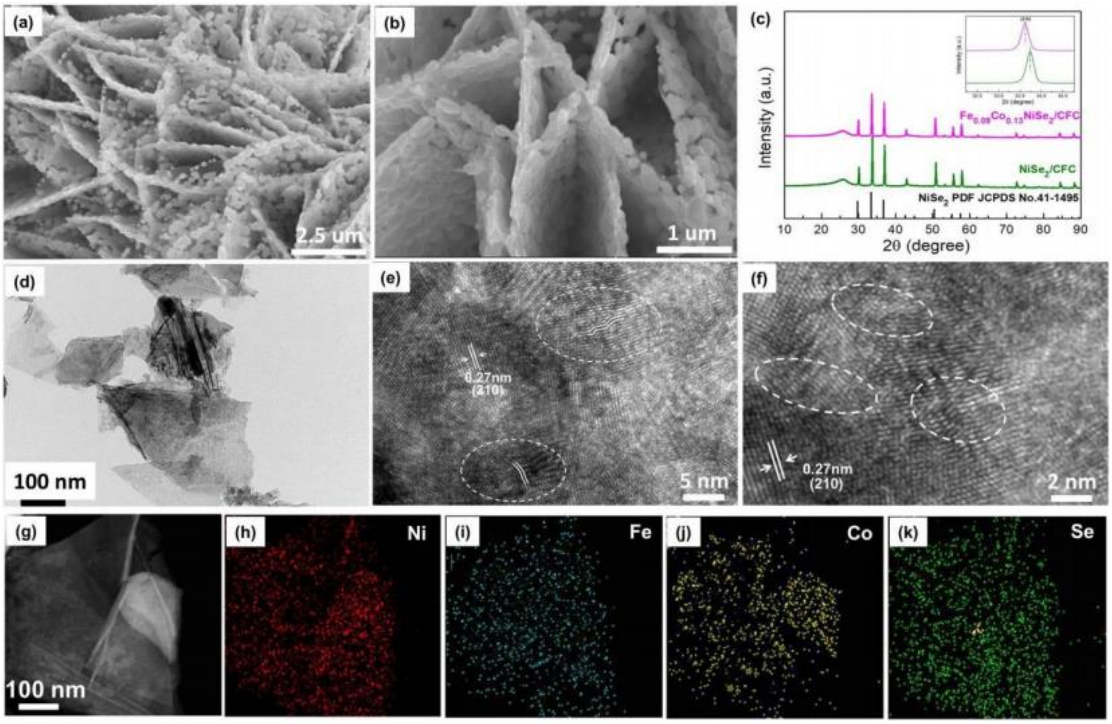

Figure 2.7 Characterizations of the dual cation doped $NiSe_2$ nanosheets. (a-b) SEM images, (c) XRD patterns, (d-k) TEM, HRTEM and STEM-EDX elemental mapping images for the dual cation doped $NiSe_2$ nanosheets.[84]

2.6.3 Three-Dimensional Electrode

The development of economical water splitting system was necessarily dependent on the accelerated two-half reactions' kinetics. To pursue this aim, a series of strategies were adopted to develop the two main technique systems made of the powder electrocatalysts and three-dimensional electrodes, respectively. The application of powder electrocatalysts always result in the decreased catalytic activities or poor stability at high current densities due to the usage of polymer binder which was essential to connect the powder electrocatalyst and the conductive substrate.[85,86] Therefore, the catalyst materials which were directly grown on the conductive substrates become the potential alternative to improve the catalytic properties. The current conductive substrates are mainly including

carbon paper,[87] carbon cloth,[88] copper foil,[89,90] FTO[91] and nickel foam,[92-94] etc. Among them, nickel foam substrate was optimal due to its low cost, porous three-dimensional network, large surface area and high conductivity.[92] The three-dimensional electrodes consisting of the nickel foam and the catalysts grown on the nickel foam substrates

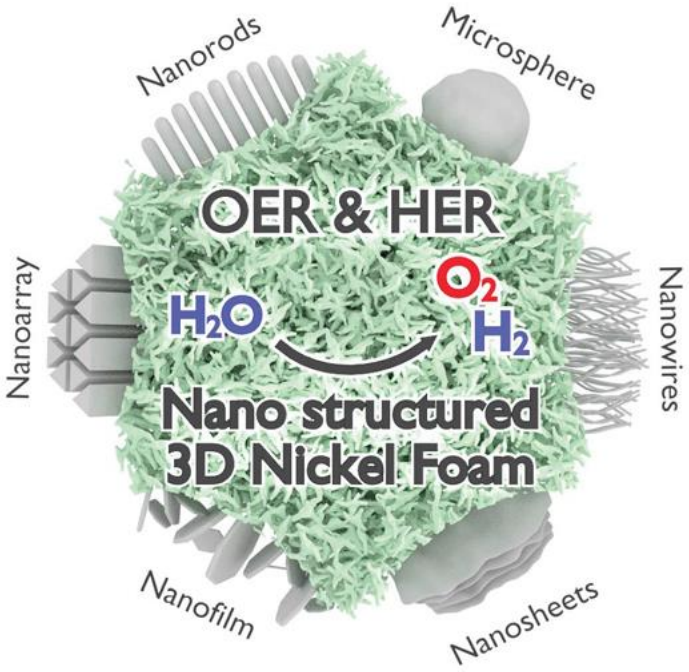

Figure 2.8 Overview of three-dimensional electrocatalysts grown on the nickel foam substrate for OER and HER.[95]

demonstrate the great potential to advance water electrolysis due to their direct catalyst-substrate contact and binder-free property.[95] The highly active catalytic activities of the three-dimensional electrodes could be attributed to their high conductivity, superior mass and charge transfer, and large surface area. Furthermore, the nanostructure materials grown on the nickel foam substrate would also exhibit an excellent stability during water splitting due to their solid connection and efficient intrinsic property.[96] As shown in **Figure 2.8**, various nanostructured catalysts could grow on the nickel foam substrates,[95] the constructed three-dimensional electrode would accelerate the electrochemical energy technologies.

2.6.4 "Superaerophobic" Surface

To produce large-scale hydrogen energy, water electrolysis techniques should be operated at high current densities. To efficiently catalyze water splitting at high current densities, the rapid mass and charge transfer would be required, thus, three-dimensional electrocatalysts was the potential alternatives.[97] However, the most challenging technique for the electrocatalysts was how to keep the active catalytic property at high current densities. The large amount of the produced hydrogen bubbles was formed and aggregated onto the used electrode when the water splitting system was operated at high current densities, leading to the rapidly reduced contact surface between the electrolyte and electrode. The limited contact surface interface would result in the inferior electrocatalytic properties, high resistance and poor stability. To realize the large-scale hydrogen generations, several catalyst systems for high-current operations have been explored, such as the hybrid bimetallic phosphides (FeP/Ni_2P) system for OER and HER,[98] $Fe(PO_3)_2$ on Ni_2P/NF and Ni-Fe-OH@Ni_3S_2/NF for OER.[99,100] All the above systems were used with the three-dimensional electrodes, and the unique surface structure was formed on the obtained three-dimensional electrocatalysts. The unique surface structure was confirmed by the reported research of Jin's[63] and Sun's[101] groups to be the "superaerophobic" surface, as shown in **Figure 2.9**. The "superaerophobic" surface structure was formed with the assemble of array architecture,[102] which could be utilized to quickly release the tremendous quantities of generated gas bubbles. Consequently, the active catalytic property of the electrocatalysts can retain when the water splitting system was run at the high current densities. Thus, the constructed array architectures for three-dimensional electrodes was necessary during large-scale hydrogen production systems.

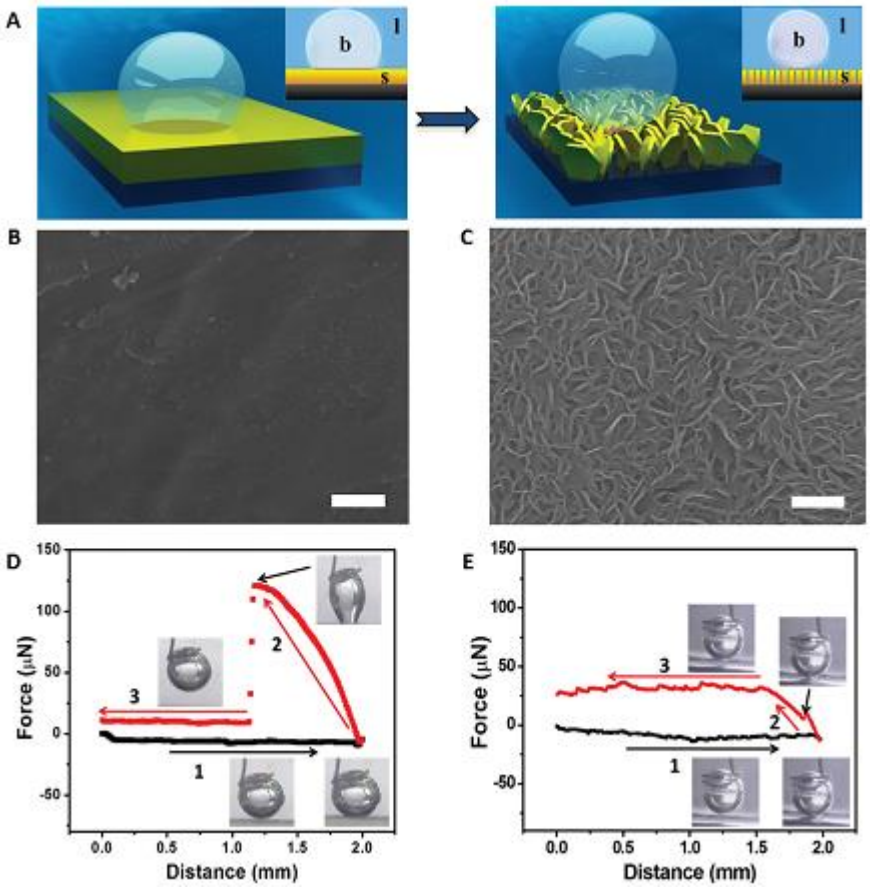

Figure 2.9 The Schematic illustration, top-view SEM images and adhesive forces measurements of gas bubbles on the flat film (left) (A, B, D) and the nanostructured film (right) (A, C, E), respectively.[101]

2.7 Summary

During this chapter, the development history of the water electrolysis was briefly introduced. The evolution process of the electrolytic water splitting technology devices was also discussed, the merits and demerits of the different water electrolysis devices were presented. The choice development of electrode electrocatalysts from noble metal materials to non-noble metal catalysts was further described in the brief analysis. And the materials design to enhance the electrocatalytic activities of the non-noble metal catalysts was explored. To meet the requirement of the large-scale hydrogen productions which were in

sore need in various new energy fields, the challenges of the electrocatalysts is how to survive and maintain the highly active catalytic property at the high current densities. Thus, the important factors which could be used to define the catalytic activities operated at high current densities needs to be on the agenda. Herein, during this literature review, we provide several assumptions about the standardization of the parameters for the electrocatalysts which could be used at high current densities. Such as the required overpotential at 1000 mA cm^{-2}, the "Tafel slope" calculated according to relationship between the large current densities and the applied potentials or other important parameters which could be used to express the catalytic property of the electrodes when the current density was very large. Besides, the progress of the membranes or the electrolytes also needs to be noticed and further explored. The development of the current water electrolysis is still the hopeful route to generate hydrogen to satisfy the industrial large-scale productions.

2.8 References

1. Chu, S. and A. Majumdar, *Opportunities and challenges for a sustainable energy future.* Nature, 2012. **488**(7411): p. 294-303.

2. Debe, M.K., *Electrocatalyst approaches and challenges for automotive fuel cells.* Nature, 2012. **486**(7401): p. 43-51.

3. Li, H.H. and S.H. Yu, *Recent advances on controlled synthesis and engineering of hollow alloyed nanotubes for electrocatalysis.* Adv. Mater., 2019. **31**(38): p. 1803503.

4. Marbán, G. and T. Valdés-Solís, *Towards the hydrogen economy?* Int. J. Hydrog. Energy, 2007. **32**(12): p. 1625-1637.

5. Pacala, S. and R. Socolow, *Stabilization wedges: solving the climate problem for the next 50 years with current technologies.* Science, 2004. **305**(5686): p. 968-972.

6. Balat, M. and M. Balat, *Political, economic and environmental impacts of biomass-based hydrogen.* Int. J. Hydrog. Energy 2009. **34**(9): p. 3589-3603.

7. Muradov, N.Z. and T.N. Veziroğlu, *"Green" path from fossil-based to hydrogen economy: an overview of carbon-neutral technologies.* Int. J. Hydrog. Energy 2008. **33**(23): p. 6804-6839.

8. Sharma, S. and S.K. Ghoshal, *Hydrogen the future transportation fuel: From production to applications.* Renew. Sust. Energ. Rev., 2015. **43**: p. 1151-1158.

9. JO'M, B., *The origin of ideas on a hydrogen economy and its solution to the decay of the environment.* Int. J. Hydrog. Energy, 2002. **27**(7-8): p. 731-740.

10. Mueller-Langer, F., et al., *Techno-economic assessment of hydrogen production processes for the hydrogen economy for the short and medium term.* Int. J. Hydrog. Energy, 2007. **32**(16): p. 3797-3810.

11. Ramachandran, R. and R.K. Menon, *An overview of industrial uses of hydrogen.* Int. J. Hydrog. Energy, 1998. **23**(7): p. 593-598.

12. Eliaz, N., D. Eliezer, and D. Olson, *Hydrogen-assisted processing of materials.* Mater. Sci. Eng. A, 2000. **289**(1-2): p. 41-53.

13. Barreto, L., A. Makihira, and K. Riahi, *The hydrogen economy in the 21st century: a sustainable development scenario.* Int. J. Hydrog. Energy, 2003. **28**(3): p. 267-284.

14. Council, N.R., *The hydrogen economy: opportunities, costs, barriers, and R&D needs*. 2004: National Academies Press.

15. Turner, J.A., *Sustainable hydrogen production.* Science, 2004. **305**(5686): p. 972-974.

16. Rosen, M. and D. Scott, *Comparative efficiency assessments for a range of hydrogen production processes.* Int. J. Hydrog. Energy 1998. **23**(8): p. 653-659.

17. Trommer, D., et al., *Hydrogen production by steam-gasification of petroleum coke using concentrated solar power—I. Thermodynamic and kinetic analyses.* Int. J. Hydrog. Energy 2005. **30**(6): p. 605-618.

18. Holladay, J.D., et al., *An overview of hydrogen production technologies.* Catal. Today, 2009. **139**(4): p. 244-260.

19. Zou, X. and Y. Zhang, *Noble metal-free hydrogen evolution catalysts for water splitting.* Chem. Soc. Rev., 2015. **44**: p. 5148-5180.

20. Stojić, D.L., et al., *Hydrogen generation from water electrolysis—possibilities of energy saving.* J. Power Sources, 2003. **118**(1-2): p. 315-319.

21. Santos, D.M., C.A. Sequeira, and J.L. Figueiredo, *Hydrogen production by alkaline water electrolysis.* Quim. Nova, 2013. **36**(8): p. 1176-1193.

22. Trasatti, S., *Water electrolysis: who first?* J. Electroanal. Chem., 1999. **476**(1): p. 90-91.

23. Kreuter, W. and H. Hofmann, *Electrolysis: the important energy transformer in a world of sustainable energy.* Int. J. Hydrog. Energy 1998. **23**(8): p. 661-666.

24. Zeng, K. and D. Zhang, *Recent progress in alkaline water electrolysis for hydrogen production and applications.* Prog. Energy Combust. Sci., 2010. **36**(3): p. 307-326.

25. Hickner, M.A., et al., *Alternative polymer systems for proton exchange membranes (PEMs).* Chem. Rev., 2004. **104**(10): p. 4587-4612.

26. Rosa, V., M. Santos, and E. Da Silva, *New materials for water electrolysis diaphragms.* Int. J. Hydrog. Energy 1995. **20**(9): p. 697-700.

27. Oldham, K. and J. Myland, *Fundamentals of electrochemical science*. 2012: Elsevier.

28. Kanan, M.W. and D.G. Nocera, *In situ formation of an oxygen-evolving catalyst in neutral water containing phosphate and Co^{2+}.* Science, 2008. **321**(5892): p. 1072-1075.

29. Li, F., et al., *Macroporous Inverse opal-like Mo_xC with incorporated Mo vacancies for significantly enhanced hydrogen evolution.* Acs Nano, 2017. **11**(7): p. 7527-7533.

30. Chadwick, S.S., *Ullmann's encyclopedia of industrial chemistry.* Ref. Serv. Rev., 1988.

31. Suen, N.-T., et al., *Electrocatalysis for the oxygen evolution reaction: recent development and future perspectives.* Chem. Soc. Rev., 2017. **46**(2): p. 337-365.

32. LeRoy, R., *Industrial water electrolysis: present and future.* Int. J. Hydrog. Energy 1983. **8**(6): p. 401-417.

33. Ayers, K.E., et al., *Research advances towards low cost, high efficiency PEM electrolysis.* ECS Trans., 2010. **33**(1): p. 3.

34. Ayers, K.E., C. Capuano, and E.B. Anderson, *Recent advances in cell cost and efficiency for PEM-based water electrolysis.* Ecs Trans., 2012. **41**(10): p. 15-22.

35. Council, H., *Hydrogen scaling up, A sustainable pathway for the global energy transition.* Hydrogen Roadmap Europe, 2017.

36. Pivovar, B., N. Rustagi, and S. Satyapal, *Hydrogen at scale (H_2@ scale): key to a clean, economic, and sustainable energy system.* Electrochem. Soc. Interface, 2018. **27**(1): p. 47-52.

37. Xu, D., et al., *Earth-abundant oxygen electrocatalysts for alkaline anion-exchange-membrane water electrolysis: Effects of catalyst conductivity and comparison with performance in three-electrode cells.* ACS Catal., 2018. **9**(1): p. 7-15.

38. Abbasi, R., et al., *A roadmap to low-cost hydrogen with hydroxide exchange membrane electrolyzers.* Adv. Mater., 2019. **31**(31): p. 1805876.

39. Felgenhauer, M. and T. Hamacher, *State-of-the-art of commercial electrolyzers and on-site hydrogen generation for logistic vehicles in South Carolina.* Int. J. Hydrog. Energy, 2015. **40**(5): p. 2084-2090.

40. Godula-Jopek, A., *Hydrogen production: by electrolysis*. 2015: John Wiley & Sons.

41. Mahmood, N., et al., *Electrocatalysts for hydrogen evolution in alkaline electrolytes: mechanisms, challenges, and prospective solutions.* Adv. Sci., 2018. **5**(2): p. 1700464.

42. Vermeiren, P., et al., *Evaluation of the Zirfon® separator for use in alkaline water electrolysis and Ni-H_2 batteries.* Int. J. Hydrog. Energy, 1998. **23**(5): p. 321-324.

43. LeRoy, R., *Industrial water electrolysis: present and future.* Int. J. Hydrog. Energy, 1983. **8**(6): p. 401-417.

44. Bodner, M., A. Hofer, and V. Hacker, *Wiley Interdiscip. Rev.* Energy Environ., 2014. **4**: p. 365-381.

45. Russell, J., L. Nuttall, and A. Fickett, *Hydrogen generation by solid polymer electrolyte water electrolysis.* Am. Chem. Soc. Div. Fuel Chem. Prepr, 1973. **18**: p. 24-40.

46. Carmo, M., et al., *A comprehensive review on PEM water electrolysis.* Inter. J. Hydrog. Energy, 2013. **38**(12): p. 4901-4934.

47. Siracusano, S., et al., *An electrochemical study of a PEM stack for water electrolysis.* Inter. J. Hydrog. Energy, 2012. **37**(2): p. 1939-1946.

48. Götz, M., et al., *Renewable power-to-gas: A technological and economic review.* Renewable Energy, 2016. **85**: p. 1371-1390.

49. Lim, A., et al., *A review of industrially developed components and operation conditions for anion exchange membrane water electrolysis.* J. Electrochem. Sci. Technol., 2017. **8**: p. 265.

50. Xiao, L., et al., *First implementation of alkaline polymer electrolyte water electrolysis working only with pure water.* Energy Environ. Sci., 2012. **5**(7): p. 7869-7871.

51. Spoeri, C., et al., *The stability challenges of oxygen evolving electrocatalysts: Towards a common fundamental understanding and mitigation of catalyst degradation.* Angew. Chem. Int. Ed., 2017. **56**: p. 5994-6021.

52. Greeley, J., et al., *Alloys of platinum and early transition metals as oxygen reduction electrocatalysts.* Nat. Chem., 2009. **1**(7): p. 552-556.

53. Li, M., et al., *Ultrafine jagged platinum nanowires enable ultrahigh mass activity for the oxygen reduction reaction.* Science, 2016. **354**(6318): p. 1414-1419.

54. Lim, B., et al., *Pd-Pt bimetallic nanodendrites with high activity for oxygen reduction.* Science, 2009. **324**(5932): p. 1302-1305.

55. Yin, H., et al., *Ultrathin platinum nanowires grown on single-layered nickel hydroxide with high hydrogen evolution activity.* Nat. Commun., 2015. **6**(1): p. 1-8.

56. Barber, J., *Photosynthetic energy conversion: natural and artificial.* Chem. Soc. Rev., 2009. **38**(1): p. 185-196.

57. Foerster, F. and A. Piguet, *On the understanding of anodic formation of oxygen.* Z. Angew. Phys. Chem, 1904. **10**: p. 714-721.

58. Gong, M. and H. Dai, *A mini review of NiFe-based materials as highly active oxygen evolution reaction electrocatalysts.* Nano Res., 2014. **8**(1): p. 23-39.

59. Ling, T., et al., *Engineering surface atomic structure of single-crystal cobalt (II) oxide nanorods for superior electrocatalysis.* Nat. Commun., 2016. **7**: p. 12876.

60. Xu, L., et al., *Plasma-engraved Co_3O_4 nanosheets with oxygen vacancies and high surface area for the oxygen evolution reaction.* Angew. Chem. Int. Ed., 2016. **55**(17): p. 5277-5281.

61. Wu, H., et al., *Identification of facet-governing reactivity in hematite for oxygen evolution.* Adv. Mater., 2018. **30**(52): p. 1804341.

62. Meng, Y., et al., *Structure−property relationship of bifunctional MnO_2 nanostructures: Highly efficient, ultra-stable electrochemical water oxidation and oxygen reduction reaction catalysts identified in alkaline media.* J. Am. Chem. Soc., 2014. **136**: p. 11452-11464.

63. Faber, M.S., et al., *High-performance electrocatalysis using metallic cobalt pyrite (CoS_2) micro- and nanostructures.* J. Am. Chem. Soc., 2014. **136**(28): p. 10053-10061.

64. Song, F. and X. Hu, *Exfoliation of layered double hydroxides for enhanced oxygen evolution catalysis.* Nat Commun, 2014. **5**: p. 4477.

65. Bediako, D.K., et al., *Structure–activity correlations in a nickel–borate oxygen evolution catalyst.* J. Am. Chem. Soc., 2012. **134**(15): p. 6801-6809.

66. Gao, M.-R., et al., *Efficient water oxidation using nanostructured α-nickel-hydroxide as an electrocatalyst.* J. Am. Chem. Soc., 2014. **136**: p. 7077-7084.

67. Bode, H., K. Dehmelt, and J. Witte, *Zur kenntnis der nickelhydroxidelektrode—I.Über das nickel (II)-hydroxidhydrat.* Electrochim. Acta, 1966. **11**(8): p. 1079-1087.

68. Diaz-Morales, O., et al., *Guidelines for the rational design of Ni-based double hydroxide electrocatalysts for the oxygen evolution reaction.* ACS Catal., 2015. **5**(9): p. 5380-5387.

69. Liu, Y., et al., *Ultrathin Co_3S_4 nanosheets that synergistically engineer spin states and exposed polyhedra that promote water oxidation under neutral conditions.* Angew. Chem. Int. Ed., 2015. **54**(38): p. 11231-11235.

70. Zhou, W., et al., *Ni_3S_2 nanorods/Ni foam composite electrode with low overpotential for electrocatalytic oxygen evolution.* Energy Environ. Sci., 2013. **6**: p. 2921-2924

71. Lai, C.-H., M.-Y. Lu, and L.-J. Chen, *Metal sulfide nanostructures: synthesis, properties and applications in energy conversion and storage.* J. Mater. Chem., 2012. **22**(1): p. 19-30.

72. Popczun, E.J., et al., *Nanostructured nickel phosphide as an electrocatalyst for the hydrogen evolution reaction.* J. Am. Chem. Soc., 2013. **135**(25): p. 9267-9270.

73. Kupka, J. and A. Budniok, *Electrolytic oxygen evolution on Ni-Co-P alloys.* J. Appl. Electrochem., 1990. **20**(6): p. 1015-1020.

74. Stern, L.-A., et al., *Ni_2P as a Janus catalyst for water splitting: the oxygen evolution activity of Ni_2P nanoparticles.* Energy Environ. Sci., 2015. **8**: p. 2347-2351.

75. Oda, K., T. Yoshio, and K. Oda, *Preparation of Co-N films by rf-sputtering.* J. Mater. Sci., 1987. **22**(8): p. 2729-2733.

76. Chen, P., et al., *Metallic Co_4N porous nanowire arrays activated by surface oxidation as electrocatalysts for the oxygen evolution reaction.* Angew. Chem. Int. Ed., 2015. **54**: p. 14710-14714.

77. Zhang, Y., et al., *Rapid synthesis of cobalt nitride nanowires: Highly efficient and low-cost catalysts for oxygen evolution.* Angew. Chem. Int. Ed., 2016. **55**: p. 8670-8674.

78. Li, H., et al., *Mesoporous Ni–B amorphous alloy microspheres with tunable chamber structure and enhanced hydrogenation activity.* Chem. Commun., 2010. **46**(5): p. 791-793.

79. Masa, J., et al., *Ultrathin high surface area nickel boride (Ni_xB) nanosheets as highly efficient electrocatalyst for oxygen evolution.* Adv. Energy Mater., 2017. **7**(17): p. 1700381.

80. Masa, J., et al., *Amorphous cobalt boride (Co_2B) as a highly efficient nonprecious catalyst for electrochemical water splitting: oxygen and hydrogen evolution.* Adv. Energy Mater., 2016. **6**(6): p. 1502313.

81. Yan, D., et al., *Defect chemistry of nonprecious-metal electrocatalysts for oxygen reactions.* Adv. Mater., 2017. **29**(48): p. 1606459.

82. Smith, R.D.L., et al., *Photochemical route for accessing amorphous metal oxide materials for water oxidation catalysis.* Science, 2013. **340**(6128): p. 60-63.

83. McCrory, C.C.L., et al., *Benchmarking heterogeneous electrocatalysts for the oxygen evolution reaction.* J. Am. Chem. Soc., 2013. **135**: p. 16977-16987.

84. Sun, Y., et al., *Strong electronic interaction in dual-cation-incorporated $NiSe_2$ nanosheets with lattice distortion for highly efficient overall water splitting.* Adv. Mater., 2018. **30**(35): p. 1802121.

85. Xia, C., et al., *Selenide-based electrocatalysts and scaffolds for water oxidation applications.* Adv. Mater., 2016. **28**(1): p. 77-85.

86. Zhao, Z., et al., *A high-performance binary Ni–Co hydroxide-based water oxidation electrode with three-dimensional coaxial nanotube array structure.* Adv. Funct. Mater., 2014. **24**(29): p. 4698-4705.

87. Wang, X., et al., *Bifunctional nickel phosphide nanocatalysts supported on carbon fiber paper for highly efficient and stable overall water splitting.* Adv. Funct. Mater., 2016. **26**(23): p. 4067-4077.

88. Fang, W., et al., *Nickel promoted cobalt disulfide nanowire array supported on carbon cloth: an efficient and stable bifunctional electrocatalyst for full water splitting.* Electrochem. Commun., 2016. **63**: p. 60-64.

89. Jiang, N., et al., *Electrodeposited cobalt-phosphorous-derived films as competent bifunctional catalysts for overall water splitting.* Angew. Chem. Int. Ed., 2015. **54**(21): p. 6251-6254.

90. Li, P., et al., *Highly active 3D-nanoarray-supported oxygen-evolving electrode generated from cobalt-phytate nanoplates.* Chem. Mater., 2016. **28**(1): p. 153-161.

91. Jiang, N., et al., *Electrodeposited nickel-sulfide films as competent hydrogen evolution catalysts in neutral water.* J. Mater. Chem. A, 2014. **2**(45): p. 19407-19414.

92. Lu, B., et al., *Oxygen evolution reaction on Ni-substituted Co_3O_4 nanowire array electrodes.* Int. J. Hydrog. Energy, 2011. **36**(1): p. 72-78.

93. Yang, G.-W., C.-L. Xu, and H.-L. Li, *Electrodeposited nickel hydroxide on nickel foam with ultrahigh capacitance.* Chem. Commun., 2008(48): p. 6537-6539.

94. Li, Y., et al., *Electrodeposited ternary iron-cobalt-nickel catalyst on nickel foam for efficient water electrolysis at high current density.* Colloids Surf. A, 2016. **506**: p. 694-702.

95. Chaudhari, N.K., et al., *Nanostructured materials on 3D nickel foam as electrocatalysts for water splitting.* Nanoscale, 2017. **9**(34): p. 12231-12247.

96. Lu, X. and C. Zhao, *Electrodeposition of hierarchically structured three-dimensional nickel–iron electrodes for efficient oxygen evolution at high current densities.* Nat. Commun., 2015. **6**(1): p. 1-7.

97. Ahn, S.H., et al., *Effect of morphology of electrodeposited Ni catalysts on the behavior of bubbles generated during the oxygen evolution reaction in alkaline water electrolysis.* Chem. Commun., 2013. **49**(81): p. 9323-9325.

98. Yu, F., et al., *High-performance bifunctional porous non-noble metal phosphide catalyst for overall water splitting.* Nat. Commun., 2018. **9**: 2551.

99. Zhou, H.Q., et al., *Highly active catalyst derived from a 3D foam of $Fe(PO_3)_2/Ni_2P$ for extremely efficient water oxidation.* P. Natl. Acad. Sci. USA, 2017. **114**(22): p. 5607-5611.

100. Zou, X., et al., *Ultrafast formation of amorphous bimetallic hydroxide films on 3D conductive sulfide nanoarrays for large-current-density oxygen evolution electrocatalysis.* Adv. Mater., 2017. **29**(22).

101. Lu, Z.Y., et al., *Ultrahigh hydrogen evolution performance of under-water "superaerophobic" MoS_2 nanostructured electrodes.* Adv. Mater., 2014. **26**(17): p. 2683-2687.

102. Mishra, I.K., et al., *Hierarchical $CoP/Ni_5P_4/CoP$ microsheet arrays as a robust pH-universal electrocatalyst for efficient hydrogen generation.* Energy Environ. Sci., 2018. **11**(8): p. 2246-2252.

Chapter 3 Experiments and Strategies

3.1 Overview

During the research study, a variety of research characterizations and methods were utilized, the main experimental strategies and techniques used in this thesis were summarized, as shown in **Figure 3.1**. According to the different emphasis, the experimental parts could be divided into three principal sections. The first section focuses on the involved methods to prepare the designed materials, including hydrothermal strategies, phosphorization treatments, annealing reactions, or ion exchange methods. The second section is about a series of techniques used to analyze the as-prepared materials, including the morphology, physical property or chemical nature characterizations. The morphology measurement facilities: scanning electron microscopy (SEM), transmission electron microscopy (TEM) and high-resolution transmission electron microscopy (HRTEM). Physical and chemical characterizations: X-ray diffraction (XRD), X-ray photoelectron spectroscopy (XPS), Raman spectroscopy, energy dispersive X-ray (EDX), elemental mapping, selected area electron diffraction (SAED), density functional theory (DFT) calculations or contact angle test. The third section is about the electrochemical analysis using a three-electrode or two-electrode device via the Multipotentiostat setup. The important factors include polarization curves, Tafel plots, electrochemical impedance spectroscopy (EIS) Nyquist plots, double-layer capacitances (C_{dl}), cyclic voltammetry (CV) curves, long-term chronoamperometry test, multi-chronoamperometric test, multi-step chronopotentiometry test, accelerated cyclic polarization curves, long-term chronopotentiometry test. During the research study, the different experimental sections work together to present the systematic research results.

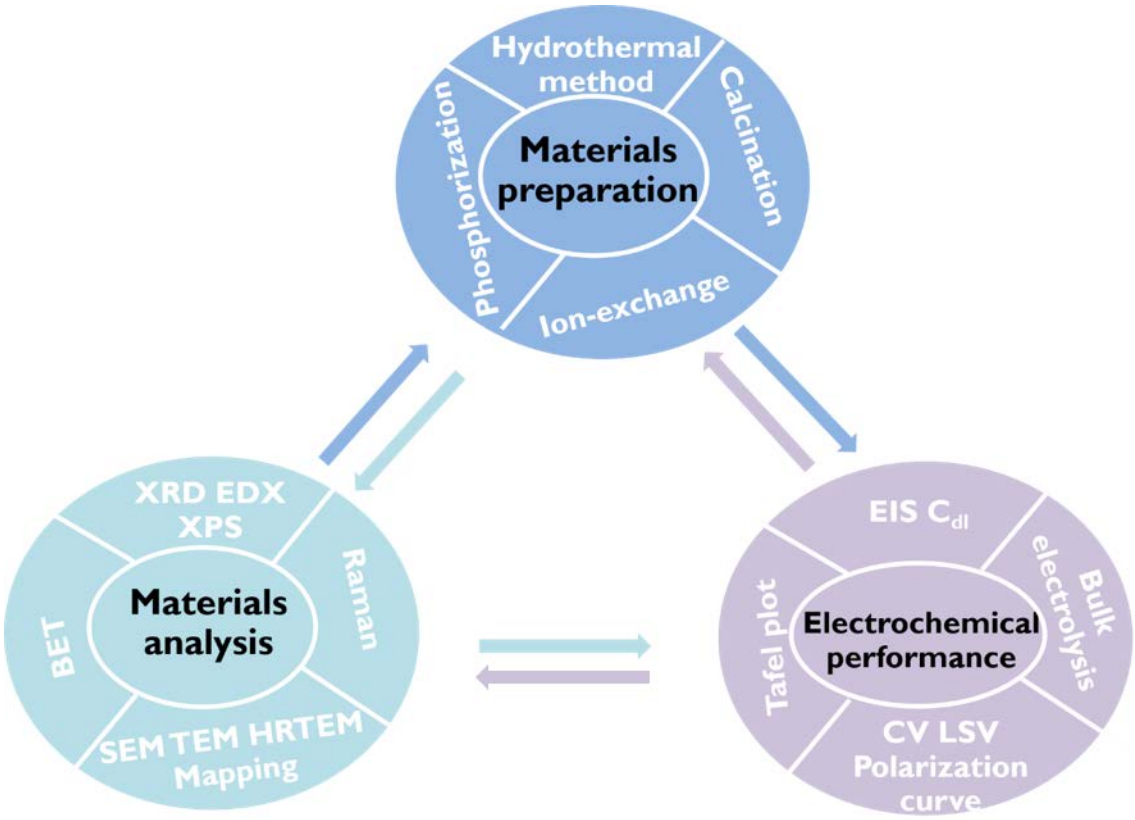

Figure 3.1 The main experimental strategies and techniques during the research work.

3.2 Chemicals

In this thesis, all the chemicals which were involved during the material preparation was listed in **Table 3.1**, including the chemical names and their formula.

Table 3.1 Chemicals Information

Chemicals	**Formula**
Hydrochloric Acid	HCl
Ethanol	CH_3CH_2OH
Diammonium hydrogen phosphate	$(NH_4)_2HPO_4$
Potassium hydroxide	KOH
Sodium hypophosphite monohydrate	$NaH_2PO_2H_{\ 2}O$

Iron nitrate nonahydrate	$Fe(NO_3)_2{\cdot}9H_2O$
Nickel nitrate hexahydrate	$Ni(NO_3)_2{\cdot}6H_2O$
copper nitrate hemi(pentahydrate)	$Cu(NO_3)_2{\cdot}21/2H_2O$
Urea	$(NH_2)_2CO$
Ammonium fluoride	NH_4F
Commercial Pt/C (20 wt%)	Pt/C
Commercial Ir/C (20 wt%)	Ir/C
Nafion (5%)	$C_9HF_{17}O_5S$
Methyl orange	$C_{14}H_{14}N_3SO_3Na$
Cobalt nitrate hexahydrate	$Co(NO_3)_2{\cdot}6H_2O$
Sodium sulfide nonahydrate	$Na_2S{\cdot}9H_2O$
Potassium phosphate monobasic	KH_2PO_4
Potassium phosphate dibasic trihydrate	$K_2HPO_4{\cdot}3H_2O$

3.3 Materials Design and Synthesis

This content portion gives a brief introduction of various methods which have been used during the material design and synthesis. The section has been divided into several small parts, every part is one kind of method, including: hydrothermal reaction, phosphorization, annealing treatment, and ion exchange strategy.

3.3.1 Hydrothermal Reaction

Hydrothermal reaction is the general term, which refers to the chemical reactions that were carried out in water, aqueous solution or steam. The reaction conditions were usually under a certain temperature and pressure. Hydrothermal reaction is a crucial role during the field of material design and synthesis due to its advantages of the flexibility and the handleability. The hydrothermal equipment consists of two parts. The external part is the stainless steel

and the internal part is made of the polytetrafluoroethylene (PTFE) texture. The feature function of the external stainless steel was used as the support matrix to protect the PTFE lining and form the certain pressure. Because the PTFE materials could not bear high temperature, thus the usual hydrothermal temperature is no higher than 220 ^{o}C. The internal capacity of reaction solution was no more than 2/3 of the labelled volume according to the

Figure 3.2 The unique designed hydrothermal device, the internal volume is 800 mL.

requirement of the security issue. The reaction devices usually have three different capacity sizes: 25 mL, 50 mL and 100 mL. To meet the special experimental demand such as high temperature, large-scale preparation, micropreparation or unique size, the internal materials, volume or shape of hydrothermal devices could be designed, as shown in **Figure 3.2**. This hydrothermal method also could be extended to other solutions, such as ethanol or other organic solutions to form the solvothermal strategy. During this thesis, our choice hydrothermal device during our research work is the normal 50 mL volume. In the experimental work, we has prepared the precursor, nickel hydroxide nanoarrays or Ni-Fe LDH in the chapter four via the hydrothermal strategy or the crystalline cobalt oxide in chapter six via a hydrothermal-then annealing method.

3.3.2 Phosphorization

The transition metal phosphides have been widely studied in various fields for the advantages of their high-efficiency activities. The current methods to prepare the phosphides can be divided into two categories according the phosphorus sources: inorganic phosphorus sources and organophosphorus.[1] Herein, we pay more attention to inorganic phosphorus sources because the organophosphorus such as trioctylphosphine (TOP) or triphenyl phosphine (TPP) are relatively more expensive. The inorganic phosphorus sources include the elemental phosphorus, phosphates, hypophosphites or other types. During the doctoral study, the phosphorus source we chose is sodium hypophosphite.

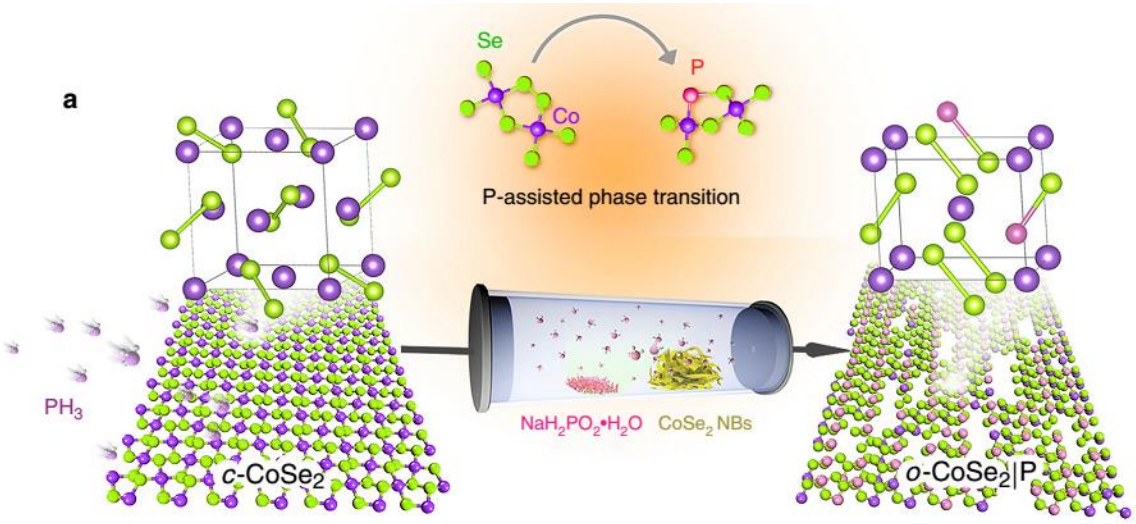

Figure 3.3 Schematic illustration of the P-doping into $CoSe_2$ to induce the structural phase transition during a facile annealing process from the work of Yu's group.[2]

Sodium hypophosphite can be in-situ decomposed into PH_3 during a facile annealing process, which enable the formation of phosphides or P-doping. For example, the recent reported work of Yu's group presents the P-doping into Co-Se_2 to induce the phase transition, the synthesis process was shown in **Figure 3.3**.[2] During this phosphorization

process, the morphology of the precursors usually could be retained, thus resulting in the wide applications during various areas. The challenge is the toxic and corrosive property of the generated PH_3 gas during phosphorization. To solve this problem, we use a copper sulfate aqueous solution or alkaline solution as the tail gas treatment and if possible, fume cupboard also could be used. In chapter four of this thesis, the phosphorization treatment was employed to synthesize the unique nickel phosphide nanoarrays.

3.3.3 Annealing

Annealing is one of the famous heat treatment methods. During the annealing process, materials could be heated to a certain temperature with an appropriate heating rate, then maintain at this temperature for a suitable time, finally cooled at a befitting rate. The frequently used annealing equipment in the laboratory was Muffle furnace or tube furnace. For the tube furnaces, the quartz or corundum tube can be selected according to

Figure 3.4 The photograph of the tube furnace used during the doctoral study.

the different produced atmosphere such as alkaline or acidic. Herein, the tube furnace was our choice, as shown in **Figure 3.4**, because of the usage of flowing argon inert atmosphere.

During the doctoral study, the preparation of the unique nickel phosphide nanoarrays and cobalt oxide synthesis were via the annealing treatment. During phosphorization, the annealing was utilized to provide an applicable temperature for the formation of PH_3 gas and the flowing Ar atmosphere gives the PH_3 gas an excellent mobility. During the cobalt oxide synthesis, the annealing treatment changed the cobalt-based hydroxide precursor into the produced cobalt oxide, and the inert atmosphere was used to protect its no further oxidation.

3.3.4 Ion Exchange Strategy

Ion exchange reaction refers to the process during which the exchange reaction was carried out between the cations or anions and the precursors via a solution containing the exchange ion. The induced heterogeneous ions bring the variation in the morphology, structure or composition of the obtained materials, tailoring their functional properties. Thus, the ion exchange strategies have been widely used in various fields. In this doctoral research work, we had used the sulfur ion exchange strategy to introduce the disordered structure into the previous crystalline cobalt oxides. The exchange reaction was operated in the Na_2S aqueous solution at room temperature, a series of the control experiments was conducted via varying the reaction times.

3.4 Materials Characterizations

3.4.1 X-ray Diffraction

When the inner electrons of an atom were bombarded by the high-speed moving electrons, the optical radiation X-ray would be generated during the transition reaction. Light

interference occurs via the coherent scattering generated from the numerous particles when X-ray traverses the crystalline structure, resulting in the stronger or weaker scattered X-rays. Bragg equation was as the following:

$$n\lambda=2d\sin\theta \quad (1)$$

where n: diffraction series, λ: X-rays irradiation wavelength, d: interplanar spacing and 2θ: diffraction angles. The Bragg equation was used to reflect the relationship between the diffraction direction and crystalline structure. Thus, X-ray diffraction (XRD) measurement can be used to analyze the phase and crystal structure of the obtained samples. During this thesis, the disordered level of S-CoO_x were estimated mainly according to the analysis of XRD patterns.

3.4.2 Scanning Electron Microscopy

Scanning electron microscope (SEM) is the microscopic observation technique which was invented to observe the surface morphology of the samples due to the secondary electronic signal imaging. The used SEM equipment during the doctoral study was as shown in **Figure 3.5**. SEM plays a vital role during the investigation of morphology analysis, especially for the nanomaterials. In the doctoral study, the SEM equipment is Zeiss Supra 55VP, equipped with the energy dispersive spectroscopy (EDX) device. During SEM measurement, sample preparation, the used voltage or operating method were also important to obtain a high qualitied SEM image. During this thesis, the achieved smooth nanowire precursor morphology, nickel hydroxide ($Ni(OH)_2$) nanoarray morphology, nickel phosphide (Ni_2P) nanoarray morphology of chapter four and chapter five, or the smooth

cobalt oxide nanowires, unique morphology of the formed S-CoO_x of chapter six were all investigated via the SEM image measurement.

Figure 3.5 The photograph of the SEM equipment used during the doctoral study.

3.4.3 Transmission Electron Microscopy

In 1932, transmission electron microscope (TEM) was invented by Ruska, with the electron beams as a light source. The used TEM equipment during this thesis was as shown in **Figure 3.6**. To further analyze the morphology of the samples, TEM was utilized with the capacity to operate at higher voltages and form image at a higher resolution. Besides, the lattice fringe or other detailed structure information also could be examined via the high resolution TEM (HRTEM) images. Selected area electron diffraction (SAED) and HRTEM-EDX mapping images also demonstrate the further phase features and elemental distributions. During the doctoral study, the disordered areas and the distorted lattice fringe

arrangement of S-CoO_x were confirmed via the combination usage of the TEM and HRTEM, SAED and HRTEM-EDX mappings images.

Figure 3.6 The photograph of the TEM equipment used during the doctoral study.

3.4.4 Raman Spectroscopy

Raman spectroscopy is a molecular spectroscopy based on the Raman scattering effect which was discovered by the Indian scientist Raman in 1928. Raman spectroscopy was one of the most important detection means to analyze the structure information of the samples due to the specific vibrations from molecular bonds and symmetry. Thus, the newly emerging, disappeared or shifted peaks in Raman spectra all exhibit the changed structure information in sample. The used Raman device is as shown in **Figure 3.7**. In the doctoral study, Raman spectroscopy was used to check the change formation from the precursor to nickel hydroxide (chapter four) and investigate the peak shifts in S-CoO_x (chapter six).

What we should pay attention is that not all the samples have the specific Raman peaks, some materials show no peaks in Raman spectra.

Figure 3.7 The photograph of the Raman device used during the doctoral study.

3.4.5 Brunauer-Emmett-Teller (BET) Measurement

The surface area of materials is the vital factor during the material design areas, such as the high surface area is the important requirement of the energy storage field to store more active sites or other exposed materials. N_2 sorption/desorption measurement was used to analyze the surface area of the samples via the usage of a Micromeritics 3Flex analyzer. The equipment is as shown in **Figure 3.8**. The samples' surface area was evaluated via Brunauer-Emmett-Teller (BET) method, which collects the recorded experiment points to calculate the values of samples' surface areas. Meanwhile, the Barret-Joyner-Halenda (BJH) method was used to calculate the pore size distribution during the prepared samples. During the doctoral research study, BET method was used to analyze the surface area of the collected S-CoO_x powder which was removed from the nickel foam substrate (NF) of the obtained S-CoO_x/NF (chapter six).

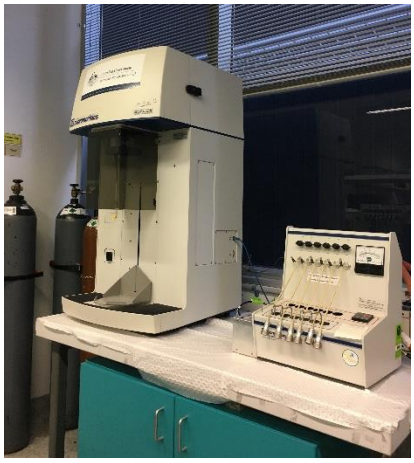

Figure 3.8 The photograph of the Brunauer-Emmett-Teller (BET) used to analyze the samples' surface area during the doctoral study.

3.4.6 Contact Angle Measurement

The contact angle usually refers to the formed angle between the gas-liquid or solid-liquid interface at the solid-liquid-gas three phase junction interface. Contact angle test was mainly used to measure the contact angle of the liquid-solid interface by dropping a droplet onto the solid materials' horizontal plane, via a standard CCD camera and the continuous magnification microscope lens. To check the "superaerophobic" surface property of nickel phosphide nanoarrays, the contact angle test is required. During the contact angle test, the hydrogen or air bubbles were released via a curved needle, the releasing bubbles arises in the solution to have a contact with the samples' surface, then the camera records a series of the sequential results.

3.4.7 X-ray Photoelectron Spectroscopy

X-ray photoelectron spectroscopy (XPS) is the technique to analyze the surface elemental composition and elemental valence states of the obtained materials. The work principle of XPS is that the valence electrons or the inner layer electrons of the atoms or molecules

were excited out when X-rays irradiates the samples. During this process, electrons which were excited out by the photons are named as the photoelectrons. With the photoelectron kinetic energy/binding energy as x-coordinate and the relative intensity as the y-coordinate, a photoelectron energy spectrum can be obtained. The XPS spectra demonstrate the structural information of the samples. XPS technique only can collect the surface information from about 0 to 10 nm of the prepared materials. XPS survey spectra show the existence of the element compositions from the samples, high-resolution elemental spectra were used to analyze the chemical states or other further information. In chapter four and chapter six of the thesis, the chemical states and element compositions of the prepared materials were evaluated via the XPS measurement.

3.4.8 Density Functional Theory

Density functional theory (DFT) calculation is one of the various computing models, which can be used to analyse the physical or chemical features of the simulation model according to the prepared materials. During the chapter six, the density of states, hydrogen adsorption Gibbs free energy (ΔG_H) and the Gibbs free enegy changes (ΔG) during OER were calculated via the DFT to give the insight analysis of cobalt oxide (CoO_x) and S-CoO_x materials.

3.5 Electrocatalytic Measurements

In this section, the electrocatalytic activities of the prepared materials were investigated. The device for HER or OER is the three-electrode system, with the prepared materials as the working electrode, Ag/AgCl electrode or saturated calomel electrode as the reference electrode, the carbon rod as the counter electrode. The overall water splitting device is a

two-electrode system with the anode and cathode. The main electrolyte is alkaline aqueous solution.

3.5.1 Electrode Preparation

During the electrocatalytic systems, the working electrodes were prepared with our synthetic materials. The achieved materials such as $Ni(OH)_2$/NF, Ni_2P/NF, Ni-Fe LDH/NF, CoO_x/NF or S-CoO_x/NF were all the freestanding three-dimensional materials. These materials could be directly used as the working electrodes without any further treated. Besides, the comparison experiments such as the commercial noble metal Pt/C (20 wt%), Ir/C (20 wt%) or the prepared Co-S were the powder materials. To prepare these powder materials as the working electrodes, 5 mg of the catalysts were dispersed in 1 mL ethanol and 40 μL 5% Nafion. The homo-disperse suspension was formed during the ultrasonic dispersion process. Then suspension solution containing the catalysts was dropped onto a clean nickel foam substrate which was later used as the working electrodes. The loading amount of the catalysts is corresponding with that of the achieved catalysts grown on the fore-mentioned free-standing samples.

3.5.2 Polarization Curves

The polarization curve was one of the most important indexes which were used to evaluate the electrocatalytic property of a catalyst during both three-electrode and two-electrode systems. The polarization curve was plotted via the recorded points with the applied potential or overpotential as the x-axis and the current density as the y-axis. The overpotential (η) is the potential difference between the achieved potentials at a current density with its thermodynamic potential (1.23 V for OER and 0 V for HER). A lower

overpotential means a more efficient consumed electric energy. The current densities we used during the doctoral study were calculated via the geometric electrode area. The polarization curves provide the onset potential values or the overpotential η_{10} values for the catalysts during the electrocatalytic performances. Onset potential was the overpotential required at the starting of an obvious current density for a catalyst. The η_{10} is the overpotential when the current density is 10 mA cm^{-2}. Both the onset potential and η_{10} are crucial factors to reflect the intrinsic activity and evalute the catalytic property for the prepared materials. A lot of the reported HER, OER, or overall water splittting research literatures have provided the comparison figures or tables for the onset potential or η_{10} values among the highly efficient electrocatalysts.[3-5]

3.5.3 Tafel Plots

The slope of the Tafel plots plays a vital role during electrocatalytic system. Tafel slope could be calculated according to the obtained from the measured polarization curves. A lower slope value of the Tafel slope usually suggests a superior catalytic activity for the achieved materials because that means a higher increased rate of current density at the same applied potential interval. Thus, a low Tafel slope is required for a highly active electrocatalysts. To assess the reaction kinetics, the Tafel slope (b) was evaluated via fitting the linear portion of Tafel plots which were replotted as overpotential (η) versus log current ($\log j$). The equation is as following:[2]

$$\eta = a + b.\log(j) \qquad (2)$$

A smaller value of Tafel slope demonstrates a supervior reaction kinetic.Thus, the desired electrocatalysts should have a lower overpotential and a smaller Tafel slope.

3.5.4 Electrochemical Impedance Spectroscopy

Electrochemical impedance spectroscopy (EIS) is a very useful electrochemical analysis tool which were widely used during the numerous areas such as electrocatalysis, batteries, or other electro-chemical systems.[6] EIS Nyquist plots of the catalysts include Z' and Z'', Z' is the real impedance, and the Z'' is the imaginary impedance. The EIS Nyquist plots for the obtained materials were recorded to probe the charge transfer process during the electrochemical activities. The smaller charge transfer resistance (R_{ct}) recorded from the EIS Nyquist plots demonstrate an enhanced charge transfer kinetics, which would be advantageous to the electrocatalytic activities. In the doctoral study, EIS Nyquist plots of different prepared materials in one electrochemical system were acquired ranging from 100 kHz to 0.1 Hz amplitude of 5 mV under the constant overpotential. The smaller R_{ct} values would result in a superior catalytic property.

3.5.5 Double-Layer Capacitances

The double-layer capacitances (C_{dl}) was used to roughly evaluate the effective electrochemically active surface area of the measured catalysts. In this thesis, C_{dl} plots were collected via the cyclic voltammetry (CV) curves under non-active catalytic regions with the scanning rates from 20 mV s^{-1} to100 mV s^{-1}. Then, the C_{dl} values was calculated using the CV results obtained at the different scan rates according to the following formula:[7]

$$i_c = \nu \cdot C_{dl} \quad (3)$$

Where i_c is the charging current density and ν represents the scan rate.

The bigger C_{dl} values of the measured catalysts suggest that the more exposed active sites were created, providing a vital route to design highly active electrocatalysts.

3.5.6 Stability Measurements

Besides the above-mentioned electrochemical activities, stability is also the important and critical parameter during the various application of the active catalysts. During the doctoral study, we have used a series of different measurement methods to check the catalysts' stability capacity. In the details, the long-term chronoamperometry test was used at the constant applied potential. The long-term chronopotentiometry test was conducted at the constant current density. Multi-chronoamperometric response test was operated at the various constant applied potentials. Multi-step chronopotentiometry test was run at the various constant applied current densities. The accelerated cyclic polarization curves were obtained during the process cyclic polarization curves. All the measurements were utilized to check the catalytic performances during the long-term electrocatalytic operation systems. A good catalyst should possess the features of both the excellent stability and highly efficient catalytic property.

3.6 Summary

During this chapter, the chemicals used during this thesis have been listed. The material synthesis methods involved during the thesis, including hydrothermal reaction, annealing, phosphorization and ion exchange strategy have been briefly discussed. The various material characterizations such as XRD, SEM, TEM, XPS, Raman, BET, DFT and contact angle measurement all have been given in a brief description. Moreover, the important sections about the electrochemical measurements consisting of the electrode preparation

and electrochemical performances have also been described in a short statement. In brief, the various material characterizations and electrochemical measurements should be combined to analyze for the comprehensive understanding of the prepared materials.

3.7 References

1. Shi, Y. and B. Zhang, *Recent advances in transition metal phosphide nanomaterials: synthesis and applications in hydrogen evolution reaction.* Chem. Soc. Rev., 2016. **45**(6): p. 1529-1541.

2. Zheng, Y.-R., et al., *Doping-induced structural phase transition in cobalt diselenide enables enhanced hydrogen evolution catalysis.* Nat. Commun., 2018. **9**: p. 2533.

3. Luo, M., et al., *PdMo bimetallene for oxygen reduction catalysis.* Nature, 2019. **574**(7776): p. 81-85.

4. Yu, X., et al., *"Superaerophobic" nickel phosphide nanoarray catalyst for efficient hydrogen evolution at ultrahigh current densities.* J. Am. Chem. Soc., 2019. **141**(18): p. 7537-7543.

5. Zhang, J., et al., *Single platinum atoms immobilized on an MXene as an efficient catalyst for the hydrogen evolution reaction.* Nat. Catal., 2018. **1**(12): p. 985-992.

6. Andre, D., et al., *Characterization of high-power lithium-ion batteries by electrochemical impedance spectroscopy. I. Experimental investigation.* J. Power Sources, 2011. **196**(12): p. 5334-5341.

7. Lukowski, M.A., et al., *Enhanced hydrogen evolution catalysis from chemically exfoliated metallic MoS_2 nanosheets.* J. Am. Chem. Soc., 2013. **135**(28): p. 10274-10277.

Chapter 4 Synthesis and Characterization of the Unique Nickel Phosphide Nanoarray Structure

4.1 Introduction

During large-scale catalytic hydrogen evolution reaction, tremendous quantities of H_2 bubbles will be rapidly formed at the high current densities. The aggregation of gas bubbles on the contact surface between the catalysts and the electrolyte severely hinders liquid mass transport process, thus slowing the electron transfer and decreasing the number of exposed active sites. These phenomena will lead to inferior electrocatalytic activity and poor stability in the electrocatalytic system[1]. The challenging dilemma in advancing industrial hydrogen production is to detach the formed H_2 bubbles to retain the catalytic ability of the electrode. This expectation has been described by the pioneering works from the Jin's[2] and Sun's[3] groups. It was observed that "superaerophobic" surface structures could be assembled via the formation of an array architecture[4], which is indispensable for large-current-density hydrogen production due to their superior ability to release the formed gas bubbles[2,3].

Herein, we report the preparation of a Ni_2P nanoarray catalyst grown on a nickel foam substrate (denoted as Ni_2P/NF), where the Ni_2P nanosheets are evenly distributed on Ni_2P nanowire arrays, forming a unique nanoarray structure. The unique assembly of the Ni_2P/NF provides a preferred "superaerophobic" structure, which is preferable to release the in-situ generated gas bubbles. The synthesis process demonstrates a promising route to prepare the "superaerophobic" material architectures, meeting the requirements of scalable H_2 production at large current densities.

4.2 Experimental Sections

4.2.1 Chemicals

All the chemicals including hydrochloric acid (HCl), ethanol (CH_3CH_2OH), diammonium hydrogen phosphate ($(NH_4)_2HPO_4$), potassium hydroxide (KOH), sodium hypophosphite monohydrate ($NaH_2PO_2H_2O$), ferric nitrate nonahydrate ($Fe(NO_3)_3 \cdot 9H_2O$), copper nitrate hemi(pentahydrate) ($Cu(NO_3)_2 \cdot 21/2H_2O$), and nickel nitrate hexahydrate ($Ni(NO_3)_2 \cdot 6H_2O$) were used as received without any further purification.

4.2.2 Synthesis of $Ni(OH)_2$/NF Nanoarrays

Prior to the synthetic procedures, commercial nickel foam (NF) was cut into 2.5 x 2.5 cm^2 plates, then were compressed into thinner ones to improve the wettability. Nickel foam were sequentially ultrasonically treated in 3 M hydrochloric acid (HCl) aqueous solution, deionized water and ethanol to remove the surface oxides and organic molecules, then dried in vacuum oven at 60 ºC. The $Ni(OH)_2$/NF was obtained via a two-step hydrothermal method. First, the clean nickel foam plate was immersed in a 35 mL of uniform transparent aqueous solution containing $(NH_4)_2HPO_4$ (1mM). Sequentially, the sealed 50 mL autoclave was retained at 180 ºC for different times to prepare the precursors. The achieved green precursors were washed several times with deionized water and dried in air. Then, another mild hydrothermal process was utilized to achieve the desired $Ni(OH)_2$/NF. In a typical procedure, the green precursor was transformed into a 50 mL Teflon-lined stainless steel autoclave containing 30 mL of 0.1 M KOH aqueous solution. Subsequently, the autoclave was kept at 120 ºC for 5h. After cooling down to room temperature, the light grey $Ni(OH)_2$/NF nanoarrays were rinsed with deionized water and dried in air. The

temperature-control experiments were also operated while the reaction time was fixed and experiment temperatures were adjusted as needed to obtained the corresponding materials.

4.2.3 Synthesis of Ni_2P/NF

The Ni_2P/NF was prepared via a low-temperature calcination method. The fresh obtained $Ni(OH)_2$/NF and $NaH_2PO_2H_2O$ with a weight ratio of 1:10, were put into a same ceramic boat at two separated places, while $NaH_2PO_2H_2O$ is at the upstream side. After excluding air for 30 min in a flowing Ar at room temperature, the samples were maintained at 300 °C for 30 min with a heating rate of 5 °C /min under a flowing Ar atmosphere. After naturally cooling down to room temperature, the achieved black samples were collected for further tests. A series of the control experiments including experimental temperatures, times, heating rates or the used gas flow were also operated as the comparisons.

4.2.4 Characterization

X-ray powder diffraction (XRD) pattern was examined via a Japan Rigaku DMax-γA X-ray diffractometer equipped with Cu Kα radiation (λ = 1.5406 Å). Scanning electron microscope (SEM) images were investigated on a Zeiss Supra 40 at 5 kV. Transmission electron microscope (TEM) images were measured through a JEOL 2010F(s) at 120 kV. High-resolution TEM (HRTEM) images, selected-area electron diffraction (SAED), energy dispersive X-ray (EDX) spectra and elemental mappings images were all obtained on an Atomic Resolution Analytical Microscope JEM-ARM 200F, operating at 200 kV. Raman spectra were obtained via a Raman microscope (Renishaw®), excited with a 514 nm excitation laser. X-ray photoelectron spectra (XPS) spectra were performed on an X-ray photoelectron spectrometer of ESCALab MKII, equipped with an X-ray source (Mg Kα) at

$h\upsilon$ = 1253.6 eV. Contact angles were analyzed via an OCA20 machine (Data-Physics, Germany) at room temperature.

4.2.5 Electrocatalytic Measurements

Electrochemical activities were operated via a Multipotentiostat (IM6ex, ZAHNER elektrik, Germany) in a traditional three-electrode system at room temperature, using a graphite rod and a saturated calomel electrode as the counter electrode and the reference electrode, respectively. The prepared samples were used as the working electrodes and the electrolyte was 1 M KOH aqueous solution. Potentials described during this work without any special statement were normalized versus the reversible hydrogen electrode (RHE), according to the equation: $E_{RHE} = E_{applied} + 0.241 + 0.059$ x pH. Where the $E_{applied}$ is the applied potential. Polarization curves were performed via sweeping the potentials at a rate of 10 mV s^{-1}. Electrochemical impedance spectroscopy (EIS) test were acquired ranging from 100 kHz to 0.1 Hz at the amplitude of 5 mV.

4.3 Results and Discussion

4.3.1 Material Synthesis and Characterization

The Ni_2P/NF catalyst was synthesized via annealing $NaH_2PO_2H_2O$ with $Ni(OH)_2$ nanoarrays which were grown on nickel foam (denoted as $Ni(OH)_2$/NF) under a flowing argon atmosphere. The $Ni(OH)_2$/NF nanoarrays were obtained via a two-step hydrothermal method as described in the experimental section. **Figure 4.1a** illustrates the whole synthesis process which could be divided into three steps (**Figure 4.2**). In the first step, the free-standing precursor was prepared through a direct thermal reaction between $(NH_4)_2HPO_4$

and nickel foam during the hydrothermal process. Several control experiments were operated at 180 ºC with different reaction times. Scanning electron microscopy (SEM) images show that smooth nanowire array morphology for the precursor obtained at 180 ºC for 12 h is even-distributed on the nickel foam substrate without agglomeration, thus the precursor obtained at 180 ºC for 12 h was chosen to be further studied (**Figure 4.3**).

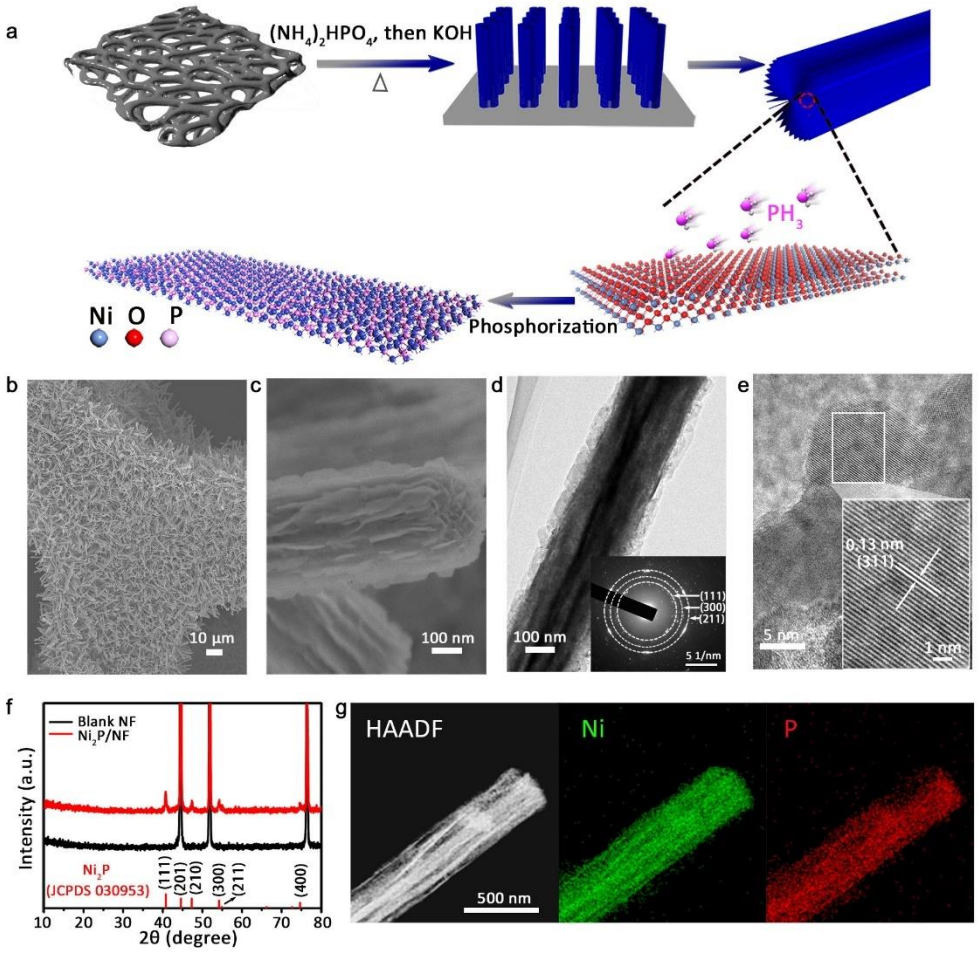

Figure 4.1 a) Schematic illustration of the synthetic process for Ni_2P nanoarrays. (b, c) SEM, (d) TEM, (e) HRTEM, (g) STEM-EDX mapping images of the obtained Ni_2P/NF. (f) XRD patterns of Ni_2P/NF and blank NF. The inset in (d) is the corresponding SAED pattern.

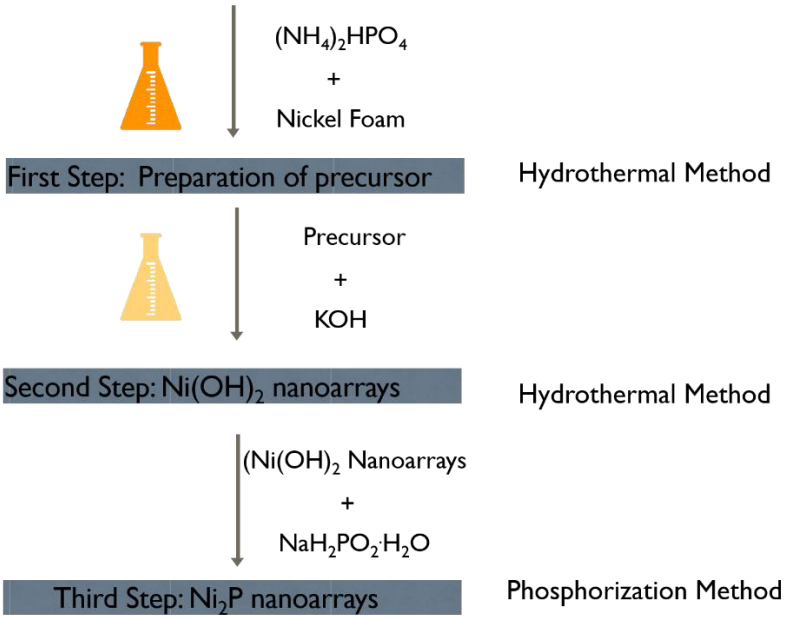

Figure 4.2 The three steps during the systhesis process of nickel phosphide nanoarrays.

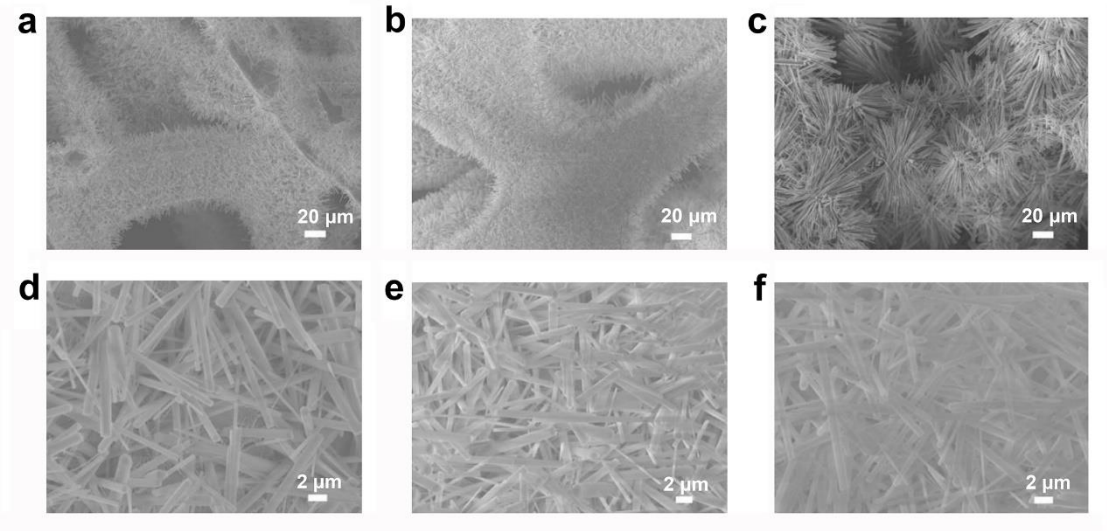

Figure 4.3 SEM images of the precursors obtained via a direct thermal reaction between $(NH_4)_2HPO_4$ and nickel foam at 180 ºC for (a, d) 6 h, (b, e) 12 h, (c, f) 24 h.

Transmission electron microscopy (TEM) images confirm the formation of nanowires with a diameter of ~250 nm. Elemental mapping and energy dispersive X-ray (EDX) spectra

evidence the existence of Ni, O and P elements (**Figure 4.4**). In the second step, the precursors were hydrothermally treated with KOH aqueous solution to form the nickel hydroxide nanoarrays grown on the nickel foam substrate. The morphology transforms from smooth nanowires to a hybrid three-dimensional (3D) nanostructure, as shown in **Figure 4.5**. The hybrid morphology stucture mainly consists of nanowires and nanosheets, where the nanosheets are uniformly embedded in nanowires. At a low hydrothermal temperature such as 80 ºC, the tenuous nanosheets were scattered across the surface of nanowires. With the increased hydrothermal temperatures, the external nanosheets become more intensive and larger. The nanosheets already could be evenly distributed over the nanowires when the hydrothermal temperature reach at 120 ºC. At higher temperatures, the phenomena were more obvious.

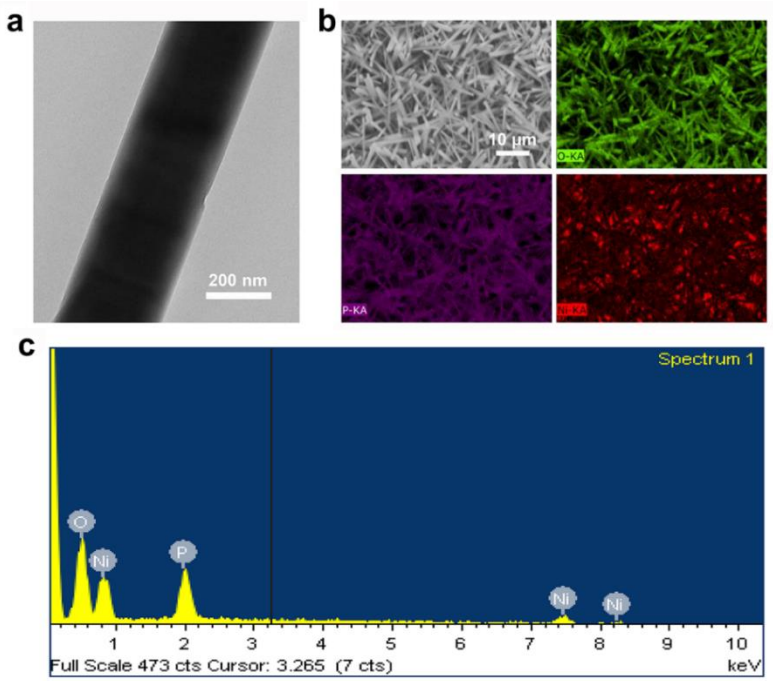

Figure 4.4 (a) TEM image, (b) elemental mapping and (c) EDX spectra of the precursor obtained via a direct thermal reaction between $(NH_4)_2HPO_4$ and Ni foam at 180 ºC for 12 h.

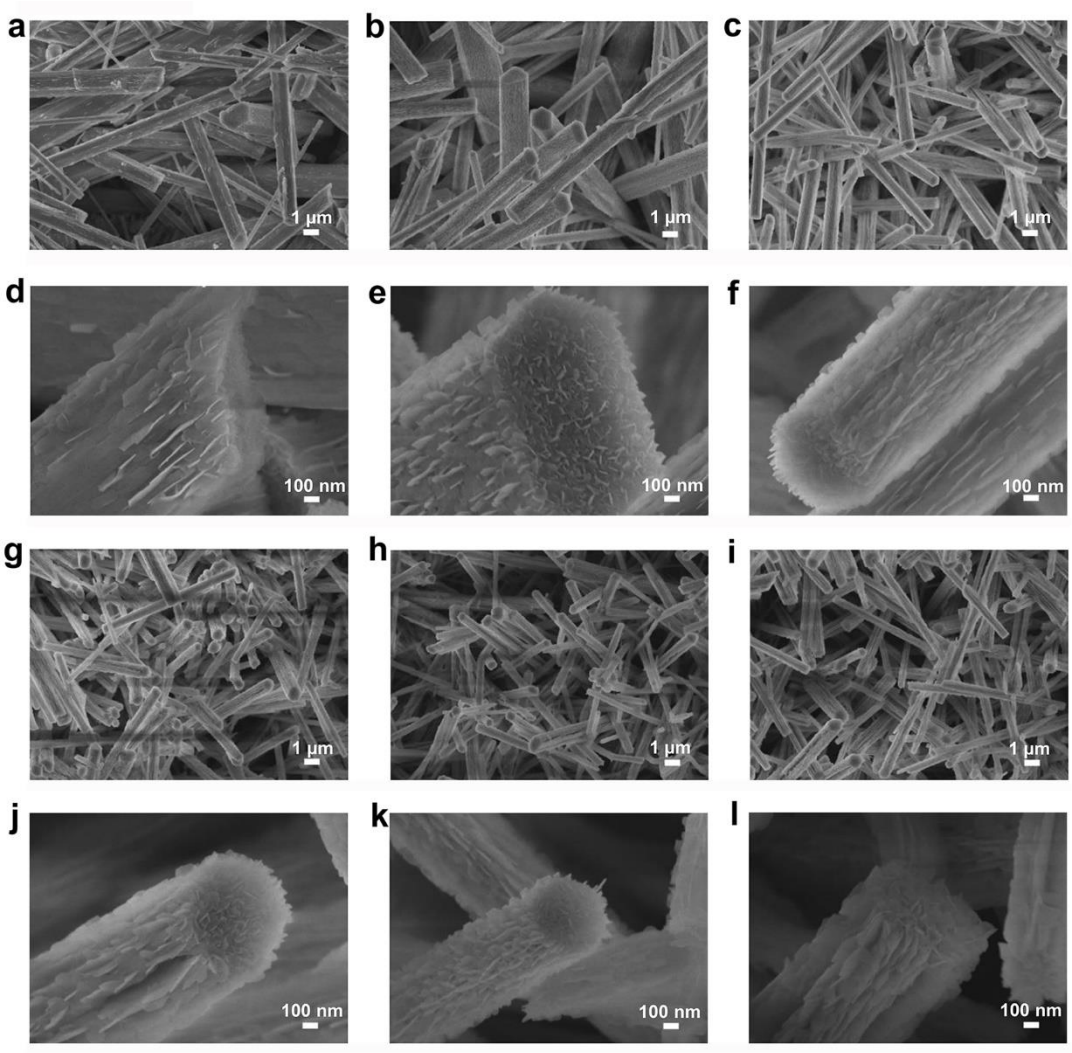

Figure 4.5 SEM images of the treated precursors in a 0.1 M KOH aqueous solution via a hydrothermal method at (a, d) 80 ºC, (b, e) 100 ºC, (c, f) 120 ºC, (g, j) 140 ºC, (h, k) 160 ºC, (i, l) 180 ºC for 5 h. SEM images reveal that the nanosheets which are grown on the nanowires become more obvious at a higher temperature.

X-ray powder diffraction (XRD) patterns and Raman spectra reveal that the precursor has been gradually changed into $Ni(OH)_2$ nanoarrays during the second-step hydrothermal process. At a higher temperature, the precursors were completely transformed into $Ni(OH)_2$ with a hexagonal phase (JCPDS 14-0117) (**Figure 4.6**)[5,6]. The transformation process was

speculated as follows. Firstly, $(NH_4)_2HPO_4$ directly reacted with nickel foam, which

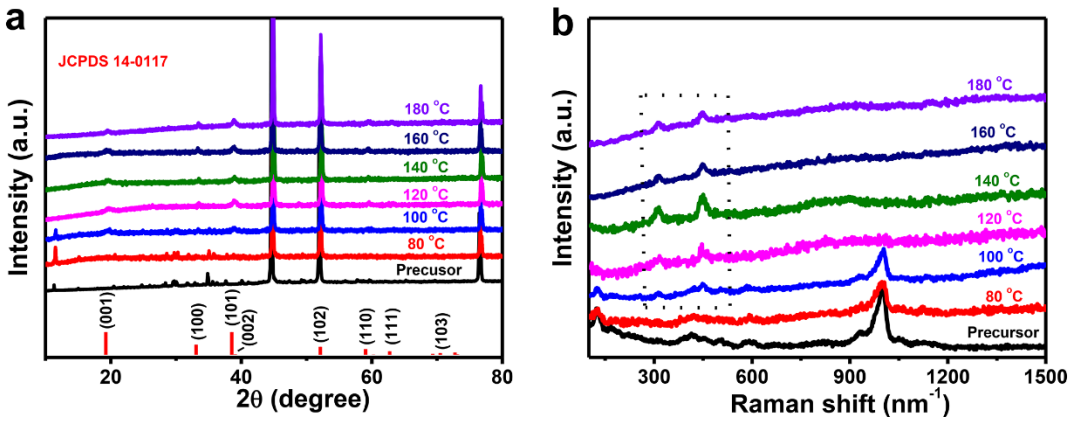

Figure 4.6 The change process of (a) XRD patterns and (b) Raman spectra for the precursors before and after treatment in a 0.1 M KOH aqueous solution at different hydrothermal temperatures for 5 h. XRD and Raman analysis show the precursors have been successfully transformed into $Ni(OH)_2$ at a higher temperature (>100 ºC).

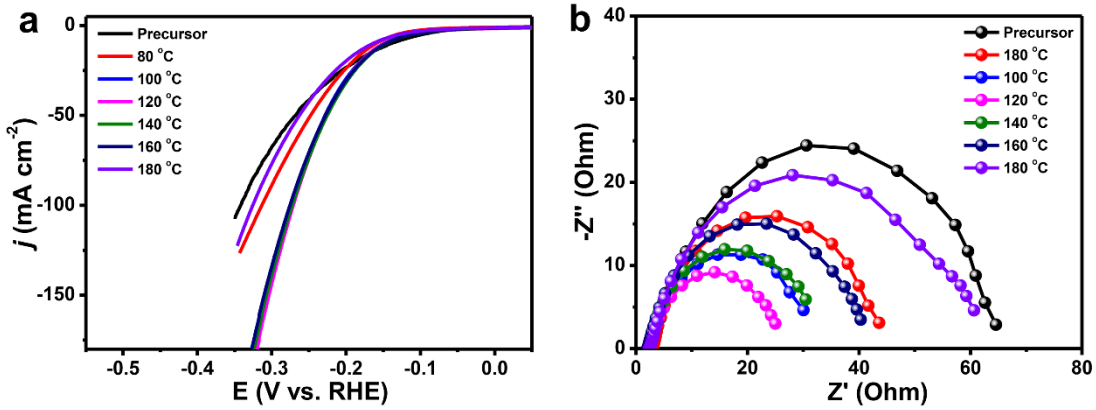

Figure 4.7 Electrocatalytic HER performances. (a) Polarization curves with a scan rate of 10 mV s^{-1} and (b) EIS Nyquist plots at the overpotential of 100 mV for the obtained materials before and after treatment in a 0.1 M KOH aqueous solution at different hydrothermal temperatures. The prepared materials obtained at 120 ºC were chosen to be further investigated depending on their electrocatalytic HER performance.

provides sites for oriented growth of the nanowires during the reaction process, forming the nanowire array precursor. Then, the obtained nanowire precursors were transformed into the $Ni(OH)_2$ in a KOH aqueous solution via another hydrothermal treatment. This process causes the morphology change from nanowire array of the precursor to the unique $Ni(OH)_2$ nanoarrays. The optimal $Ni(OH)_2$ nanoarrays obtained at 120 ºC were chosen to be further investigated (**Figure 4.7**). TEM image also confirms that the external ultra-thin nanosheets

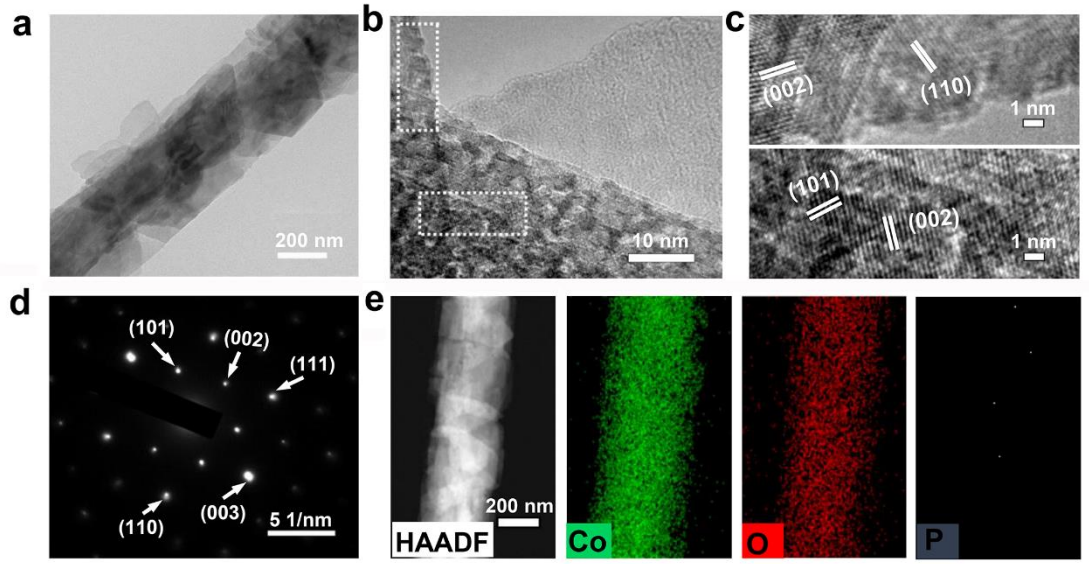

Figure 4.8 (a) TEM, (b, c) HRTEM, (d) the corresponding SAED and (e) STEM-EDX mapping images of the $Ni(OH)_2$ obtained after treatment in a 0.1 M KOH aqueous solution at 120 ºC for 5 h.

are arranged regularly on the nanowires (**Figure 4.8a**). Corresponding selected area electron diffraction (SAED) patterns reveal single-crystalline-feature of the as-prepared $Ni(OH)_2$. High-resolution TEM (HRTEM) images demonstrate the high crystallinity of $Ni(OH)_2$ with the resolved lattice fringes of (110), (002) and (101) planes. Scanning TEM (STEM) and elemental mapping images display the uniform distribution of Ni and O (**Figure 4.8b-e**). The analysis of Ni 2p and O 1s spectra elucidated that the main peaks at

855.6 eV and 873.4 eV could be assigned to Ni $2p_{3/2}$ and Ni $2p_{1/2}$. While, the metal-O peak is at 530.7 eV (**Figure 4.9**) [7].

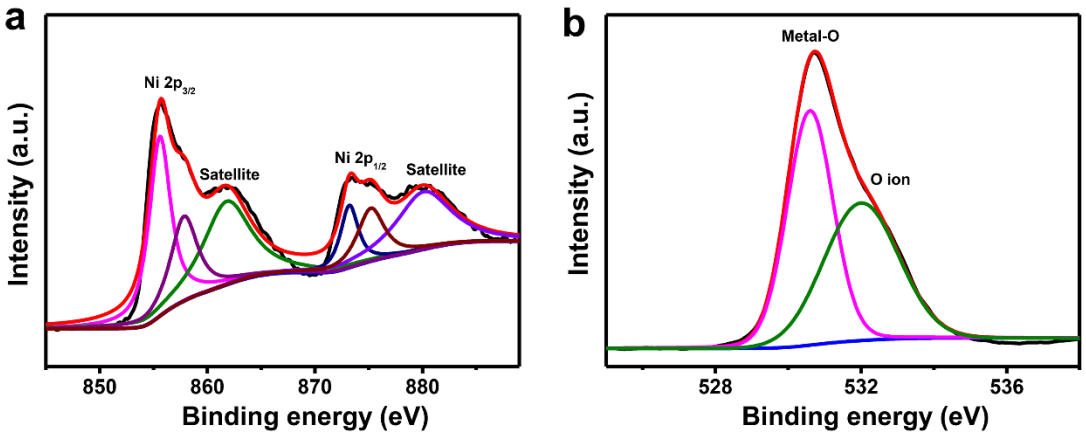

Figure 4.9 (a) Ni 2p spectra and (b) O 1s spectra of the $Ni(OH)_2$/NF obtained after treatment in a 0.1 M KOH aqueous solutio at 120 ºC.

The various control experiments including the reaction temperatures, reaction times, the heating rates and the gas flows were operated during the third reaction step-phosphorization process. The "superaerophobic" Ni_2P/NF nanoarrays were achieved via the phosphorization process by annealing the prepared $Ni(OH)_2$/NF with $NaH_2PO_2H_2O$. The reaction condition which was at 300 ºC for 0.5 h under an Ar flow at a heating rate of 5 ºC/min was the optimal condition (**Figure 4.10**). $NaH_2PO_2 \cdot H_2O$ was placed at the upper location, which can be decomposed to PH_3 species in situ during the annealing process, enabling the formation of Ni_2P. SEM and TEM images of the obtained Ni_2P show a uniform nanoarray morphology, inherited from the original $Ni(OH)_2$ precursor (**Figure 4.1b-d** and **Figure 4.11**). The corresponding SAED pattern reveals a polycrystalline feature, which can be easily distinguished from the single-crystal-like pattern of the $Ni(OH)_2$

precursor (**Inset** in **Figure 4.1d**). HRTEM images demonstrate distinct lattice fringes with

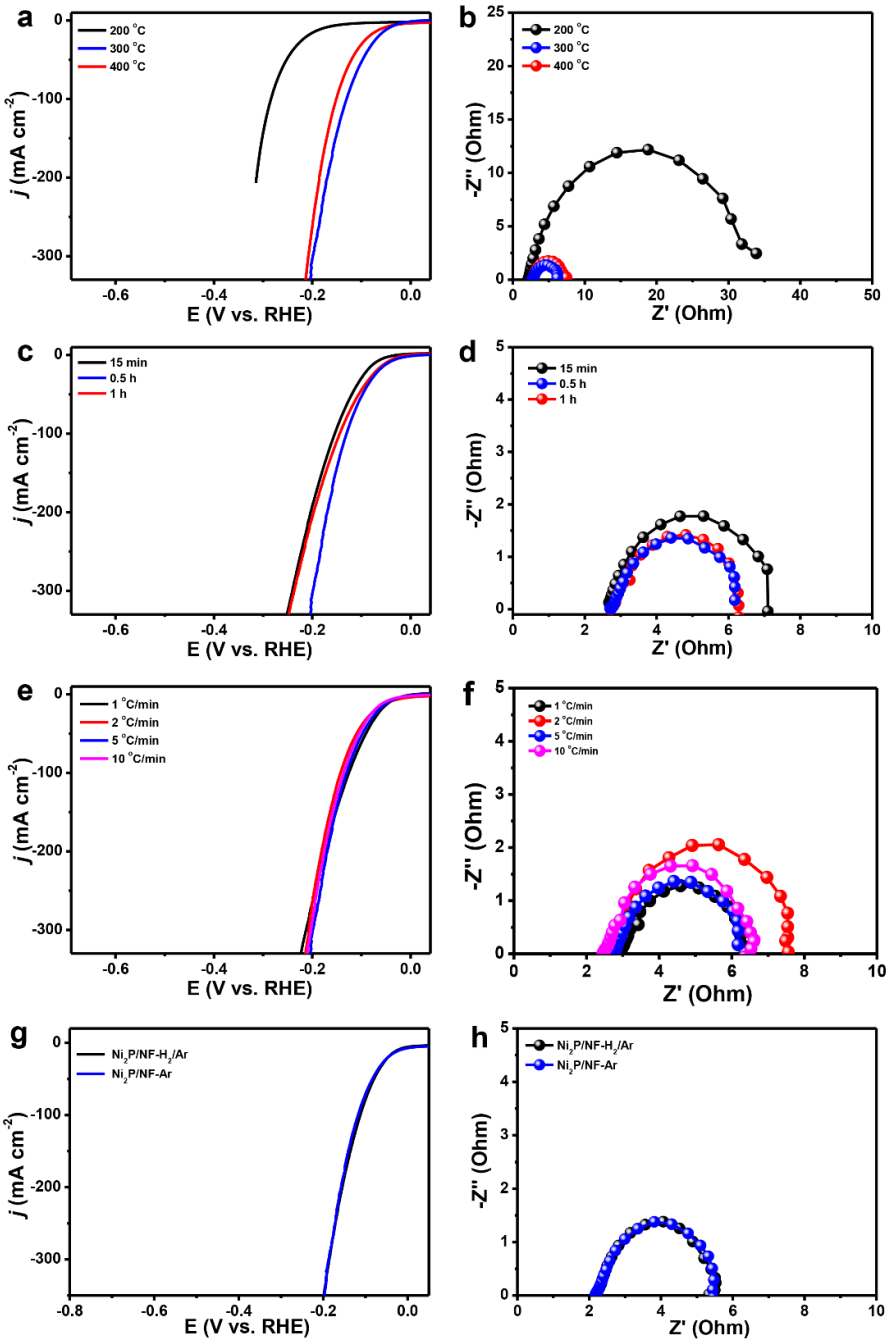

Figure 4.10 Polarization curves and EIS Nyquist plots at the overpotential of 100 mV for Ni_2P/NF obtained at different (a and b) temperatures, (c and d) times, (e and f) heating rates and (g and h) gas flow. The scan rate is 10 mV s^{-1}. The optimal Ni_2P/NF catalyst was achieved at 300 ºC for 0.5 h at the heating rate of 5 ºC/min under an Ar flow.

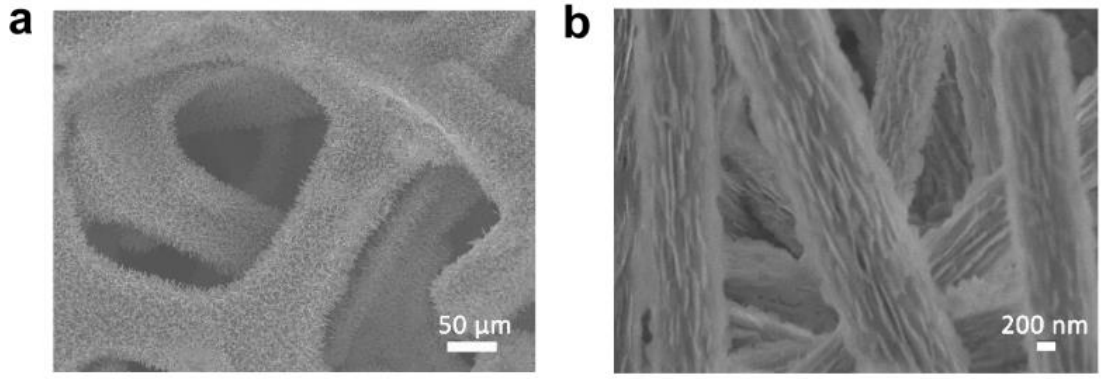

Figure 4.11 (a, b) SEM images of the prepared Ni_2P nanoarrays after annealing at 300 ºC for 0.5 h at 5 ºC/min in a flowing Ar.

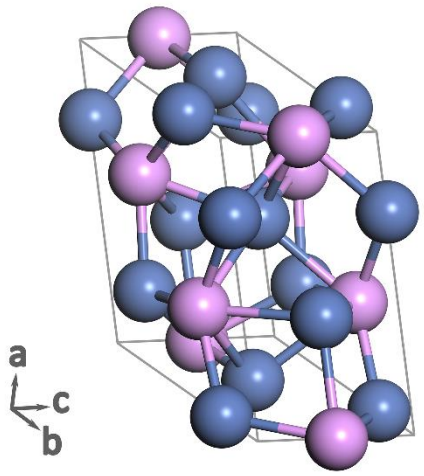

Figure 4.12 Unit cell of the hexagonal Ni_2P crystal structure. The lattice parameters are a = b = 5.86 Å, c = 3.37 Å and the space group is P321.

a spacing of 0.13 nm (**Figure 4.1e**), this lattice spacing could be attributed to the (311) plane of hexagonal Ni_2P (JCPDS 030953), which is consistent with the results from the XRD patterns (**Figure 4.1f**). The unit cell of the hexagonal Ni_2P and the atomic arrangement of (311) lattice plane were shown in **Figure 4.12** and **Figure 4.13**, respectively.

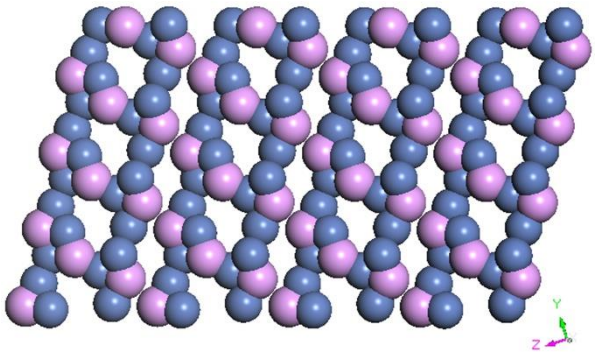

Figure 4.13 Atomic arrangement of (311) lattice plane for the obtained Ni_2P.

The STEM elemental mapping images of Ni_2P material demonstrate the existence of Ni and P elements, which are both uniformly distributed across the unique nanoarray morphology (**Figure 4.1g**). EDX patterns and XPS survey spectra of the Ni_2P sample further verify the existence of both Ni and P elements, as shown in **Figure 4.14** and **Figure 4.15a**. Ni 2p spectra analysis of the prepared Ni_2P shows that the two obvious peaks appear at 857.2 eV and 875.1 eV, which can be attributed to Ni $2p_{3/2}$ and Ni $2p_{1/2}$, respectively. The peak at 134.3 eV originates from P 2p, further confirming the existence of P element. These above results verify the successful generation of Ni_2P product (**Figure 4.15b-c**)[8-10]. The loading amount of Ni_2P on the nickel foam supporting substrate was determined to be ~3.83 mg cm^{-2}. Besides, we also note that this phosphorization approach can be extended to produce other transition metal phosphides, such as Ni_2P nanosheets, MnP-type FeP and Cu_3P (JCPDS 021263), proving the wide application of this facile phosphorization method (**Figure 4.16** and **Figure 4.17**). The unique structural features and solid adhesive connection with 3D nickel foam substrate will synergistically function together to provide excellent electrocatalytic properties.

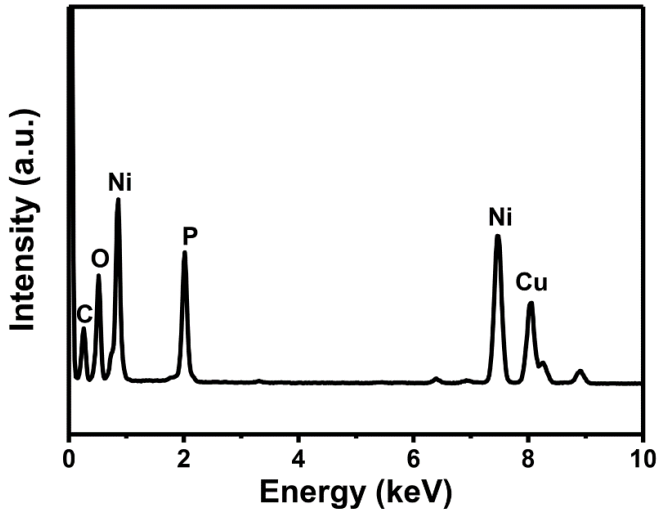

Figure 4.14 EDX pattern of the prepared Ni_2P nanoarrays after annealing at 300 ºC for 0.5 h at 5 ºC/min in a flowing Ar.

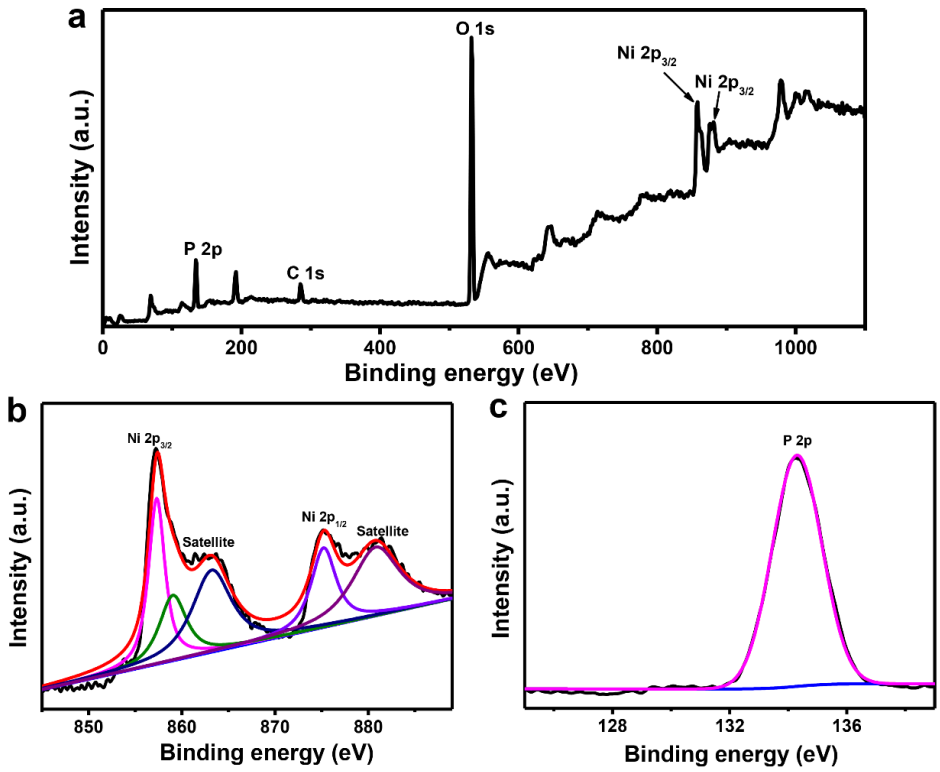

Figure 4.15 (a) XPS survey, (b) Ni 2p and (c) P 2p spectra of the prepared Ni_2P nanoarrays.

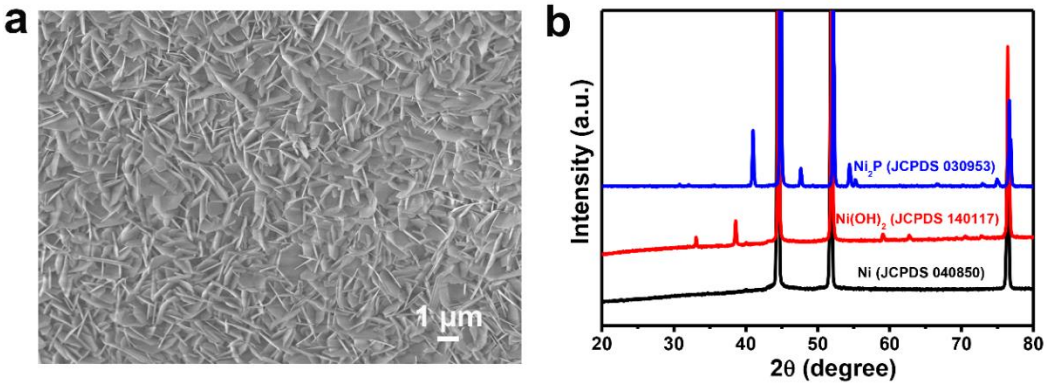

Figure 4.16 (a) SEM image of the product. (b) XRD patterns for the product using $Ni(OH)_2$ nanosheets as the precursors under the same phosphorization process (blue line), $Ni(OH)_2$ nanosheets (red line) and nickel foam substrate (black line). $Ni(OH)_2$ nanosheets were prepared via the direct hydrothermal process at 160 ºC for 24 h using a clean nickel foam and deionized water.

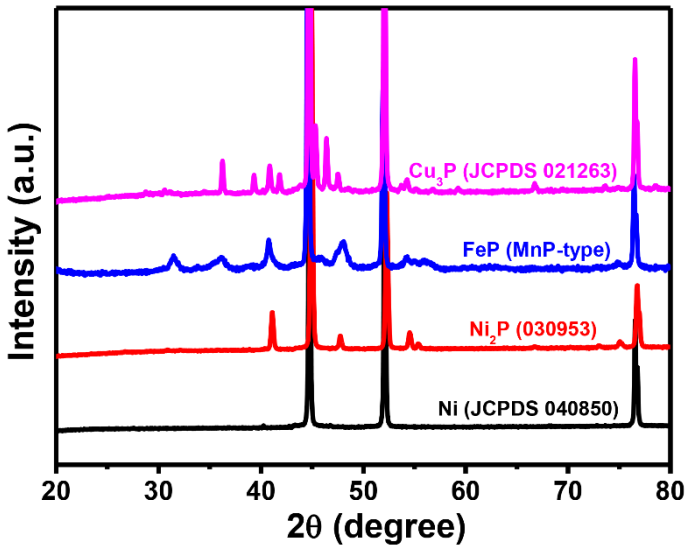

Figure 4.17 The obtained different transition metals phosphides using different transition metals precursors under the same phosphorization process. Black line is the nickel foam substrate. The Ni_2P was reused from **Figure 4.16**. Fe and Cu precursors were prepared using the similar hydrothermal method of preparing Ni-Fe LDH, except for the use of 1 mM $Fe(NO_3)_3{\cdot}9H_2O$ and 1 mM $Cu(NO_3)_2{\cdot}21/2H_2O$ instead of 0.5 mM $Ni(NO_3)_2{\cdot}6H_2O$ and 0.5 mM $Fe(NO_3)_3{\cdot}9H_2O$, respectively.

4.3.2 Structure Mechanisms

The feature of solid-liquid contact interface between catalysts and electrolyte plays an important role during the process of HER catalysis. However, little research attention has been paid to this aspect. The generated hydrogen bubbles, especially at high current densities, tend to pin or aggregate on the surface of the catalyst, resulting in decreased solid-liquid contact area and limited electron transfer. Therefore, a unique "superaerophobic" structure may be efficient to solve this challenging dilemma. **Figure 4.18a** shows that a H_2 bubble is readily pinned on the surface of the blank NF, whereas the "superaerophobic" Ni_2P/NF exhibits a tremendous potential to release the in-situ generated H_2 bubbles and prevent bubble retention.

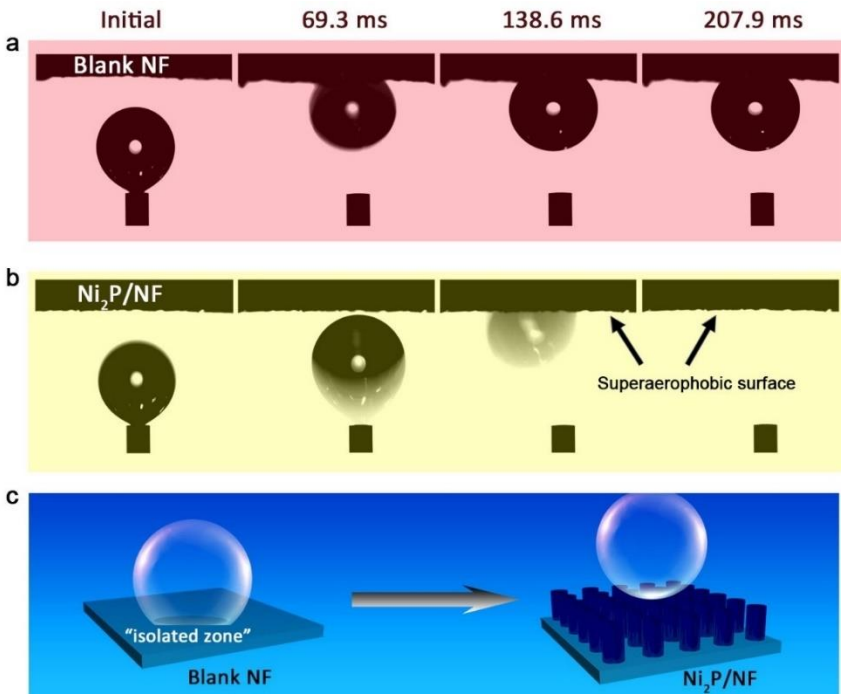

Figure 4.18. Digital images of hydrogen bubbles on (a) blank NF and (b) Ni_2P/NF. (c) Schematic illustration of the adhesion behavior for a H_2 bubble on blank NF (left) and Ni_2P/NF nanoarrays (right). The contact area is an "isolated zone" due to the bubble effect.

The contact angle tests showed that H_2 bubbles detached with a superfast speed off the surface (**Figure 4.18b**). To further analyze the "superaerophobic" property of Ni_2P/NF catalyst, a heavier gas bubble (an air bubble) was studied under the same basic conditions (1 M KOH aqueous solution), showing that air bubble also can be easily released (**Figure 4.19**). The schematic illustration reveals that the generated H_2 bubbles adhered on the surface of the blank nickel foam substrate, resulting in a deteriorated HER performance, which could be attributed to the reduced contact interface and consequent blocked electrolyte transfer (**Figure 4.18c, left**). Whereas, the "superaerophobic" structure of Ni_2P/NF releases the formed H_2 bubbles rapidly, retaining the original catalytic sites, thus the catalytic property can be maintained (**Figure 4.18c, right**). Therefore, the high-efficient electrocatalytic activity and excellent stability of the Ni_2P/NF catalyst at high current densities should be ascribed to the unique "superaerophobic" property that timely expels H_2 bubbles generated in-situ.

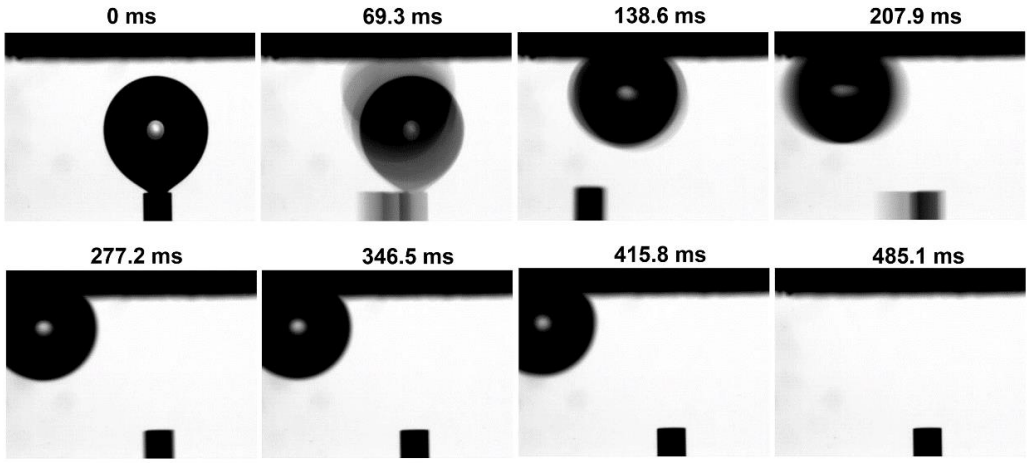

Figure 4.19. Digital images of Ni_2P/NF during air bubble adhesion process under 1 M KOH electrolyte.

4.4 Conclusions

In summary, a unique "superaerophobic" nickel phosphide nanoarray structure was successfully synthesized on a nickel foam substrate via a facile hydrothermal-then-annealing strategy. The Ni_2P/NF nanoarray structure contains the even nanowire arrays on the nickel foam and the uniform nanosheets grown onto the nanowire arrays. The as-prepared Ni_2P/NF nanoarrays exhibit a highly efficient electrocatalytic activity for hydrogen evolution under the basic electrolytes. The contact angle comparison between unique Ni_2P/NF nanoarrays and the blank NF counterpart has proved that the unique Ni_2P/NF nanoarray structure was in an interesting framework with a "superaerophobic" surface. This work offers a path to design the unique "superaerophobic" structure catalysts, enabling the industrial-scale H_2 production or other energy storage fields.

4.5 References

1. Han, N.N., et al., *Nitrogen-doped tungsten carbide nanoarray as an efficient bifunctional electrocatalyst for water splitting in acid.* Nat. Commun., 2018. **9**: p.924.

2. Faber, M.S., et al., *High-performance electrocatalysis using metallic cobalt pyrite (CoS_2) micro- and nanostructures.* J. Am. Chem. Soc., 2014. **136**(28): p. 10053-10061.

3. Lu, Z.Y., et al., *Ultrahigh hydrogen evolution performance of under-water "superaerophobic" MoS_2 nanostructured electrodes.* Adv. Mater., 2014. **26**(17): p. 2683-2687.

4. Mishra, I.K., et al., *Hierarchical CoP/Ni_5P_4/CoP microsheet arrays as a robust pH-universal electrocatalyst for efficient hydrogen generation.* Energy Environ. Sci., 2018. **11**(8): p. 2246-2252.

5. Li, B.J., M. Ai, and Z. Xu, *Mesoporous beta-Ni(OH)$_2$: synthesis and enhanced electrochemical performance.* Chem. Commun., 2010. **46**(34): p. 6267-6269.

6. Yuan, Y.F., et al., *Nickel foam-supported porous Ni(OH)$_2$/NiOOH composite film as advanced pseudocapacitor material.* Electrochim. Acta, 2011. **56**(6): p. 2627-2632.

7. Yu, X.X., et al., *Direct growth of porous crystalline $NiCo_2O_4$ nanowire arrays on a conductive electrode for high-performance electrocatalytic water oxidation.* J. Mater. Chem. A, 2014. **2**(48): p. 20823-20831.

8. Qian, M.M., et al., *Highly efficient and stable water-oxidation electrocatalysis with a very low overpotential using FeNiP substitutional-solid-solution nanoplate arrays.* Adv. Mater., 2017. **29**(46): p. 1704075.

9. Chen, P.Z., et al., *3D nitrogen-anion-decorated nickel sulfides for highly efficient overall water splitting.* Adv. Mater., 2017. **29**(30): p.1701584.

10. Wang, M.Q., et al., *Nanosized metal phosphides embedded in nitrogen-doped porous carbon nanofibers for enhanced hydrogen evolution at all pH values.* Angew. Chem. Int. Ed., 2018. **57**(7): p. 1963-1967.

Chapter 5 "Superaerophobic" Nickel Phosphide Nanoarray Catalysts for Highly Active Hydrogen Evolution at Ultrahigh Current Densities in Alkaline Solution

5.1 Introduction

Electrocatalytic water splitting ($2H_2O \rightarrow 2H_2 + O_2$) that produces hydrogen offers a promising route to provide renewable, sustainable and environment-friendly clean energy sources for the replacement of traditional fossil fuels[1-5]. However, considerable challenges still exist in the quest to boost catalytic hydrogen evolution reaction (HER) to the industrial scale. Currently, the most highly active HER reaction catalysts are scarce and costly noble metal platinum (Pt) or Pt-based materials[6-8], thus dramatically hampering the practical applications. Great efforts have been devoted to accelerating the advance of low-cost and abundant HER catalysts. Many transition metal-based electrocatalysts such as MoS_2[9], $CoSe_2$[10], transition metal phosphides[11], nitrides[12], carbides[13], oxides[14], or bimetallic materials[15] have been reported. Besides, metal-organic frameworks have also demonstrated great potential in this research area[16,17]. Owing to the low catalytic performance and the poor stability of these promising non-noble electrocatalysts when performing at large current densities, a variety of strategies has been designed to promote the reaction kinetics and improve the catalytic activities, such as improving electron transfer, designing advantageous defects[18,19], creating new active sites and tailoring the intrinsic properties[20-22]. Previous efforts have demonstrated several catalyst systems for high-current operations. These include the hybrid bimetallic phosphides (FeP/Ni_2P) for oxygen evolution reaction (OER) and HER in basic solutions[23], hexagonal α-MoB_2 for HER in acidic solutions[24], $Fe(PO_3)_2$ formed on Ni_2P/Ni foam and Ni-Fe-OH@Ni_3S_2/NF for OER in basic solutions[25,26]. Although impressive progress, there are few reports on studies of solid-liquid

interfaces and gas-liquid-solid interfaces that permit the quick release of large amount of H_2 bubbles from the electrode where generated at large current densities.

Herein, the as-prepared Ni_2P/NF nanoarray catalyst (synthesis details as shown in chapter four) was used to catalyze water reduction in alkaline solution. The Ni_2P/NF catalyst performs highly active and stable catalytic activities for HER, even exceeding the commercial noble metal Pt/C at large current densities (> 170 mA cm^{-2}). Besides, using Ni_2P||Ni-Fe LDH (LDH = layered double hydroxide) as cathode and anode electrodes, our Lab-made overall water-splitting cell also outperforms the noble metal combination made of Pt/C||Ir/C cell when the current density is higher (> 600 mA cm^{-2}). These findings open a promising approach to satisfy the requirements of scalable H_2 production at large current densities with the usage of the "superaerophobic" structure catalyst materials.

5.2 Experimental Sections

5.2.1 Materials

The as-synthesized samples (details in chapter four) were further used in the electrochemical tests.

5.2.2 Synthesis of Ni-Fe LDH

The Ni-Fe LDH was synthesized with a modified method. In a typical process, a clean nickel foam plate was put into 30 mL of a transparent light green aqueous solution containing 0.5 mM $Fe(NO_3)_2 \cdot 9H_2O$, 0.5 mM $Ni(NO_3)_2 \cdot 6H_2O$, 3 mM urea and 7.5 mM NH_4F. Then the 50 mL autoclave was transformed into an oven, kept at 120 ºC for 6 h.

After cooling down to room temperature, the obtained Ni-Fe LDH were rinsed with deionized water and dried in air for further use.

5.2.3 Characterizations

A Japan Rigaku DMax-γA X-ray diffractometer equipped with Cu Kα radiation (λ = 1.5406 Å) was used to examine the X-ray powder diffraction (XRD) patterns of the samples. The morphology was investigated via the Scanning electron microscope (SEM) using a Zeiss Supra 40 at 5 kV. Scanning transmission electron microscopy (STEM) elemental mapping images were achieved on a JEM-ARM 200F atomic resolution analytical microscope, operating at 200 kV.

5.2.4 Electrocatalytic Measurements

Electrochemical HER activities were examined via a Multipotentiostat (IM6ex, ZAHNER elektrik, Germany) in a traditional three-electrode system, with a graphite rod and a saturated calomel electrode as the counter electrode and the reference electrode, respectively. The as-prepared samples were used as the working electrodes and the electrolyte was 1 M KOH aqueous solution. During the control experiments, the homo-disperse commercial Pt/C (20 wt%) and Ir/C (20 wt%) (5 mg catalysts in 1 mL ethanol and 40 μL 5% Nafion) were loaded onto the clean nickel foam, named as Pt/C/NF and Ir/C/NF, used as the working electrodes, and the loading amount is corresponding with that of the fore-mentioned samples. Potentials described during this work without any special statement were normalized versus the reversible hydrogen electrode (RHE), according to the equation: $E_{RHE} = E_{applied} + 0.241 + 0.059 \times pH$. Where the $E_{applied}$ is the applied potential.

Electrochemical performances for overall water splitting were tested in a two-electrode system. The prepared Ni_2P/NF and Ni-Fe LDH samples were worked as cathode and anode, respectively. For comparison, noble metal catalysts Pt/C and Ir/C were also used as cathode and anode under the same conditions. The amount of produced H_2 and O_2 was collected via a commercial two-electrode water splitting setting using drainage method. The Faradic efficiency was calculated by comparing the measured and theoretical produced amounts of H_2. To simulate industrial application, the fresh prepared electrolyte was used directly without any further degassing period during the electrochemical tests.

Polarization curves were performed via sweeping the potentials at a rate of 10 mV s^{-1}. The corresponding Tafel plots were obtained by fitting the linear portion between the overpotential (η) and log current (log j), using the equation: η = b log (j) + a, where b is the Tafel slope. Electrochemical impedance spectroscopy (EIS) test were acquired ranging from 100 kHz to 0.1 Hz at the amplitude of 5 mV. Double-layer capacitance (C_{dl}) data were collected via the cyclic voltammetry (CV) curves measured, the potentials were between 0.067 V and 0.167 V and the scanning rates were from 20 mV s^{-1} to100 mV s^{-1}. The stability performances were examined through various electrochemical measurements including accelerated cycling polarization curves with a rate of 100 mV s^{-1}, multi-potential steps tests, multi-current steps tests, current density versus time curves at a constant potential and potential versus time curves at a constant current density. All the measured potentials were calibrated with iR compensation if not explicitly specified, where R is the solution resistance.

5.2.5 H_2 Amount Measurements

H_2 amount for Ni_2P||Ni-Fe LDH was tested via a Hoffman apparatus setup in a two-electrode system at room temperature. The electrolyte was 1 M KOH aqueous solution. In order to detect the H_2 amount more accurately, methyl orange was added into the electrolyte (0.1 mg/mL) to observe a more obvious color.

5.3 Results and Discussions

5.3.1 Electrocatalytic HER Activities

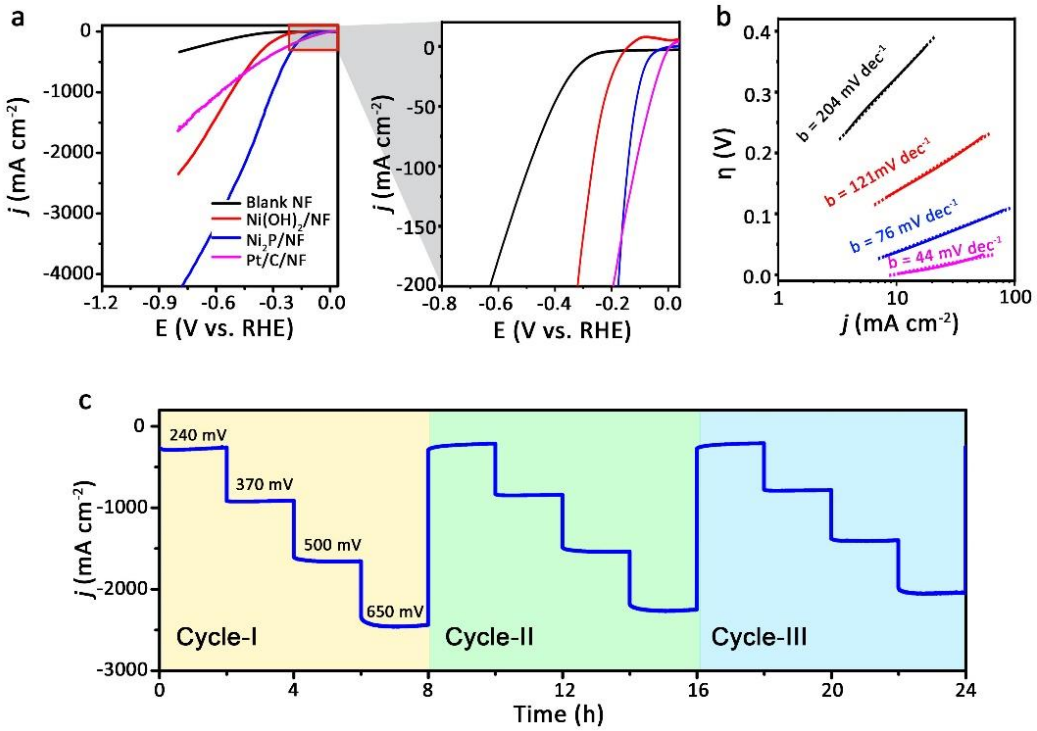

Figure 5.1 (a) HER polarization curves for different catalysts at high current density (left) and low current density (right). Scan rate: 10 mV s^{-1}. (b)Tafel plots for different catalysts derived from Figure 2a (right). (c) Multi-chronoamperometric responses curve from 240 mV to 650 mV overpotentials for the Ni_2P/NF catalyst.

Electrocatalytic HER activities of the as-prepared catalysts were evaluated via a three-electrode system in 1 M KOH electrolyte at room temperature, using a graphite rod and a saturated calomel electrode as the counter electrode and the reference electrode, respectively. The polarization curves for the Ni_2P/NF, $Ni(OH)_2$/NF, blank NF and Pt/C/NF catalysts were operated at the scan rate of 10 mA cm^{-2}, as demonstrated in **Figure 5.1a (left)**. The results show that the Ni_2P/NF catalyst exhibits an inferior catalytic property at the low current densities compared with the noble metal catalysts Pt/C/NF. However, this phenomenon has totally been changed when the current densities are higher. The prepared Ni_2P/NF catalyst displays an excellent electrocatalytic activity, which ever shows a better catalytic performance than the commercial Pt/C (20 wt%) catalyst at high current densities. For example, the Ni_2P/NF can sustain current densities of 1000 mA cm^{-2} and 1500 mA cm^{-2} at overpotentials of 306 mV and 368 mV, respectively. While, under the same conditions, much higher overpotentials of 575 mV and 758 mV are required to reach at the current densities of 1000 mA cm^{-2} and 1500 mA cm^{-2} for the commercial Pt/C/NF catalyst. Another interesting phenomenon is that the electrocatalytic activity of Ni_2P/NF catalyst always overwhelmingly surpassed that of $Ni(OH)_2$/NF and blank NF under the constant overpotentials, which could be attributed to the high active intrinsic catalytic property of the nickel phosphide. To show more details, the polarization curves for the obtained samples under the low current densities (< 200 mA cm^{-2}) were given in **Figure 5.1a (right)**, the intersection dot for Ni_2P/NF and Pt/C/NF appeared at the current density of ~ 160 mA cm^{-2}. To assess the reaction kinetics, Tafel analysis was performed from the low-current-density polarization curve area shown in **Figure 5.1a (right)**. The corresponding Tafel plots give the Tafel slope values of 76, 44, 121 and 204 mV dec^{-1} for Ni_2P/NF, Pt/C, $Ni(OH)_2$/NF and blank NF, respectively (**Figure 5.1b**). Although, the Tafel slope of

Ni_2P/NF is larger than that of Pt/C/NF, which is also much smaller that of $Ni(OH)_2$/NF and blank NF. The lower Tafel slope value of Ni_2P/NF suggests its superior HER catalytic kinetics.[27]

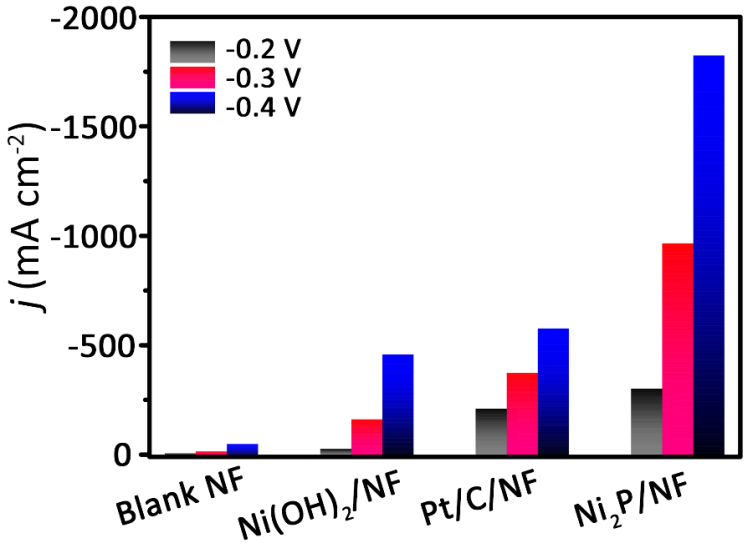

Figure 5.2 Comparison of HER performance for the various catalysts under the constant potentials.

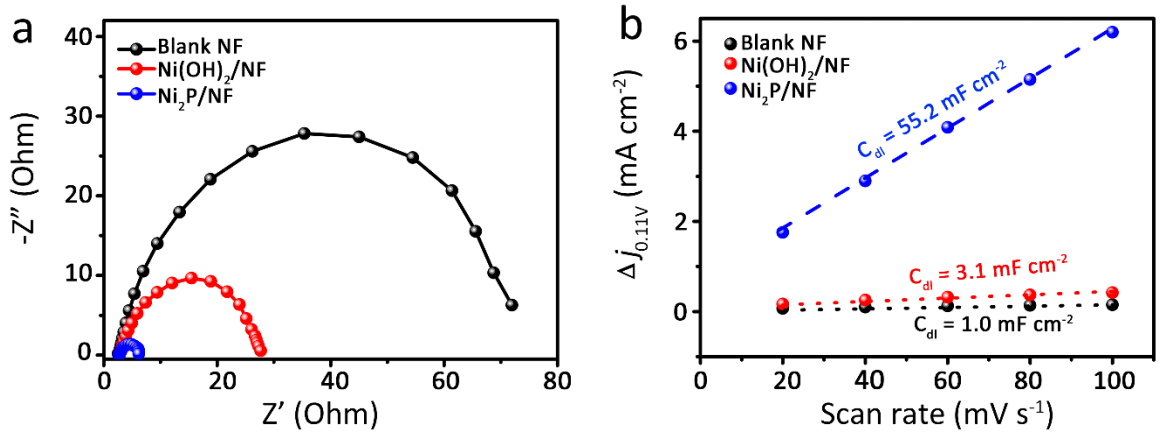

Figure 5.3 (a, b) EIS Nyquist and C_{dl} plots of the various catalysts. Z′ and Z″ are the real and the imaginary impedance, respectively.

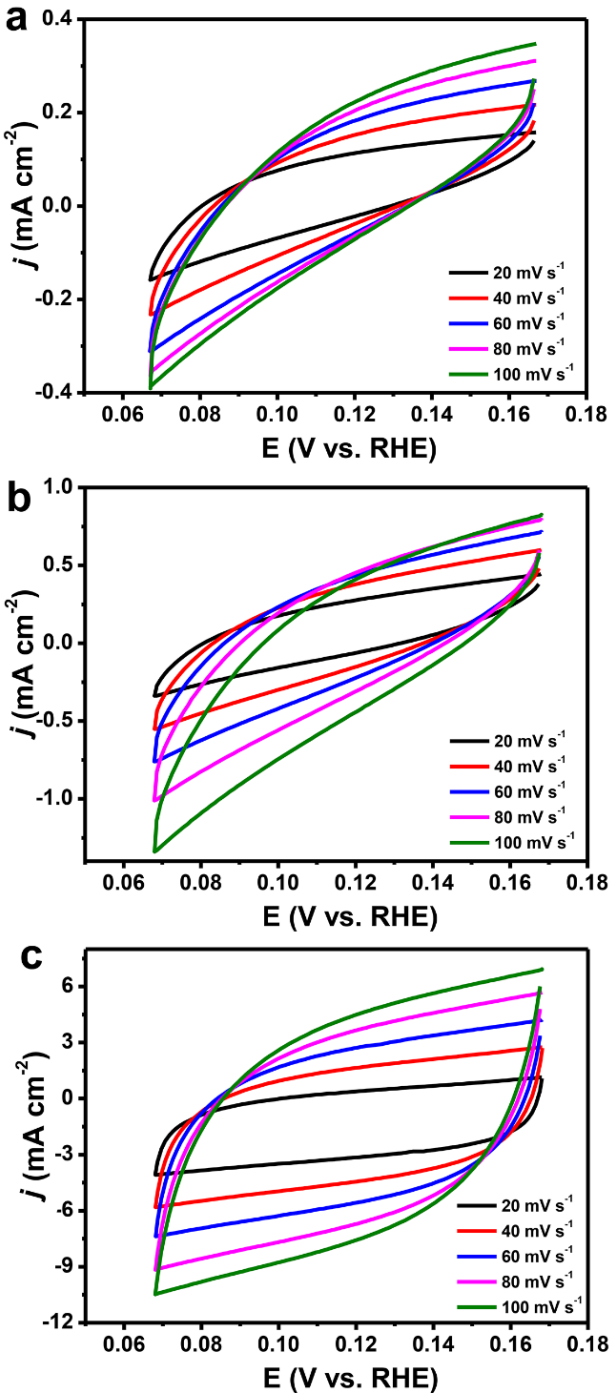

Figure 5.4 Cyclic voltammetry curves of (a) Blank NF, (b) $Ni(OH)_2$/NF and (c) Ni_2P/NF catalysts under the potential of 0.07~0.17 V vs. RHE at different scan rates from 20 mV s^{-1} to 100 mV s^{-1}.

The HER activities for the various catalysts at different constant overpotentials were also recorded, as shown in **Figure 5.2**. With the increase of the overpotentials, the catalysis advantage of Ni_2P/NF becomes more and more obvious. For example, the Ni_2P/NF catalyst demonstrates a superior electrochemical performance with a current density > 1800 mA cm^{-2} at an overpotential of 0.4 V while the Pt/C/NF reaches at a much lower current density of only ~ 580 mA cm^{-2}. EIS Nyquist plots reveal that the charge transfer resistance (R_{ct}) of Ni_2P/NF is 3.5 Ω, which is much lower than that of $Ni(OH)_2$/NF (25.2 Ω) and blank NF (69.5 Ω) at an overpotential of 100 mV, indicating accelerated charge transfer kinetics for Ni_2P/NF catalyst (**Figure 5.3a**). To estimate the effective electrochemically active surface area of the catalysts, we calculated double-layer capacitances (C_{dl}). The C_{dl} of Ni_2P/NF (55.2 mF cm^{-2}) is larger than $Ni(OH)_2$/NF (3.1 mF cm^{-2}) and blank NF (1.0 mF cm^{-2}) (**Figure 5.3b** and **Figure 5.4**), suggesting more exposed active sites on Ni_2P/NF catalyst.

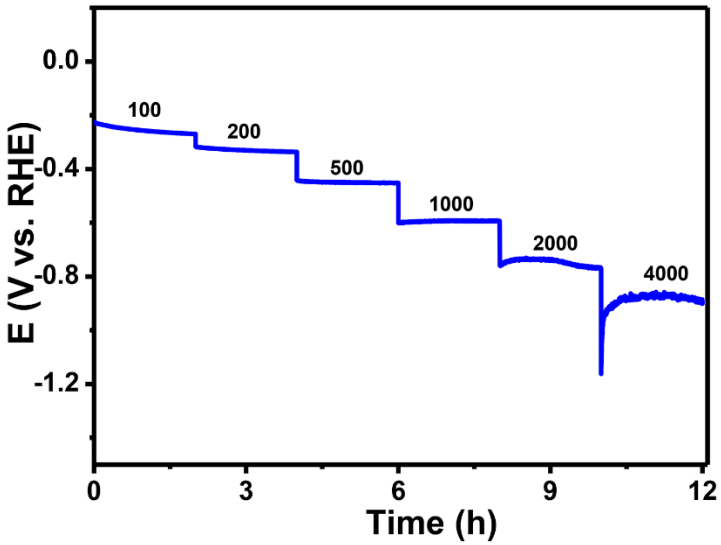

Figure 5.5 Multi-steps chronopotentiometry curve at different current densities from 100 to 4000 mA cm^{-2}.

Besides the above-mentioned electrocatalytic activities, stability property is also a critical parameter to examine the catalysts' performance, which is necessary to realize the large-scale hydrogen production. We evaluated the HER stability of Ni_2P/NF catalyst via multiple testing methods. Multi-step chronoamperometric curves were measured under a wide potential range (from 240 to 650 mV), the long-term test includes three cycles, every cycle is 8 h including four different electrolysis processes at four different overpotentials made of 240 mV, 370 mV, 500 mV and 650 mV, as shown in **Figure 5.1c**. The multi-step chronopotentiometry curves were also recorded across a long-term test of 12 h which was operated under a broad current density (from 100, 200, 500, 1000, 2000 to 4000 mA cm^{-2}), as shown in **Figure 5.5**. These above results show that the electrocatalytic activities of the prepared Ni_2P/NF remain stable after every step of the long-term tests, confirming the excellent stability of Ni_2P/NF catalyst.

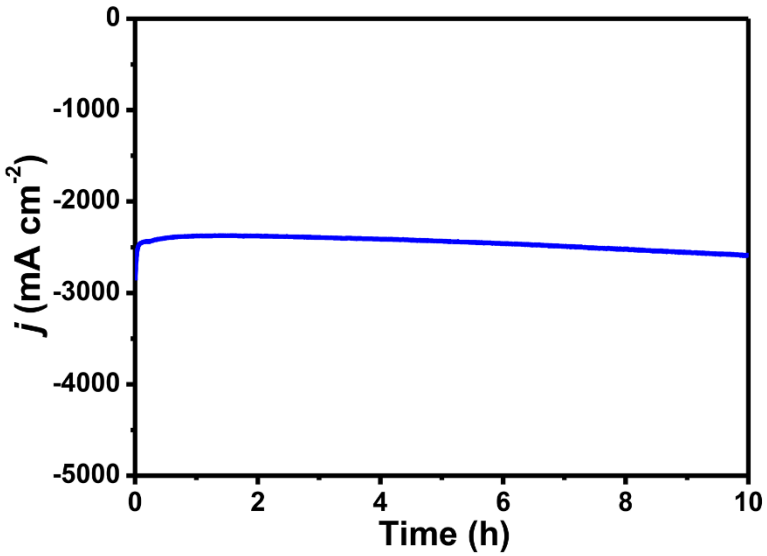

Figure 5.6 Long-time chronoamperometry (*j*–t) curve at a high current density of 2500 mA cm^{-2} at the potential of 0.7 V.

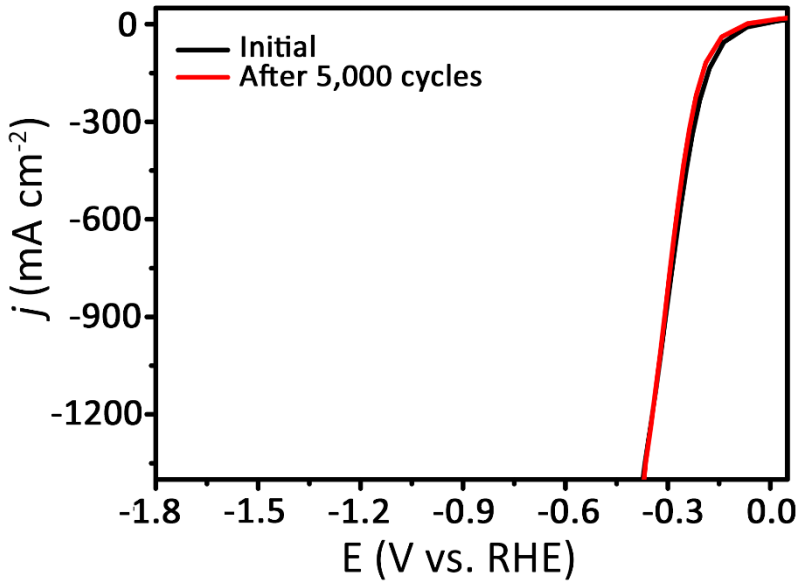

Figure 5.7 Cyclic polarization curves for Ni_2P/NF before and after 5,000 cycles.

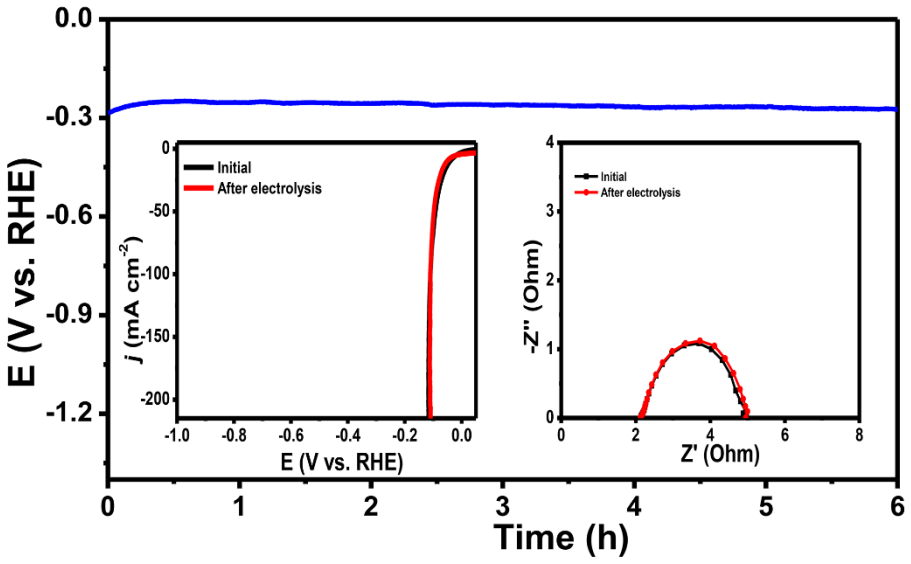

Figure 5.8 Chronopotentiometry curve of Ni_2P/NF at the current density of 500 mA cm^{-2}, the insets are polarization curves of Ni_2P/NF (left) at a scan rate of 10 mV s^{-1} and EIS Nyquist plots at the overpotential of 0.1 V before and after the electrolysis (right).

To further investigate the stability of the Ni_2P/NF catalyst, more various measurements have been applied. Firstly, we chose a relatively high current density to operate. The long-term chronoamperometry (*j*–t) test shows that at a high current density of ~ 2500 mA cm^{-2}, the current density for Ni_2P/NF catalyst can be maintained without obvious decrease even after 10 h long-term continuous electrolysis, as demonstrated in **Figure 5.6**. This result exhibits that the Ni_2P/NF catalyst still possesses a great stability even used at a high current density. Additionally, the accelerated cyclic polarization curves for Ni_2P/NF catalyst were tested during the potential range from 0 V to -0.37 V. Meanwhile, the current densities were ranging from 0 mA cm^{-2} to more than 1350 mA cm^{-2}. After 5,000 cycles, the long-term test result still demonstrates no apparent activity decay, as shown in **Figure 5.7**. Besides, the stability of Ni_2P/NF catalyst was also checked under a mild current density. Chronopotentiometry curve of Ni_2P/NF was examined at the constant current density of 500 mA cm^{-2}, the corresponding potential demonstrates no apparent increment even after 6 h's test. Furthermore, it should be noted that no visible shifts were observed in polarization curves or EIS Nyquist plots after the long-term chronopotentiometry test at the constant current density of 500 mA cm^{-2}, as shown **Figure 5.8.** The above measurement results clearly indicate the good stability of Ni_2P/NF catalyst under both the mild and high current electrolysis (**Figure 5.8**). The morphology and crystal structure of the Ni_2P/NF after electrolysis were investigated via SEM and XRD. The postmortem SEM and XRD characterizations reveal no apparent changes of the morphology and crystal structure after a long-term high-current electrolysis (**Figure 5.9**). The above kinetic and energetic merits demonstrate that the Ni_2P/NF is a superior catalyst among the previously reported HER catalysts under basic conditions (**Figure 5.10** and **Table 5.1**)[28-37].

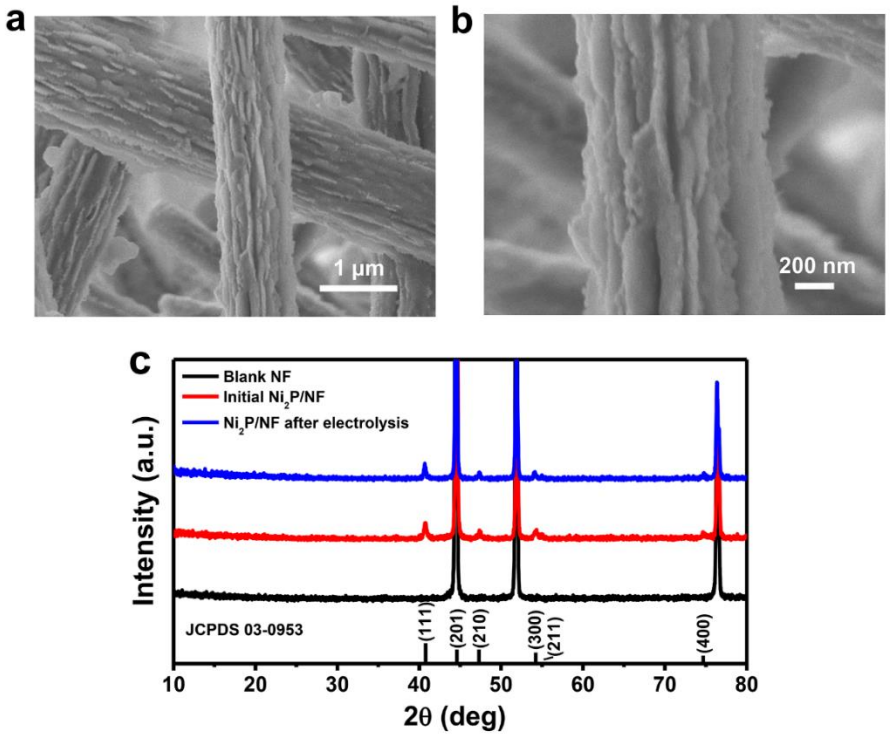

Figure 5.9 (a, b) SEM images of Ni_2P/NF after the electrolysis. (c) Comparison of XRD patterns for Ni_2P/NF before and after the electrolysis.

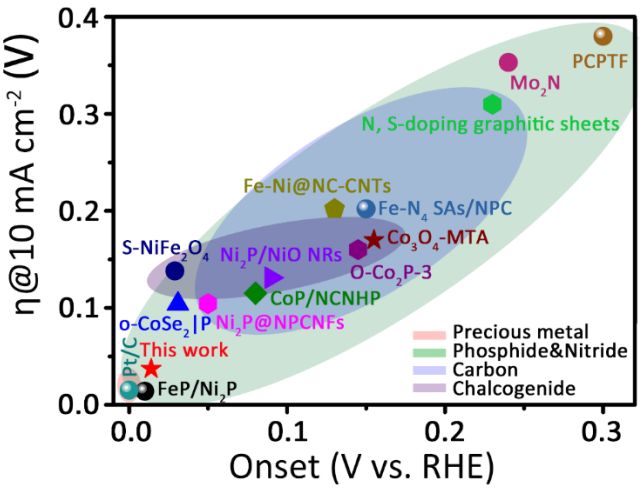

Figure 5.10 Comparison of the electrocatalytic HER performance of Ni_2P/NF with the other reported high-efficiency catalysts.

Table 5.1 Comparison of HER performance of the prepared Ni_2P/NF with other recently reported high-efficiency electrocatalysts.

Catalysts	Electrolytes	η_{10} (mV)	Onset (V vs. RHE)	References
Ni_2P	1.0 M KOH	37	0.014	This work
Pt/C	1.0 M KOH	15	0	
FeP/Ni_2P	1.0 M KOH	14	~0.010	23
o-$CoSe_2$|P	1.0 M KOH	104	0.031	10
O-Co_2P-3	1.0 M KOH	160	~0.145	35
Fe-N_4 SAs/NPC	1.0 M KOH	202	~0.15	42
Fe-Ni@NC-CNTs	1.0 M KOH	202	~0.13	37
PCPTF	1.0 M KOH	380	~0.3	36
S-$NiFe_2O_4$	1.0 M KOH	138	0.029	30
Co_3O_4-MTA	1.0 M KOH	~170	~0.155	43
CoP/NCNHP	1.0 M KOH	115	~0.08	32
Ni_2P@NPCNFs	1.0 M KOH	104.2	~0.05	33
Ni_2P/NiO NRs	1.0 M KOH	131	~0.09	34
N, S-doping graphitic sheets	1.0 M KOH	230	0.31	29
Mo_2N	1.0 M KOH	240	0.353	31

5.3.2 Overall Water Splitting Using Ni_2P||Ni-Fe LDH Catalysts

To demonstrate the advantages of the Ni_2P/NF catalyst for large-scale H_2 production, we conducted overall water splitting in a two-electrode system using 1 M KOH aqueous solution as the electrolyte. The Ni-Fe layered double hydroxide (LDH) grown on nickel foam (Ni-Fe LDH/NF) was synthesized during a hydrothermal reaction, the reaction aqueous solution containing 0.5 mM $Fe(NO_3)_2{\cdot}9H_2O$, 0.5 mM $Ni(NO_3)_2{\cdot}6H_2O$, 3mM urea and 7.5 mM NH_4F. The reaction temperature was chosen to be 120 °C and reaction time is 6 h. We chose the Ni-Fe LDH as the anode electrode because the Ni-Fe LDH is one of the

most active catalysts for oxygen evolution reaction (OER). The Ni_2P/NF catalyst was used

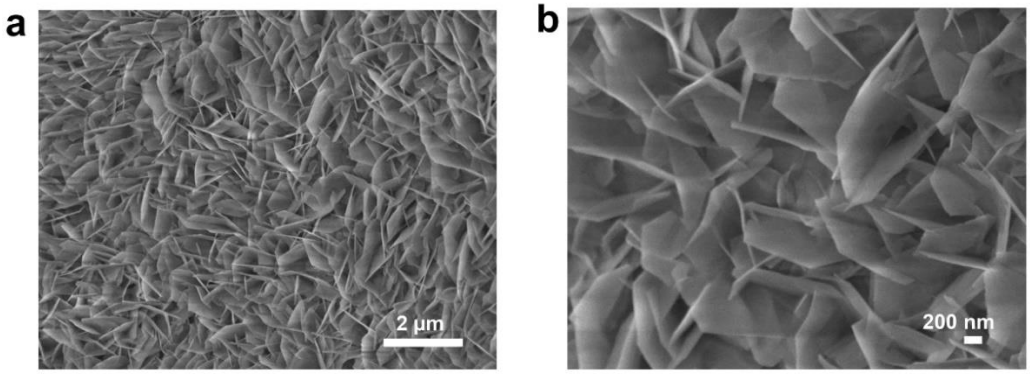

Figure 5.11 (a, b) SEM images of the Ni-Fe LDH/NF obtained at 120 ºC for 6 h via a hydrothermal method.

directly as the cathode electrode. The SEM images of Ni-Fe LDH/NF catalyst show that the nanosheets of Ni-Fe LDH are uniformly distributed on the nickel foam substrate, as shown in **Figure 5.11**. XRD patterns in **Figure 5.12** show the the Ni-Fe LDH catalyst has the pure phase structure. The polarization curves EIS Nyquist plots of Ni-Fe LDH and commercial Ir/C (20 wt%) demonstrates that the Ni-Fe LDH catalyst has an outstanding OER property which was even better than the noble metal Ir/C (**Figure 5.13**). The electrolysis cell system using Ni-Fe LDH/NF as the anode and Ni_2P/NF as the cathode, is denoted as Ni_2P||Ni-Fe LDH[38]. For comparison, we also deposited the same amount of the commercial noble metal catalysts Ir/C (20 wt%) and Pt/C (20 wt%) onto nickel foam substrate and used them as anode and cathode, respectively. The two-electrode noble metal combination cell is denoted as Pt/C||Ir/C. The electrochemical activities of Ni_2P||Ni-Fe LDH and Pt/C||Ir/C were examined under the same conditions using 1 M KOH as the electrolyte. Polarization curves of Ni_2P||Ni-Fe LDH and Pt/C||Ir/C were shown in **Figure 5.14a**, revealing that Ni_2P||Ni-Fe

LDH exhibits an inferior performance compared to Pt/C||Ir/C under the low current

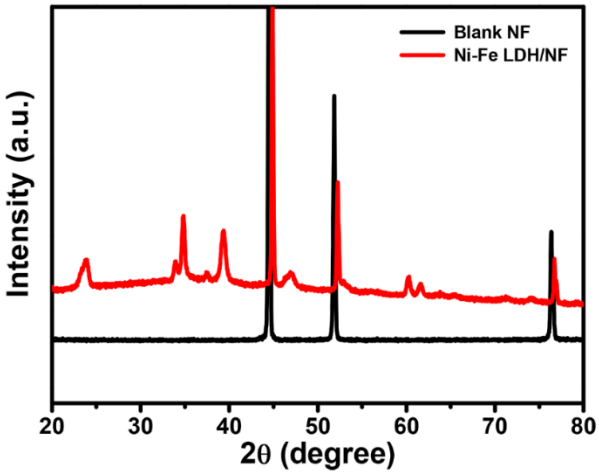

Figure 5.12 XRD pattern of the Ni-Fe LDH/NF obtained at 120 ºC for 6 h via a hydrothermal method.

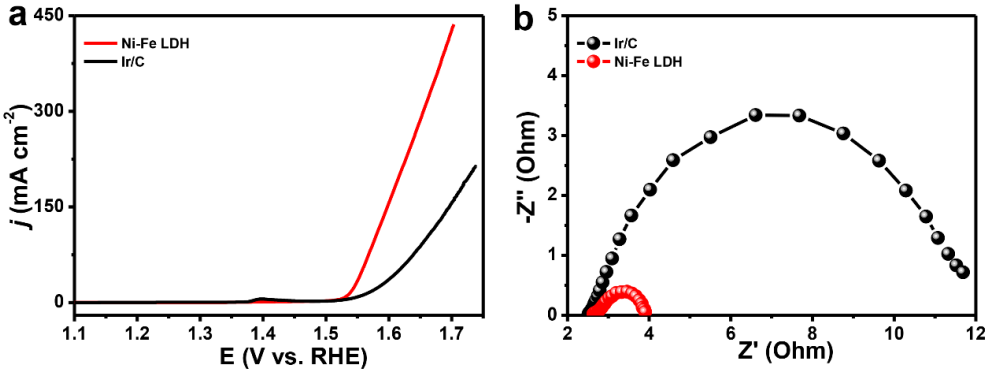

Figure 5.13 Electrocatalytic OER performances of the obtained Ni-Fe LDH/NF and the commercial Ir/C. (a) Polarization curves with a scan rate of 10 mV s^{-1} and (b) EIS Nyquist plots at the overpotential of 0.34 V.

densities (< 600 mA cm^{-2}). The onset voltage of noble metals combination Pt/C||Ir/C is 1.52 V, which was also lower than that of Ni_2P||Ni-Fe LDH (1.58 V). The EIS Nyquist plots which were collected at a voltage of 1.7 V show that the R_{ct} of Pt/C||Ir/C is 11.4 Ω, lower

than that of Ni_2P||Ni-Fe LDH (15.5 Ω). This result further proves the inferior catalytic

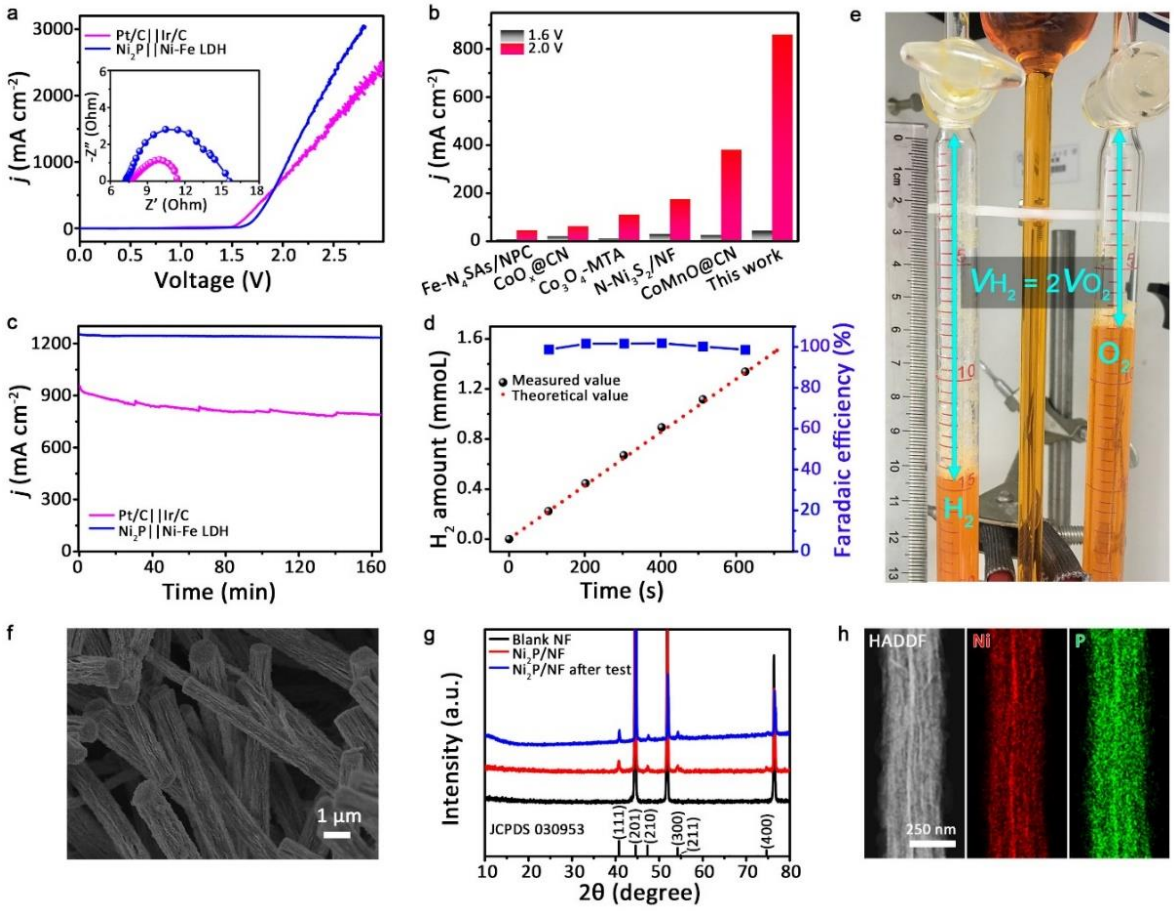

Figure 5.14 (a) Polarization curves of the catalysts at a scan rate of 10 mV s^{-1}. Inset shows EIS Nyquist plots of the catalysts at a voltage of 1.7 V. (b) The comparison of overall electrocatalytic water splitting performance of the Ni_2P||Ni-Fe LDH catalyst with recently reported highly active catalysts. (c) Chronoamperometric curves at a voltage of 2.1 V. (d and e) H_2 amount for Ni_2P||Ni-Fe LDH at a fixed current density of 1000 mA cm^{-2} and optical picture of the measured setup Hoffman apparatus. (f-h) SEM, XRD and STEM elemental mapping images of Ni_2P/NF after the long-term electrolysis.

property phenomenon for Ni_2P||Ni-Fe LDH under low current densities (Inset in **Figure 5.14a**). However, the growth rate of current densities for Ni_2P||Ni-Fe LDH is much faster

than that for Pt/C||Ir/C at the same voltage intervals. Thus, the electrochemical activity of

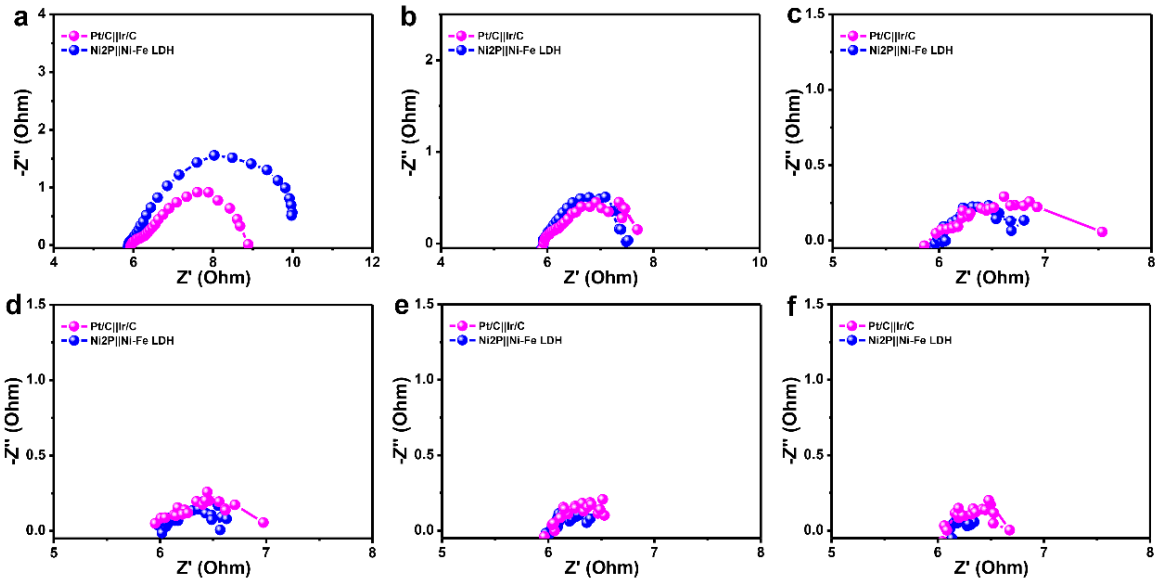

Figure 5.15 EIS Nyquist plots for Ni2P||Ni-Fe LDH and Pt/C||Ir/C catalysts at different voltages. (a) 1.72 V, (b) 1.75 V, (c) 1.87 V, (d) 1.97 V, (e) 2.06 V and (f) 2.2 V. The results show that the EIS of Ni_2P||NiFe LDH catalyst is large than EIS of Pt/C||Ir/C at a low voltage. However, the EIS results of Ni_2P||NiFe LDH decrease more rapidly than that of the Pt/C||Ir/C catalyst with the increased voltages, and even smaller than that of Pt/C||Ir/C at a high voltage >1.87 V.

Ni_2P||Ni-Fe LDH rapidly surpasses that of Pt/C||Ir/C when the current densities were higher (> 600 mA cm^{-2}). Besides, a series of EIS Nyquist plots collected at different voltages show that the R_{ct} values of Ni_2P||NiFe LDH decrease more quickly than that of the Pt/C||Ir/C with the increase of the voltages, and would become lower than that of Pt/C||Ir/C at a high voltage >1.87 V (**Figure 5.15**). These results exhibit that Ni_2P||NiFe LDH shows superior catalytic activities at high current densities or high voltages. The observations can be ascribed to the unique "superaerophobic" characteristics of Ni_2P nanoarrays. The unique "superaerophobic" feature help the Ni_2P||Ni-Fe LDH release the numerous generated hydrogen bubbles at high current densities to avoid the reduced contact interface with the

electrolyte. By contrast, the polarization curve of Pt/C||Ir/C cell at high current densities becomes choppy due to the strong "bubble effect", thus reducing its catalytic properties.

Table 5.2 Comparison of the electrocatalytic overall water splitting activities of the prepared Ni_2P/NF with other recently reported high-efficiency electrocatalysts.

Catalysts	Electrolytes	$j_{1.6V}$ (mA cm^{-2})	$j_{2.0V}$ (mA cm^{-2})	References
Ni_2P/NF	1.0 M KOH	43	860	**This work**
Fe-N_4 SAs/NPC	1.0 M KOH	~7	44	42
Co_3O_4-MTA	1.0 M KOH	10	110	43
CoO_x@CN	1.0 M KOH	20	62	40
N-Ni_3S_2/NF	1.0 M KOH	30	175	39
CoMnO@CN	1.0 M KOH	25	380	41

The superior overall water splitting performances of Ni_2P||Ni-Fe LDH cell at high current densities could not be separated from the special "superaerophobic" structure, thus the phenomenon would be more obvious at higher voltages where the more gas bubbles were produced. The electrochemical activities of our Ni_2P||Ni-Fe LDH compared with other reported catalysts demonstrate that Ni_2P||Ni-Fe LDH exhibit a much better catalytic performance at the higher voltage of 2.0 V rather than the lower voltage of 1.6 V (**Figure 5.14b** and **Table 5.2**)[39-43]. We measured the long-term chronoamperometry for Ni_2P||Ni-Fe LDH and Pt/C||Ir/C cells operated at a constant voltage of 2.1 V to check their stabilities. The Ni_2P||Ni-Fe LDH cell shows an excellent stability without decay of the current density during the continuous electrolysis of more than 160 minutes, However, the Pt/C||Ir/C cell exhibits an inferior stable property (**Figure 5.14c** and **Figure 5.16**). To simulate the hydrogen industrialization production, we collected the generated H_2 from the Ni_2P||Ni-Fe

LDH catalyst-driving cell via a Hoffman apparatus setup (**Figure 5.17**). The amounts of H_2

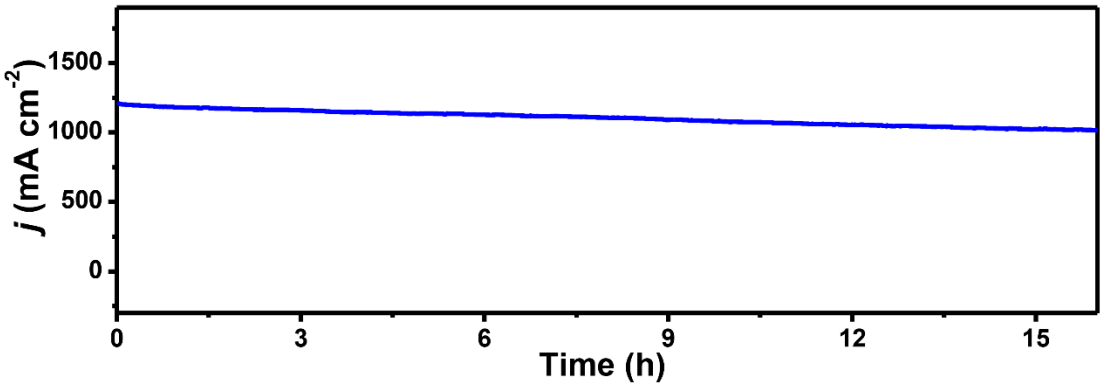

Figure 5.16 Long-time chronoamperometric curves for Ni_2P||Ni-Fe LDH at the constant voltage of 2.1 V.

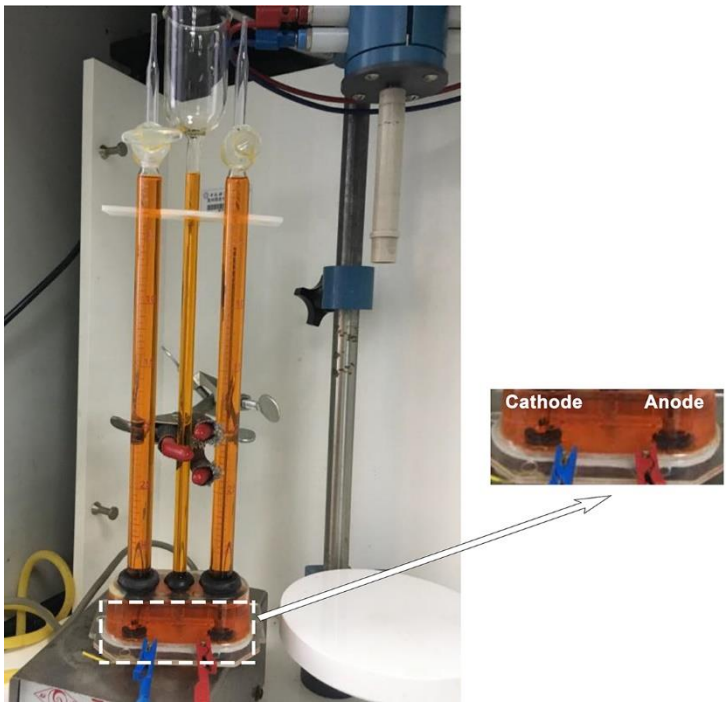

Figure 5.17 The digital photo of Hoffman apparatus.

produced were collected at the current density of 1000 mA cm^{-2} or 500 mA cm^{-2}, the produced H_2 amounts match well with the theoretically calculated values, corresponding to

a Faradaic efficiency of ~100% (**Figure 5.14d** and **Figure 5.18**). As shown in **Figure 5.14e**, the volume of the produced H_2 is about 15 milliliter and volume of the generated O_2 is about 7.5 milliliter. The volumetric ratio of the measured H_2 and O_2 is about 2 : 1, which is corresponding with the theoretical value of 2 : 1. To investigate the stability of the Ni_2P/NF catalyst after the long-term electrolysis during two-electrode system. Postmortem SEM images for Ni_2P/NF catalyst show that no obvious morphology changes appear after the long-term high-current overall water splitting electrolysis (**Figure 5.14f** and **Figure 5.19**). Besides, XRD patterns and STEM elemental mapping image characterizations for Ni_2P/NF catalyst further demonstrate that there were no obvious changes of the structural phase and the existence of elemental distribution after high-current electrolysis during overall water splitting cell system, confirming the chemical and structural stability of the Ni_2P/NF catalyst (**Figure 5.14g** and **Figure 5.14h**).

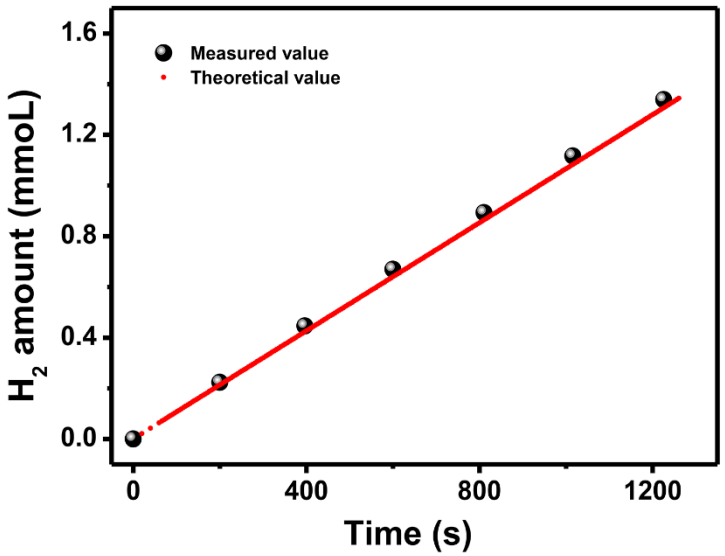

Figure 5.18 H_2 amount produced during the overall water splitting at a fixed current density of 500 mA cm^{-2}, measured in a Hoffman apparatus under 1 M KOH electrolyte.

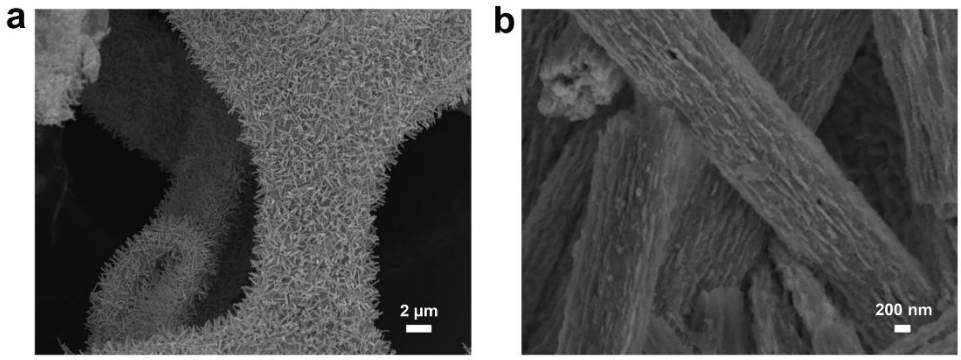

Figure 5.19 (a and b) SEM images of Ni_2P/NF after the long-time electrolysis during overall water splitting.

5.4 Summary

In this chapter, electrochemical performance of the unique "superaerophobic" nickel phosphide nanoarray structure was investigated. The Ni_2P/NF catalyst exhibits an exceptionally high electrocatalytic activity and stability for hydrogen evolution under high current densities and basic electrolytes. A two-electrode Lab-scale electrolyser composed of a Ni-Fe LDH anode and a Ni_2P/NF cathode also demonstrated an excellent catalytic capability for overall water splitting, which surpassed the performance of the Pt/C||Ir/C cell at a higher current density (> 600 mA cm^{-2}). This work uncovers the potential of the low-cost nickel phosphide nanoarrays as HER catalysts for H_2 production at ultra-large current densities owing to the unique "superaerophobic" structure.

5.5 References

1. Gonzalez-Flores, D., et al., *Heterogeneous water oxidation: Surface activity versus amorphization activation in cobalt phosphate catalysts.* Angew. Chem. Int. Ed., 2015. **54**(8): p. 2472-2476.

2. Ling, T., et al., *Activating cobalt(II) oxide nanorods for efficient electrocatalysis by strain engineering.* Nat. Commun., 2017. **8**: p. 1509.

3. Nai, J.W., et al., *Formation of Ni-Fe mixed diselenide nanocages as a superior oxygen evolution electrocatalyst.* Adv. Mater., 2017. **29**(41): p. 1703870.

4. Wang, D.Y., et al., *Highly active and stable hybrid catalyst of cobalt-doped FeS_2 nanosheets-carbon nanotubes for hydrogen evolution reaction.* J. Am. Chem. Soc., 2015. **137**(4): p. 1587-1592.

5. Zhang, B., et al., *Homogeneously dispersed multimetal oxygen-evolving catalysts.* Science, 2016. **352**(6283): p. 333-337.

6. Chen, G.B., et al., *Accelerated hydrogen evolution kinetics on NiFe-layered double hydroxide electrocatalysts by tailoring water dissociation active sites.* Adv. Mater., 2018. **30**(10): p. 1706279.

7. Masa, J., et al., *Ultrathin high surface area nickel boride (Ni_xB) nanosheets as highly efficient electrocatalyst for oxygen evolution.* Adv. Energy Mater., 2017. **7**(17): p. 1700381.

8. Yin, J., et al., *Oxygen vacancies dominated NiS_2/CoS_2 interface porous nanowires for portable Zn-Air batteries driven watersplitting devices.* Adv. Mater., 2017. **29**(47): p. 1704681.

9. Chang, K., et al., *Targeted synthesis of 2H-and 1T-phase MoS_2 monolayers for catalytic hydrogen evolution.* Adv. Mater., 2016. **28**(45): p. 10033-10041.

10. Zheng, Y.R., et al., *Doping-induced structural phase transition in cobalt diselenide enables enhanced hydrogen evolution catalysis.* Nat. Commun., 2018. **9**: p. 2533.

11. Jiang, N., et al., *Electrodeposited cobalt-phosphorous-derived films as competent bifunctional catalysts for overall water splitting.* Angew. Chem. Int. Ed., 2015. **54**(21): p. 6251-6254.

12. Xie, L.S., et al., *In situ formation of a 3D core/shell structured Ni_3N@Ni-Bi nanosheet array: an efficient non-noble-metal bifunctional electrocatalyst toward*

full water splitting under near-neutral conditions. J. Mater. Chem. A, 2017. **5**(17): p. 7806-7810.

13. Huang, Y., et al., *Mo_2C nanoparticles dispersed on hierarchical carbon microflowers for efficient electrocatalytic hydrogen evolution.* Acs Nano, 2016. **10**(12): p. 11337-11343.

14. Yu, Z.Y., et al., *Ni-Mo-O nanorod-derived composite catalysts for efficient alkaline water-to-hydrogen conversion via urea electrolysis.* Energy Environ. Sci., 2018. **11**(7): p. 1890-1897.

15. Duan, J.J., S. Chen, and C. Zhao, *Ultrathin metal-organic framework array for efficient electrocatalytic water splitting.* Nat. Commun., 2017. **8**: p. 15341.

16. Wang, H., et al., *Metal-organic frameworks for energy applications.* Chem, 2017. **2**(1): p. 52-80.

17. Zhu, B.J., R.Q. Zou, and Q. Xu, *Metal-organic framework based catalysts for hydrogen evolution.* Adv. Energy Mater., 2018. **8**(24): p. 1801193.

18. Jia, Y., J. Chen, and X.D. Yao, *Defect electrocatalytic mechanism: concept, topological structure and perspective.* Mater. Chem. Front., 2018. **2**(7): p. 1250-1268.

19. Jia, Y., et al., *The role of defect sites in nanomaterials for electrocatalytic energy conversion.* Chem, 2019, **5**: p. 1371-1397.

20. Ledendecker, M., et al., *The synthesis of nanostructured Ni_5P_4 films and their use as a non-noble bifunctional electrocatalyst for full water splitting.* Angew. Chem. Int. Ed., 2015. **54**(42): p. 12361-12365.

21. Liang, H.F., et al., *Porous two-dimensional nanosheets converted from layered double hydroxides and their applications in electrocatalytic water splitting.* Chem. Mater., 2015. **27**(16): p. 5702-5711.

22. Xiong, Q.Z., et al., *Cobalt covalent doping in MoS_2 to induce bifunctionality of overall water splitting.* Adv. Mater., 2018. **30**(29): p. 1801450.

23. Yu, F., et al., *High-performance bifunctional porous non-noble metal phosphide catalyst for overall water splitting.* Nat. Commun., 2018. **9**: p. 2551.

24. Chen, Y.L., et al., *Highly active, nonprecious electrocatalyst comprising borophene subunits for the hydrogen evolution reaction.* J. Am. Chem. Soc., 2017. **139**(36): p. 12370-12373.

25. Zhou, H.Q., et al., *Highly active catalyst derived from a 3D foam of $Fe(PO_3)_2/Ni_2P$ for extremely efficient water oxidation.* P. Natl. Acad. Sci. USA, 2017. **114**(22): p. 5607-5611.

26. Zou, X., et al., *Ultrafast formation of amorphous bimetallic hydroxide films on 3D conductive sulfide nanoarrays for large-current-density oxygen evolution electrocatalysis.* Adv. Mater., 2017. **29**(22): p. 1700404.

27. Shinagawa, T., A.T. Garcia-Esparza, and K. Takanabe, *Insight on Tafel slopes from a microkinetic analysis of aqueous electrocatalysis for energy conversion.* Sci. Rep., 2015. **5**: p. 13801.

28. You, B., et al., *Universal molecular-confined synthesis of interconnected porous metal oxides-NC frameworks for electrocatalytic water splitting.* Nano Energy, 2018. **48**: p. 600-606.

29. Hu, C.G. and L.M. Dai, *Multifunctional carbon-based metal-free electrocatalysts for simultaneous oxygen reduction, oxygen evolution, and hydrogen evolution.* Adv. Mater., 2017. **29**(9): p. 1604942.

30. Liu, J.L., et al., *S-$NiFe_2O_4$ ultra-small nanoparticle built nanosheets for efficient water splitting in alkaline and neutral pH.* Nano Energy, 2017. **40**: p. 264-273.

31. Ma, L., et al., *Efficient hydrogen evolution reaction catalyzed by molybdenum carbide and molybdenum nitride nanocatalysts synthesized via the urea glass route.* J. Mater. Chem. A, 2015. **3**(16): p. 8361-8368.

32. Pan, Y., et al., *Core-shell ZIF-8@ZIF-67-derived CoP nanoparticle-embedded N-doped carbon nanotube hollow polyhedron for efficient overall water splitting.* J. Am. Chem. Soc., 2018. **140**(7): p. 2610-2618.

33. Wang, M.Q., et al., *Nanosized metal phosphides embedded in nitrogen-doped porous carbon nanofibers for enhanced hydrogen evolution at all pH values.* Angew. Chem. Int. Ed., 2018. **57**(7): p. 1963-1967.

34. Wu, M.Y., et al., *Designing hybrid NiP_2/NiO nanorod arrays for efficient alkaline hydrogen evolution.* Acs Appl. Mater. Inter., 2018. **10**(21): p. 17896-17902.

35. Xu, K., et al., *Regulating water-reduction kinetics in cobalt phosphide for enhancing HER catalytic activity in alkaline solution.* Adv. Mater., 2017. **29**(28): p. 1606980.

36. Yang, Y., et al., *Porous cobalt-based thin film as a bifunctional catalyst for hydrogen generation and oxygen generation.* Adv. Mater., 2015. **27**(20): p. 3175-3180.

37. Zhao, X.J., et al., *Bifunctional electrocatalysts for overall water splitting from an iron/nickel-based bimetallic metal-organic framework/dicyandiamide composite.* Angew. Chem. Int. Ed., 2018. **57**(29): p. 8921-8926.

38. Qian, M.M., et al., *Highly efficient and stable water-oxidation electrocatalysis with a very low overpotential using FeNiP substitutional-solid-solution nanoplate arrays.* Adv. Mater., 2017. **29**(46): p. 1704075.

39. Chen, P.Z., et al., *3D nitrogen-anion-decorated nickel sulfides for highly efficient overall water splitting.* Adv. Mater., 2017. **29**(30): p. 1701584.

40. Jin, H.Y., et al., *In situ cobalt-cobalt oxide/N-doped carbon hybrids as superior bifunctional electrocatalysts for hydrogen and oxygen evolution.* J. Am. Chem. Soc., 2015. **137**(7): p. 2688-2694.

41. Li, J., et al., *Nanoparticle superlattices as efficient bifunctional electrocatalysts for water splitting.* J. Am. Chem. Soc., 2015. **137**(45): p. 14305-14312.

42. Pan, Y., et al., *A bimetallic Zn/Fe polyphthalocyanine-derived single-atom Fe-N_4 catalytic site:A superior trifunctional catalyst for overall water splitting and Zn-Air batteries.* Angew. Chem. Int. Ed., 2018. **57**(28): p. 8614-8618.

43. Zhu, Y.P., et al., *Self-templating synthesis of hollow Co_3O_4 microtube arrays for highly efficient water electrolysis.* Angew. Chem. Int. Ed., 2017. **56**(5): p. 1324-1328.

Chapter 6 Highly Disordered Cobalt Oxide Nanostructure Induced by Sulfur Incorporation for Efficient Overall Water Splitting

6.1 Introduction

Exhaustible fossil fuels and anabatic environmental pollution have stimulated the demands for renewable energy techniques.[1,2] Electrochemical water splitting ($2H_2O \rightarrow 2H_2 + O_2$) offers a promising route for sustainable hydrogen generation and electric energy storage. However, the development of energy-saving water splitting electrolyzer is hampered by the requirement of high cell voltages (1.8-2.0 V) because of the sluggish electrode reactions, particularly for the pivotal anodic oxygen evolution reaction (OER).[3] Moreover, the use of single-function electrocatalysts for OER and hydrogen evolution reaction (HER) depends on the complex synthesis procedure and multiple operation process, thus resulting in a high practical cost.[4,5] Therefore, highly efficient bifunctional catalysts are the key to overcome these technical issues, enabling cost-saving H_2 production.[6] Transition metal oxides, especially cobalt-based oxides, are the promising and attractive bifunctional alternatives, owing to their high catalytic activities and favorable redox capability.[7] However, the intrinsic catalytic properties of crystalline cobalt-based oxides are far from practical applications. Recent progress has employed several appreciable strategies to enhance their catalytic capabilities, including heterogeneous element doping,[8] supporting carbon-based material,[9,10] strain,[11] structure conversion,[4] amorphization,[12-16] tuning electronic structure[17] and vacancies,[18] etc. Nevertheless, effective approach that permits the control of applicable structure transition are still lacking.

Recently, flexible disordered structure was observed to be favorable to give superior activities of catalysts.[19] The introduction of disorders in catalysts could be a prospective route to implement structure transition, thus boosting the intrinsic catalytic properties. Structural disorder was formed owing to the change of the atomic arrangement and could be introduced via various sources including vacancy, substitution, anti-site, strain, surface roughness or adsorbates.[20,21] Among them, substitutional doping exhibits a tremendous potential for interface structure control and function engineering.[17,22] Our recent work showed a phosphorus-doping-induced structural phase transition for enhanced HER, displaying that the electronegativity of heterogeneous element would build the structure reconstruction and tune the electron orbitals in $CoSe_2$.[23] We assume that an electronegative element incorporation could induce the controllable disordered structure that benefits the electrocatalysis.

In this chapter, we report a structurally disordered cobalt oxide induced by sulfur incorporation (S-CoO_x) catalyst. The S-CoO_x catalyst was synthesized via the incorporation of electronegative sulfur ion into the crystalline cobalt oxide (CoO_x) using a facile room-temperature ion exchange strategy. After the electronegative sulfur incorporation, we observed that the high crystalline state of CoO_x was gradually destroyed and the long-range lattice arrangement was broken into disorganized distribution. These changes lead to the generation of more defect sites and enhanced active low oxygen coordination. Experimental measurements and theoretical calculation results reveal that a preferable electronic state was generated in the disordered S-CoO_x catalyst. These striking features enable S-CoO_x an outstanding electrocatalyst for both HER and OER in alkaline electrolyte. This study

spotlights an accessible structure disorder avenue to develop newly advanced electrocatalysts for water splitting systems.

6.2 Experimental Sections

6.2.1 Chemicals

All chemicals used during this research project, including cobalt nitrate hexahydrate ($Co(NO_3)_2{\cdot}6H_2O$, 98%), ammonium fluoride (NH_4F, 98%), urea (99%), sodium sulfide nonahydrate ($Na_2S{\cdot}9H_2O$, 98%), potassium hydroxide (KOH, 85%), Pt plate (1x1 cm^2), Pt/C (20 wt%), Ir/C (20 wt%) and ethanol (CH_3CH_2OH, 96%), were purchased from Aldrich and used without any further purification.

6.2.2 Synthesis of CoO_x/NF

Prior to the process, the commercial nickel foam substrate was cut into several plates (2.5 x 2.5 cm^2), then these plates were compressed into thinner nickel foam plates with a press machine to improve their wettability. The nickel foam plates (NF) were sequentially cleaned in 3 M HCl aqueous solution for 20 min, deionized water for 5 min and ethanol for 5 min via ultrasonic treatment, then dried in the vacuum oven at 60 ºC. The cobalt-based hydroxide precursor was directly grown onto the nickel foam substrate via a mild hydrothermal process. The typical procedure was as follows: 0.5 mmol $Co(NO_3)_2{\cdot}6H_2O$, 1 mmol NH_4F and 2.5 mmol urea was dispersed in 30 mL deionized water via 30 min continuous magnetic stirring to form a homogeneous solution. Then the obtained pink aqueous solution was decanted into a 50 mL Teflon autoclave containing a clean nickel foam plate. The synthesis process was carried out at 120 ºC for 6 h. After cooling to room

temperature, the obtained precursor was rinsed with deionized water and ethanol several times, then dried at 60 ºC in vacuum. Subsequently, the cobalt oxide grown on nickel foam (CoO_x/NF) product was obtained by annealing the achieved cobalt-based hydroxide precursor at 300 ºC for 1.5 h with a heating rate of 2 ºC /min under a flowing argon atmosphere.

6.2.3 Synthesis of S-CoO_x/NF

The S-CoO_x grown on nickel foam (S-CoO_x/NF) was obtained via a room-temperature sulfur ion exchange process, by immersing the dry CoO_x/NF (1 x 2.5 cm^2) plate into a 15 mL of 0.5 M fresh-prepared Na_2S aqueous solution for 3 h. Control experiments were also operated by varying the immersing times for 0.5 h and 24 h, named as S-CoO_x-0.5h/NF and S-CoO_x-24h/NF, respectively. Finally, the as-synthesized catalysts were washed with deionized water several times and dried at room temperature in vacuum.

6.2.4 Material Characterizations

XRD patterns were obtained via a Bruker D8 Discover using Cu Kα (λ = 0.15406 nm) radiation (40 kV, 40 mA) with a scanning rate of 0.04° s^{-1} from 10° to 80°. SEM images and EDX were operated on a field emission scanning electron microscopy (FESEM, Zeiss Supra 55VP) with an accelerating voltage of 10 kV, equipped with a Rontec EDX system. TEM measurements was conducted on a FEI Tecnai T20 electron microscopy at an accelerating voltage of 200 kV. HRTEM images and element mappings were obtained via a JEOL JEM-2011 and the corresponding SAED patterns were taken via the Gatan charge-coupled device (CCD) camera. Raman spectra were recorded on a Renishaw inVia Raman microscope, with an exposure time of 100 s and laser power of 10% under the excitation

wavelength of 633 nm. The surface area of S-CoO_x was examined using the Brunauer-Emmett-Teller (BET) method via the nitrogen adsorption-desorption process. XPS was obtained via an ESCALab MKII X-ray photoelectron spectrometer with an X-ray source.

6.2.5 Electrochemical Measurements

The electrochemical performances were operated during a standard three-electrode system using a CHI660D Instrument Potentialstat, with a saturated Ag/AgCl electrode (0.197 V vs. normal hydrogen electrode (NHE)) and a graphite rod as the reference electrode and counter electrode, respectively. The prepared materials were served as the working electrode, and 1.0 M KOH aqueous solution was used as the electrolyte. 5 mg commercial Ir/C (20 wt%) or Pt/C (20 wt%) was dispersed in 1mL of ethanol with 40 μL of 5wt% Nafion as the binder, then coated onto nickel foam as the control experiments. All the potentials during this paper were converted to RHE (reversible hydrogen electrode) via the formula for Nernst equation: $E_{RHE} = E_{Ag/AgCl} + 0.197 + 0.059 \times pH$ if without other statements and all the current densities were calculated according to the geometrical surface area of the working electrodes. Polarization curves were run at the scan rate of 5 mV s^{-1} with iR compensation. The Tafel plots were obtained via replotting the polarization curves using overpotential versus log current density, the Tafel slopes were calculated via the fitting linear portion from the Tafel plot using the following formula:[1]

$$\eta = a + b \cdot \log(j) \qquad (1)$$

Where η is overpotential, b is Tafel slope and j is current density. During the process of oxygen evolution reaction (OER), overpotential η was calculated via the formula $\eta = E - 1.23$ V. Where E is the potential vs. RHE.

Stability tests were operated via the polarization curves cyclic measurements at the scan rate of 50 mV s^{-1} for 1000 cycles or through the electrolysis test at the constant potentials. To reflect the exposed electrochemical active surface area, double layer capacitance (C_{dl}) was calculated via the cyclic voltammograms (CVs) tests at the different scan rates using the formula as follows:[24]

$$i_c = v \cdot C_{dl} \quad (2)$$

Where i_c and v represent the charging current density and the scan rate, respectively. The electrical impedance spectroscopy (EIS) was obtained at the frequency from 10^5 Hz to 0.001 Hz, the voltage amplitude is 5 mV. Overall water splitting was accomplished in a two-electrode system, with S-CoO_x/NF used as both anode and cathode in 1.0 M KOH aqueous solution. The control experiments were operated with Ir/C and Pt/C as the anode and cathode, respectively.

6.2.6 DFT Calculations

DFT calculations were operated with the Vienna ab initio simulation package, by assuming that every metal atom of the catalysts is involved during the catalysis process. All geometry optimization and energy calculations were performed within the CASTEP module in Materials Studio based on the density functional theory (DFT).[25] The projector augmented wave (PAW) method[26] and generalized gradient approximation (GGA) functional of Perdew, Burke, and Enzerhof (PBE) were adopted in the present calculations.[27] The semi-empirical London dispersion corrections of Grimme et al were conducted to calculate the interactions between absorbers and samples. The plane-wave cut-off energy level for all calculations were set as 480 eV in geometry optimization and 600 eV in energy calculation,

the SCF tolerance level was as 1.0×10^{-5} au in geometry optimization, while SCF tolerance was set as 1.0×10^{-6} au for energy calculation. The k space was sampled with a Γ point centered at $4 \times 4 \times 1$ in geometry optimizations and at $6 \times 6 \times 1$ in energy calculations. During surface adsorption calculations, a $2 \times 2 \times 3$ supercell with (100) surface for CoO model and a $1 \times 1 \times 2$ supercell with (010) surface for Co_3O_4 model were used along with a 20 Å vacuum.

The free energy of the adsorbed state is calculated as follows based on the adsorption energy:

$$\Delta G_{ad} = \Delta E_{ad} + \Delta E_{ZPE} - T\Delta S \quad (3)$$

where ΔE_{ad} is the adsorption energy, and ΔE_{ZPE} is the difference corresponding to the zero point energy between the adsorbed state and the gas phase.

During DFT calculations, the OER process was divided into four elementary steps, including:

$$OH^- + * \rightarrow *OH + e^- \quad (4)$$

$$*OH + OH^- \rightarrow *O + H_2O + e^- \quad (5)$$

$$*O + OH^- \rightarrow *OOH + e^- \quad (6)$$

$$*OOH + OH- \rightarrow * + O_2 + H_2O + e^- \quad (7)$$

Here, the (*) denotes the surface of CoO, Co_3O_4, S-CoO or S-Co_3O_4.[11]

6.3 Results and Discussions

6.3.1 Material Morphology and Analysis

As schematically illustrated in **Figure 6.1a** and **Figure 6.2**, a facile room-temperature ion exchange strategy was used to incorporate sulfur into the as-synthesized CoO_x. Briefly,

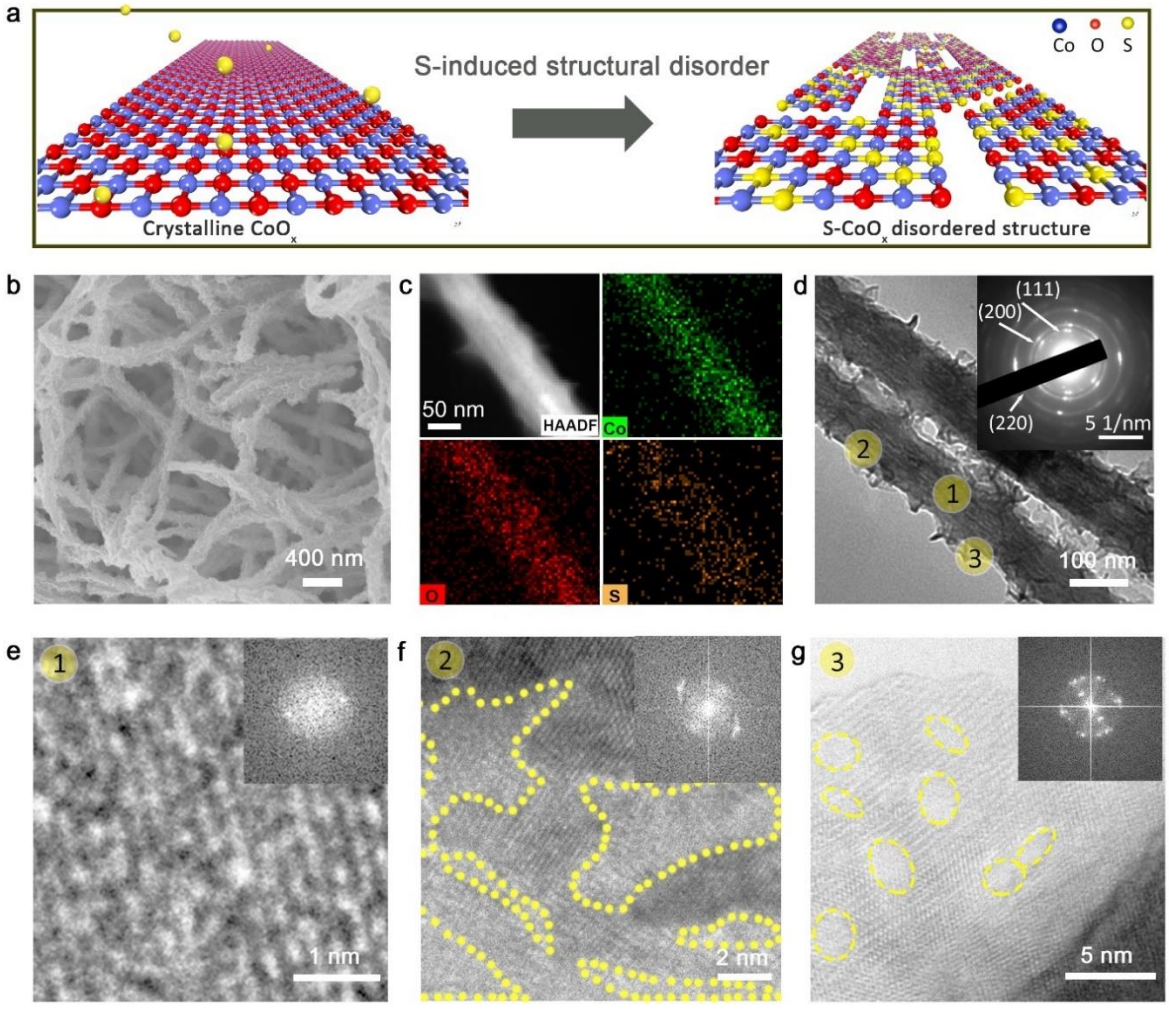

Figure 6.1 (a) Schematic illustration for the synthesis of S-CoO_x. (b-g) SEM, STEM elemental mapping, TEM and HRTEM images of S-CoO_x. Inset in (d) shows the SAED patterns and insets in (e-g) show the corresponding FFT patterns of S-CoO_x. (e-g) are from the areas 1-3 of (d), respectively.

CoO_x on a nickel foam (CoO_x/NF) was prepared through a modified hydrothermal-then-annealing method as described in the above experimental section (**Figure 6.3**).[28] After that, S-CoO_x/NF product was obtained by immersing the prepared CoO_x/NF into a 0.5 M Na_2S aqueous solution for 3 h under ambient temperature.[29] The mass loading of S-CoO_x on the nickel foam substrate was ~ 2.10 mg cm^{-2}. We propose that the new structural disorder in S-CoO_x could be ascribed to the electronegative sulfur incorporation. When the bigger heterogeneous sulfur atoms partially substitutes smaller O atoms in the host crystalline CoO_x, the induced increment of lattice damage and the influence on the electron densities characteristics of Co atoms are generated. This special phenomenon could be owing to the electronegativity of sulfur ion and different atom radius between sulfur atoms and oxygen atoms, thus resulting in the destruction of crystalline CoO_x and therefore the formation of the structural disorder.[30,31]

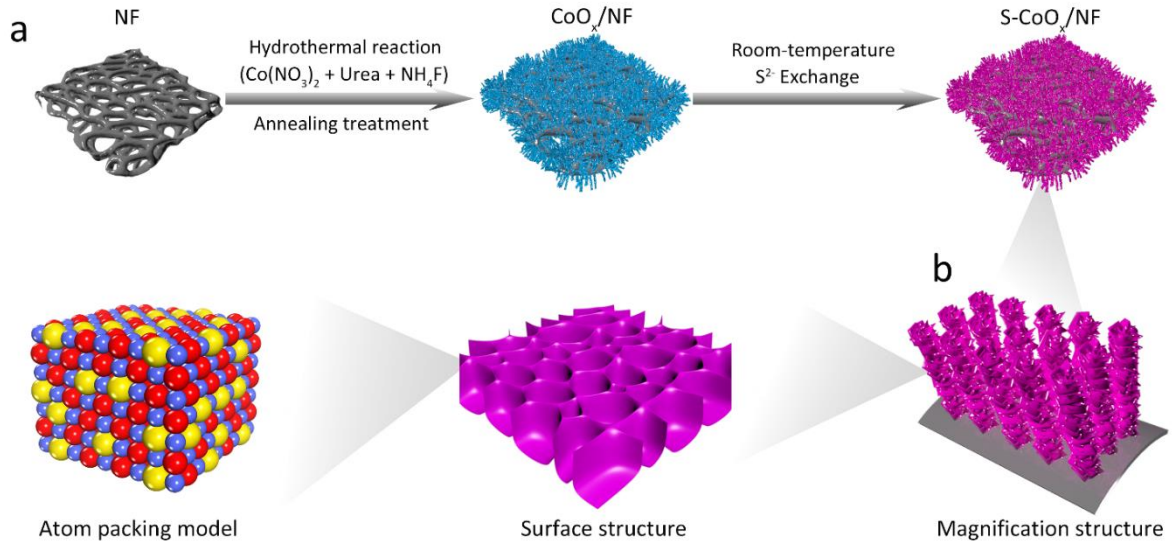

Figure 6.2 (a) Schematic illustration of the synthetic procedure for S-CoO_x/NF. (b) The morphology structure and atom packing model for S-CoO_x. Co blue, O red and S yellow.

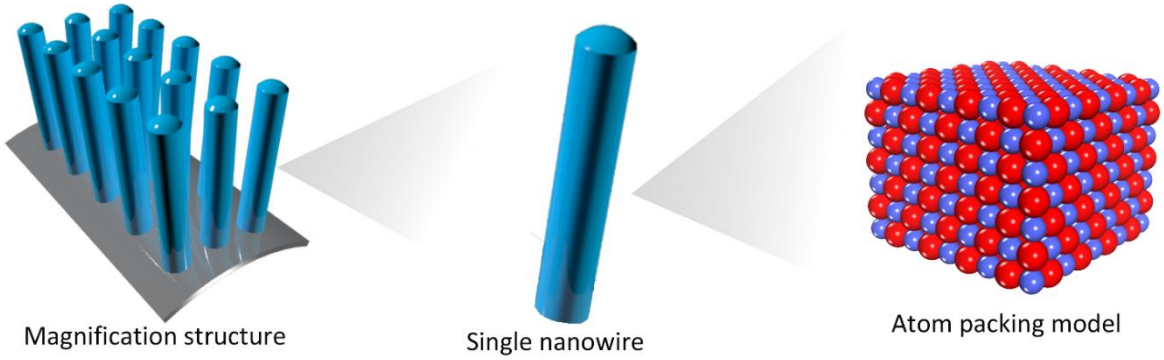

Figure 6.3 The morphology structure and atom packing model for the CoO_x. Co blue and O red.

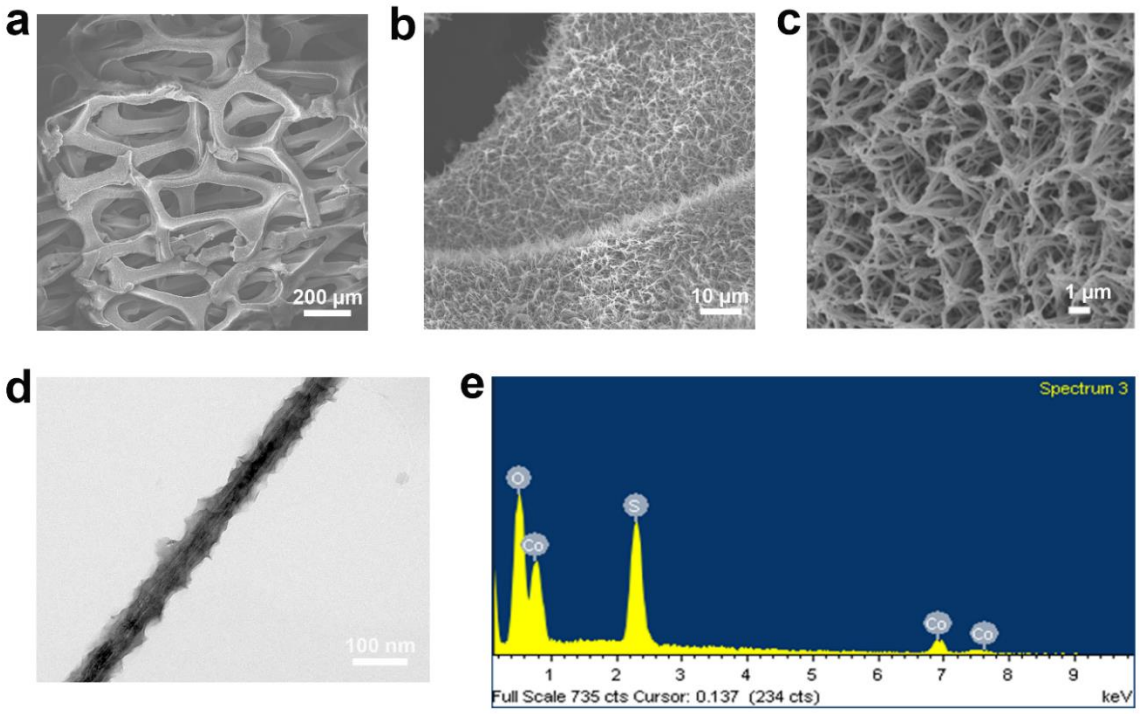

Figure 6.4 (d) TEM image and (e) Energy-dispersive X-ray (EDX) patterns of S-CoO_x. The S-CoO_x powder was obtained by ultrasound from S-CoO_x/NF catalyst.

Scanning electron microscopy (SEM) and transmission electron microscopy (TEM) images of S-CoO_x show that the rough nanowires covered with numerous nanosheets, the

diameters of nanowires are 50-100 nm and the sizes of nanosheets are 20-40 nm (**Figure**

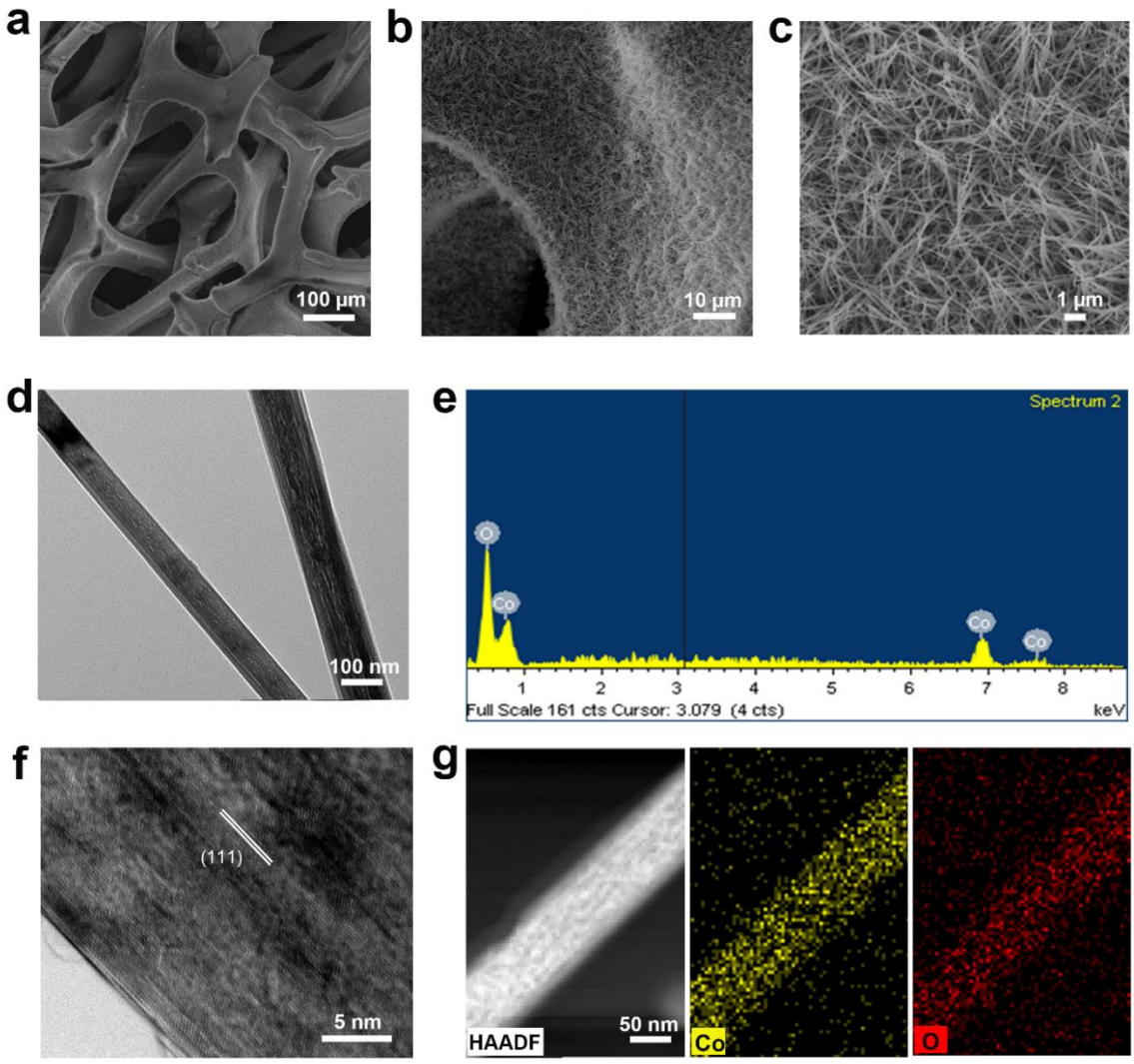

Figure 6.5 (a-c) SEM images of CoO_x/NF. (d) TEM image and (e) EDX patterns of CoO_x. (f and g) HRTEM and STEM-EDX mapping images of CoO_x. The CoO_x powder was obtained by ultrasound from CoO_x/NF catalyst.

6.1b and **Figure 6.1d**). The rough nanowires of S-CoO_x were uniformly grown on the clean nickel foam, evolved from the previous smooth nanowires of CoO_x (**Figure 6.4** and **6.5**). Scanning TEM (STEM) elemental mapping results reveal that Co, O and S elements are uniformly distributed on the rough nanowire (**Figure 6.1c**). High-resolution TEM

(HRTEM) images of S-CoO_x show three different regions from a single S-CoO_x rough nanowire. HRTEM image in **Figure 6.1e** demonstrates that lattice fringes of the interior S-CoO_x were already highly disorganized with the incorporation of sulfur. The middle region of the S-CoO_x exhibits that the wide range of existing disorganized lattice fringes were formed (**Figure 6.1f**). **Figure 6.1g** shows that the external S-CoO_x region also includes the newly formed nanosheets as well as the wide disordered lattice fringe areas. The formation

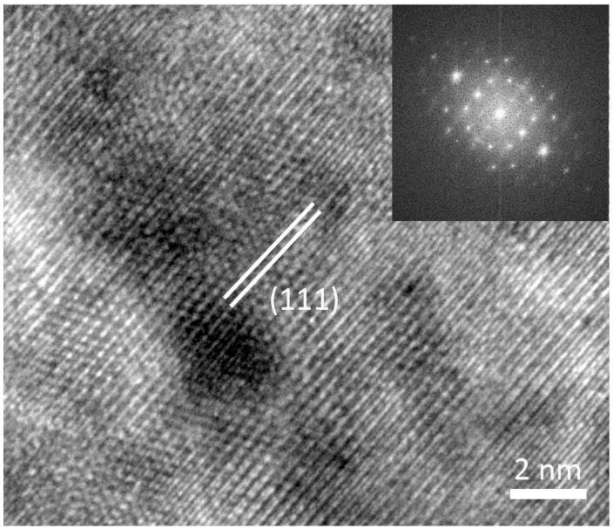

Figure 6.6 HRTEM images of CoO_x. Inset shows the corresponding FFT of CoO_x. The CoO_x powder was obtained by ultrasound from CoO_x/NF catalyst.

Table 6.1 Comparison of the atomic ratio for the obtained samples via EDX analysis.

Samples	Elements		Atomic Ratio
CoO_x/NF	O	S	1 : 0
S-CoO_x-0.5h/NF	O	S	3.93 : 1
S-CoO_x/NF	O	S	2.98 : 1
S-CoO_x-24h/NF	O	S	2.40 : 1

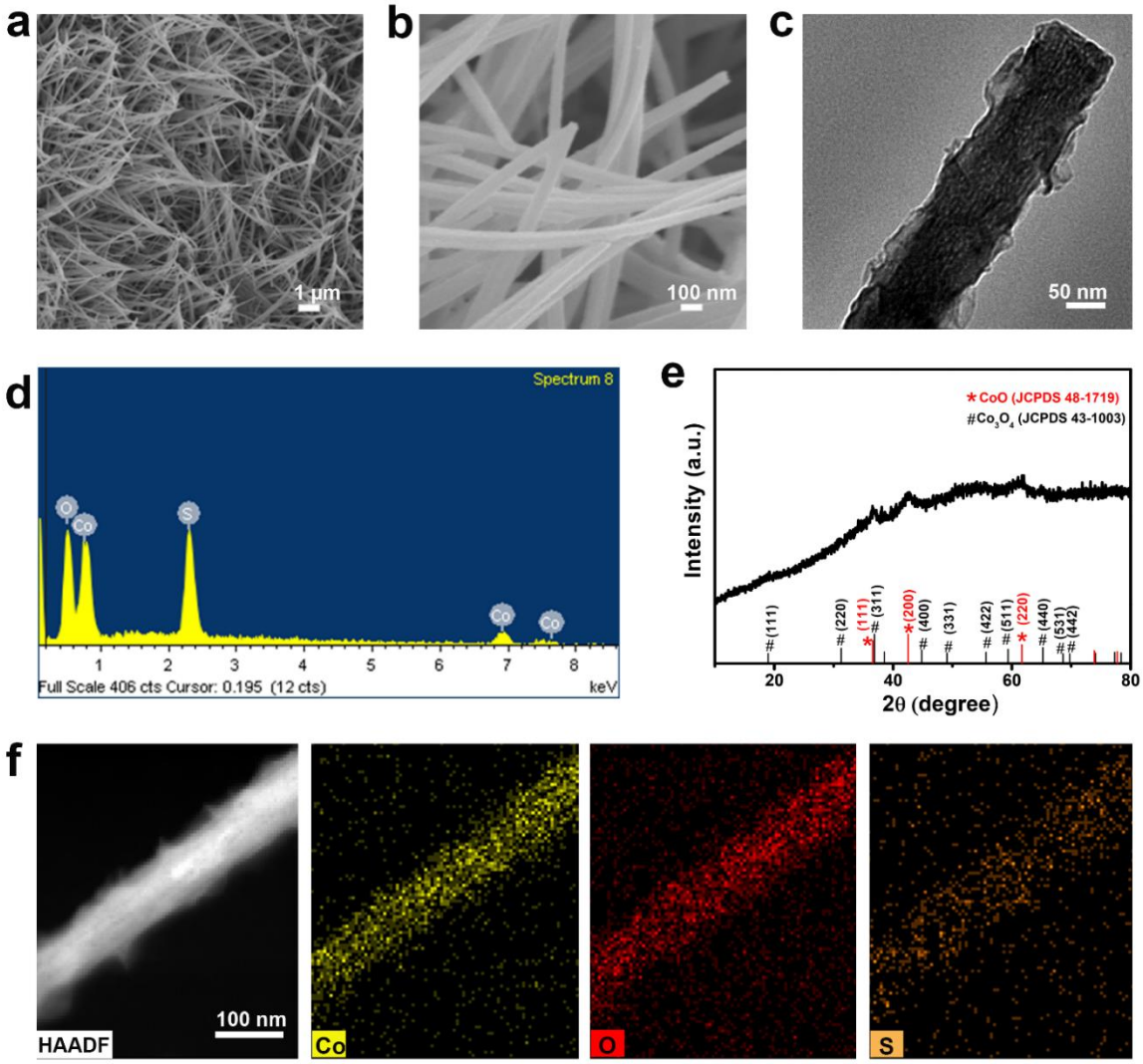

Figure 6.7 Characterization of S-CoO_x-0.5h. (a and b) SEM images of S-CoO_x-0.5h/NF. (c) TEM image, (d) EDX and (e) XRD patterns of S-CoO_x-0.5h. (f) STEM-EDX mapping images of S-CoO_x-0.5h. The S-CoO_x-0.5h powder was obtained by ultrasound from S-CoO_x-0.5h/NF catalyst. The S-CoO_x-0.5h/NF catalyst was obtained after 0.5h room-temperature sulfur ion exchange reaction. The XRD analysis shows that the diffraction peaks were weakened compared with that of the prepared CoO_x.

of nanosheets could be attributed to the intense and direct reaction between outer structure of cobalt oxide and electronegative sulfur during the ion exchange process. To estimate the degree of structural disorder in S-CoO_x, selected-area electron diffraction (SAED) analysis

(Inset, **Figure 6.1d**) and corresponding fast Fourier transform (FFT) patterns (Inset, **Figure 6.1e-g**) were investigated. These diffraction rings are significantly different from the single-crystalline-like clear diffraction spots in CoO_x (**Figure 6.6**), confirming the heavily

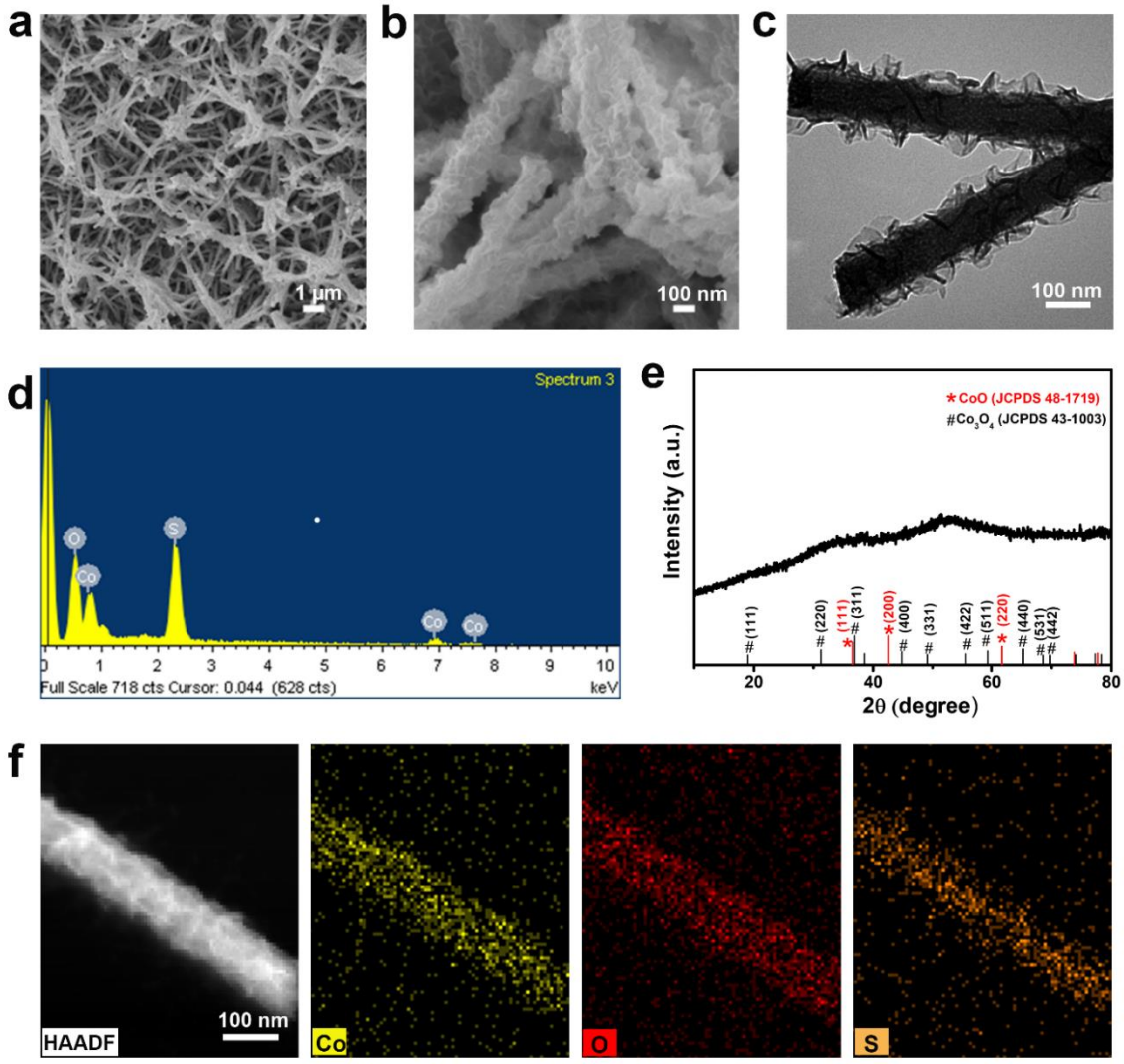

Figure 6.8 Characterization of S-CoO_x-24h. (a and b) SEM images of S-CoO_x-24h/NF. (c) TEM image, (d) EDX and (e) XRD patterns of S-CoO_x-24h. (f) STEM-EDX mapping images of S-CoO_x-24h. The S-CoO_x-24h powder was obtained by ultrasound from S-CoO_x-24h/NF catalyst. The S-CoO_x-24h/NF catalyst was obtained after 24h room-temperature sulfur ion exchange reaction. The XRD analysis shows that no obvious diffraction peaks were observed, which are consistent with that of S-CoO_x.

disordered lattice arrangements.[19,22] It should be noted that the controllable sulfur incorporation and structural disorder can be adjusted via varying the immersing times during ion exchange process (**Figure 6.7-6.8**, **Table 6.1**).

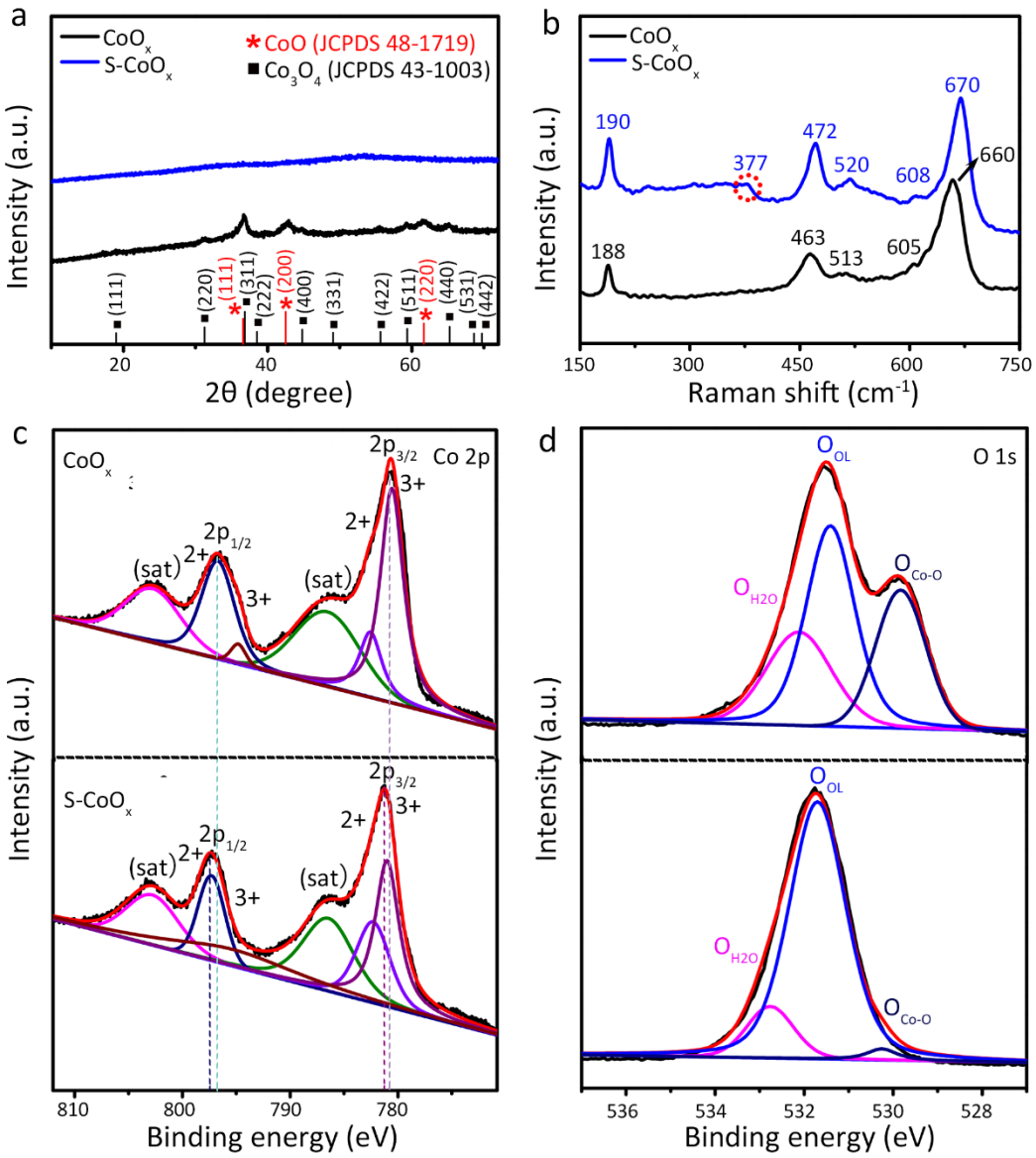

Figure 6.9 Characterization of CoO_x and S-CoO_x. (a) XRD patterns and (b) Raman spectra of CoO_x and S-CoO_x. (c and d) High resolution XPS spectra for Co 2p and O 1s of CoO_x and S-CoO_x, respectively.

The crystal structure of the catalysts was analyzed via X-ray diffraction (XRD) measurement. As shown in **Figure 6.9a**, the diffraction peaks for CoO_x can be attributed to cubic CoO (JCPDS 48-1719) and cubic Co_3O_4 (JCPDS 43-1003), where the main composition is cubic CoO. By sharp contrast, no obvious diffraction peaks were observed

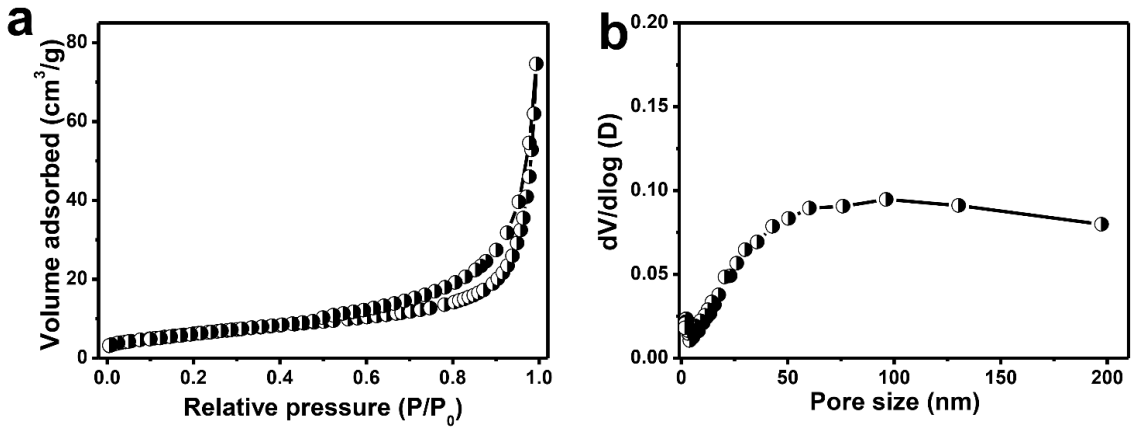

Figure 6.10 BET analyses. (a) Nitrogen adsorption-desorption isotherm for S-CoO_x. (b) The corresponding pore size distribution. The BET surface area of the S-CoO_x catalyst was determined to be 23.3 m^2 g^{-1}.

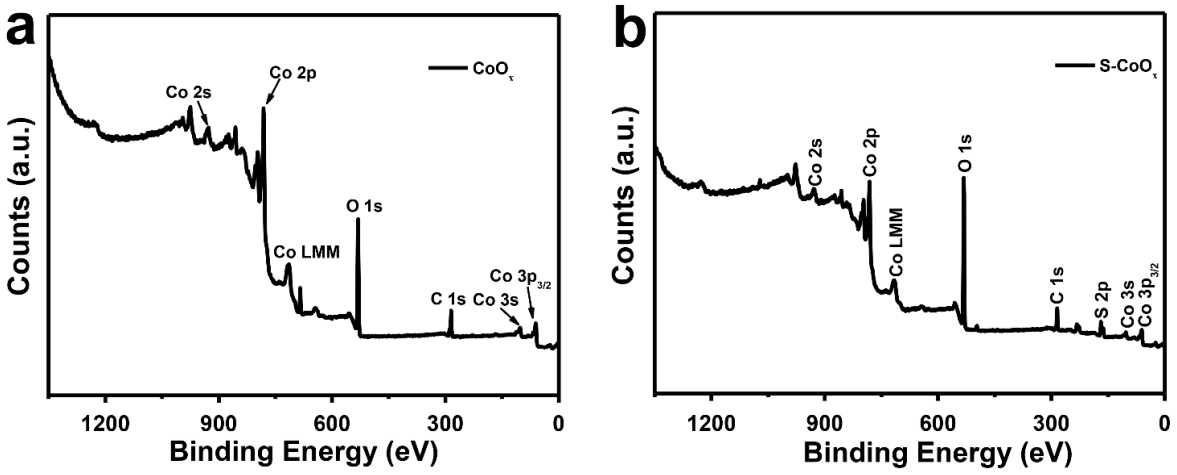

Figure 6.11 XPS survey spectra for (a) CoO_x and (b) S-CoO_x.

in S-CoO_x. The disappeared diffraction peaks in S-CoO_x confirm that the long-range order in the crystalline form of CoO_x has been disturbed after sulfur incorporation, which are

distinguishable from the original CoO_x. The similar vibration peaks in Raman analysis indicate a similar chemical composition and phase for S-CoO_x and CoO_x (**Figure 6.9b**). Detailed analysis for the original crystalline CoO_x shows that the peaks at 188, 463 cm^{-1} could be attributed to the vibration of Co(II)-O coordination, the peaks at 513, 605 and 660 cm^{-1} correspond to the vibration of Co(III)-O coordination.[32,33] After S incorporation, the existing peaks of S-CoO_x are all blue-shift to 190, 472, 520, 608 and 670 cm^{-1} compared to the results of crystalline CoO_x. Besides, a new peak at 377 cm^{-1} was formed, which could be ascribed to the Co-S coordination vibration.[32,33] The blue-shift Raman signals and the new emerged peak were indispensable with the elemental incorporation, which might be ascribed to that the bigger S ions partially substitutes the smaller O atoms or the formative disordered structure transition.[30,34,35] Moreover, the Raman peak intensities of the Co(II)-O vibration have been enhanced after sulfur incorporation, probably resulting from the influence of electronegative sulfide ions.[36]

BET surface area of S-CoO_x catalyst was about 23.3 m^2 g^{-1} (**Figure 6.10**). Surface chemistry information was further investigated by X-ray photoelectron spectroscopy (XPS). XPS survey spectra show that the dominated elements for S-CoO_x and CoO_x were consistent with the above results (**Figure 6.11**). Co 2p spectra for S-CoO_x and CoO_x exhibit the existence of divalent (Co^{2+}), trivalent cobalt (Co^{3+}) and their shake-up satellites (sat) (**Figure 6.9c**). The peaks at Co $2p_{3/2}$ and Co $2p_{1/2}$ were shifted to higher binding energy after sulfur incorporation, which results from the altered electron densities around Co atoms and can be attributed to the drastic distortion of crystal structure.[37-40] Meanwhile, O 1s spectra could be divided into three peaks. The component O_{Co-O} is a typical metal-oxygen

bond and the O_{OL} peak at around 531.5 eV could be attributed to the oxygen ions in low

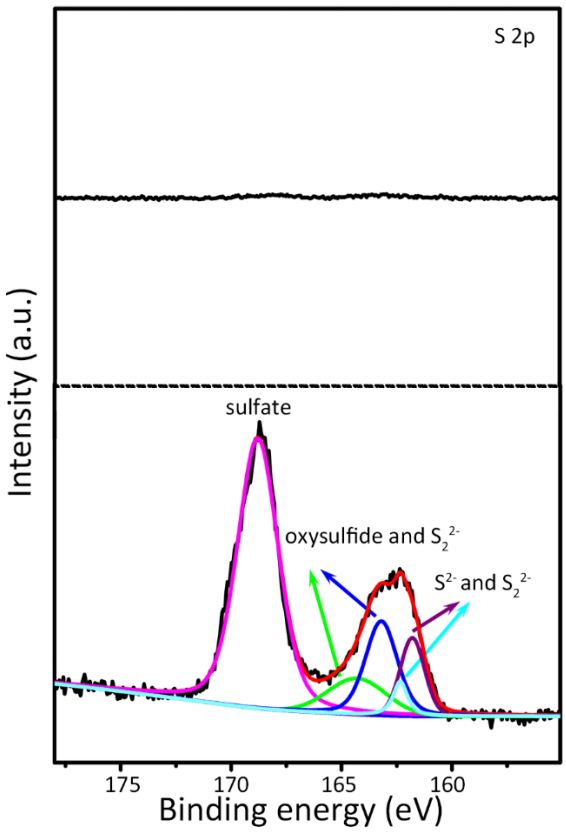

Figure 6.12 High resolution XPS spectra for S 2p of CoO_x (above) and S-CoO_x (below).

coordination, coming from the numerous defect sites.[18] The O_{H2O} peak at 532.2 eV is associated with the physi- and chemisorbed water on or within the material surface.[41] The area percentage for O_{Co-O}, O_{OL} and O_{H2O} in CoO_x is 30%, 43.6% and 26.4%, respectively. After sulfur incorporation, the O_{OL} peak had been greatly increased to 84.6%, indicating that more defect sites have been formed (**Figure 6.9d**).[42] S 2p spectra in S-CoO_x also include several components. The peaks at 161.8 and 162.4 eV are consistent with S ion (S^{2-}) and part of terminal S_2^{2-}, the peaks at 163.2 and 164.4 eV correspond to bridge S_2^{2-} and oxysulfide, and the peak at 168.8 eV could be ascribed to the re-oxidation of the S ion (**Figure 6.12**).[43-45] The results reveal that S ion has been partially oxidized owing to the

existed oxygen atoms. Raman and XPS analysis for S-CoO_x uncover the existence of Co-S bond and intimate connection between S and O, confirming our assumption that S atoms partially substitutes O atoms. Additionally, S-CoO_x catalyst also bears rich defect sites and more low oxygen coordination, which would be beneficial to the electrocatalytic activities.

6.3.2 Electrochemical HER Performances

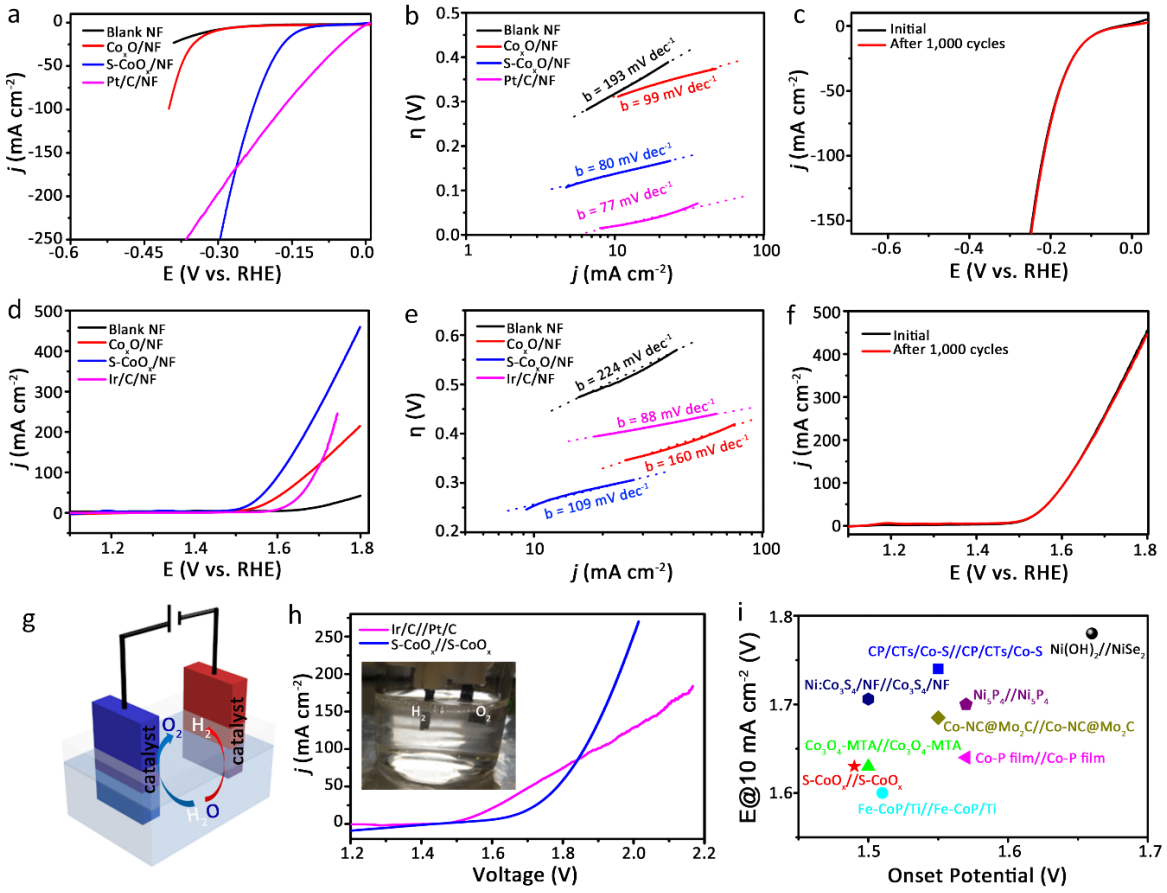

Figure 6.13 Electrocatalytic activities. (a and b) Polarization curves and the corresponding Tafel plots of the catalysts for HER electrolysis. (c) Polarization curves of S-CoO_x/NF for the HER before and after 1000 cycles. (d and e) Polarization curves and the corresponding Tafel plots of the catalysts for OER activities. (f) Polarization curve of S-CoO_x/NF for the OER before and after 1000 cycles. (g) The schematic for overall water splitting. (h) Polarization curve for overall water splitting using S-CoO_x/NF as both anode and cathode

in a two-electrode setup. For comparation, Ir/C and Pt/C coated on nickel foam used as anode and cathode, respectively. (i) Comparison of the electrocatalytic overall water splitting performances for S-CoO_x/NF and the recently reported bifunctional electrocatalysts. Scan rate is 5 mV s^{-1}.

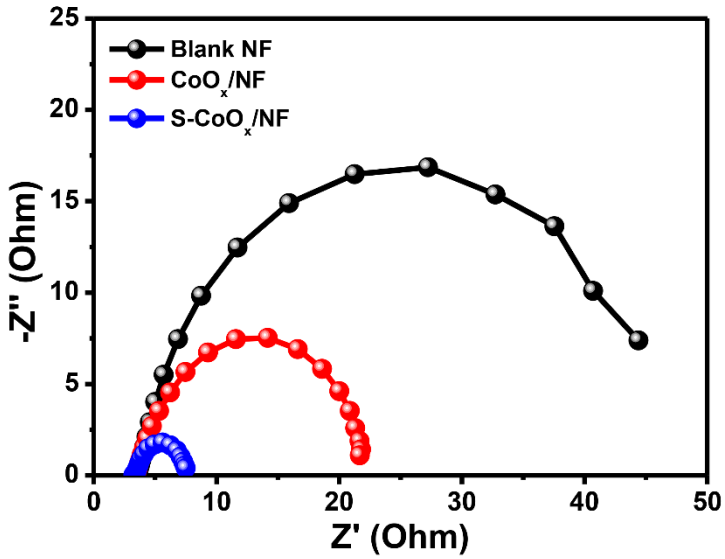

Figure 6.14 EIS Nyquist plots of blank NF, CoO_x/NF and S-CoO_x/NF for HER at 200 mV overpotential. Z′ means the real impedance and Z″ means the imaginary impedance. EIS Nyquist plots show that the R_{ct} of S-CoO_x/NF is 7.5 Ω at 200 mV overpotential, whereas, 21.6 Ω and 45 Ω for CoO_x and blank NF, respectively.

Electrocatalytic activities of the catalysts were evaluated in a three-electrode set-up system using a saturated Ag/AgCl electrode and a graphite rod as the reference electrode and counter electrode, respectively. 1 M KOH aqueous solution was used as the electrolyte, in which the HER kinetics on platinum are two orders of magnitude sluggish than in acidic medium.[23] During HER electrolysis, the polarization curves of the catalysts in **Figure 6.13a** shows that the overpotential (ŋ) for S-CoO_x/NF at the current density of 10 mA cm^{-2} is 136 mV, which is largely lower than 313 mV for CoO_x/NF. It is also remarkable that S-CoO_x/NF catalyst even exhibits a better HER activity than the commercial Pt/C (20 wt%)

on a nickel foam (Pt/C/NF) at large current densities (>167 mA cm^{-2}). These advantages of

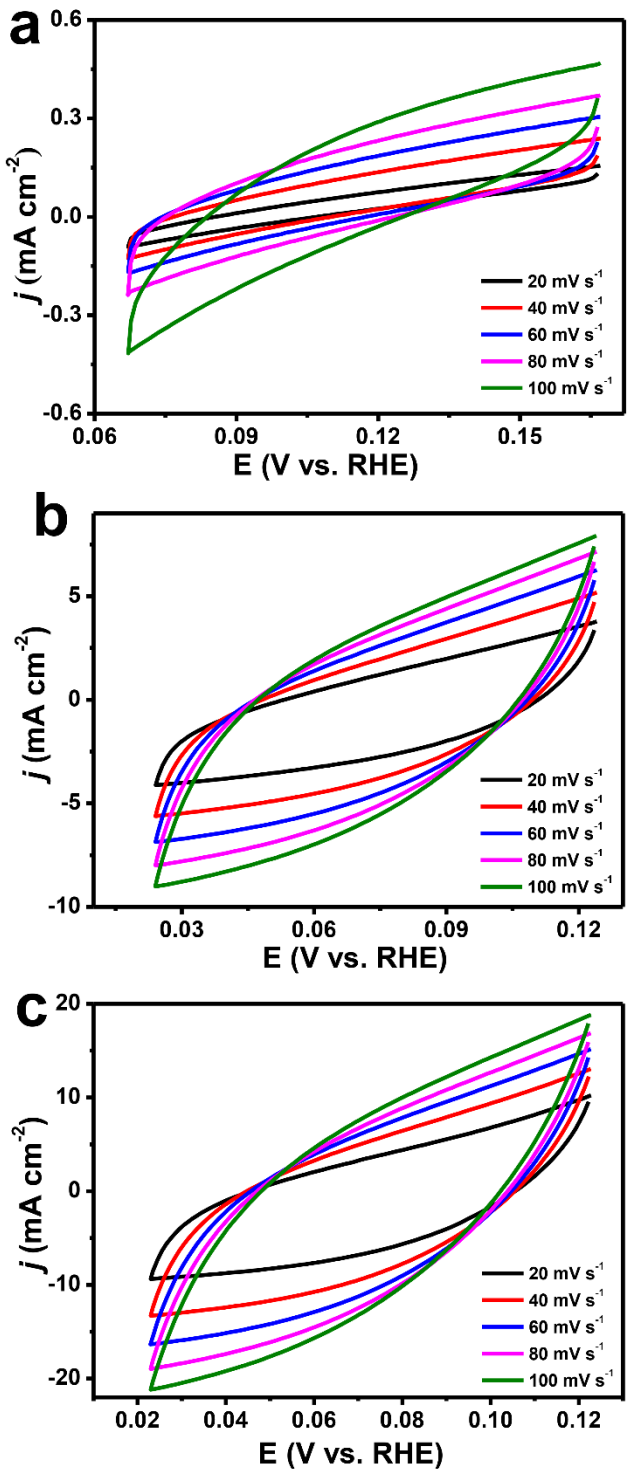

Figure 6.15 CV curves of (a) the blank NF, (b) CoO_x/NF and (c) S-CoO_x/NF at different scan rates, from 20 to 100 mV s^{-2}.

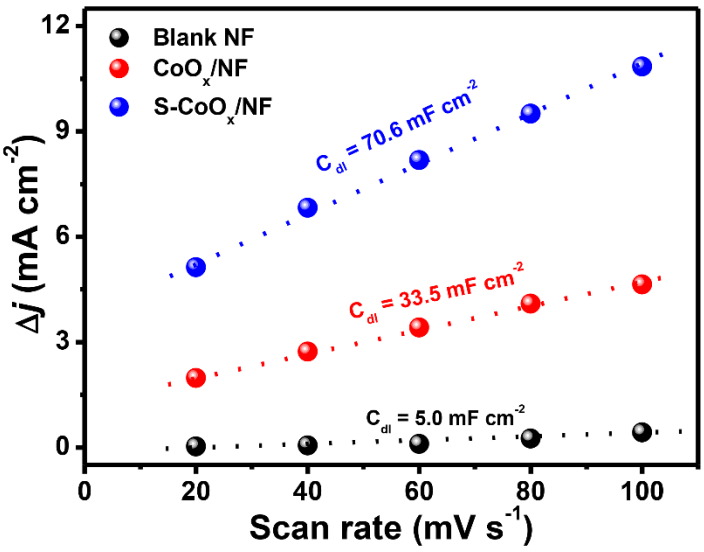

Figure 6.16 The calculated C_{dl} for the blank NF, CoO_x/NF and S-CoO_x/NF.

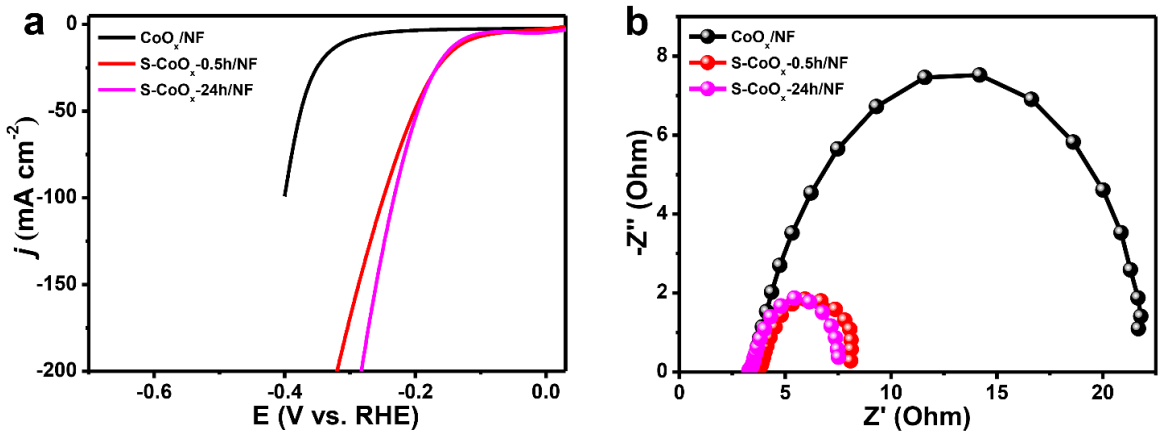

Figure 6.17 HER activities. (a) Polarization curves of CoO_x/NF, S-CoO_x-0.5h/NF and S-CoO_x-24h/NF at 5 mV s^{-1}. (b) EIS Nyquist plots of CoO_x/NF, S-CoO_x-0.5h/NF and S-CoO_x-24h/NF at 200 mV overpotential.

S-CoO_x/NF catalyst might mainly be caused by the increased defect sites due to the structural disorder of S-CoO_x. Besides, the corresponding Tafel slopes of S-CoO_x/NF and CoO_x/NF are 80 and 99 mV dec^{-1}, respectively (**Figure 6.13b**). The lower Tafel value of S-CoO_x/NF suggests a superior catalytic kinetics for S-CoO_x/NF compared with the crystalline CoO_x/NF.

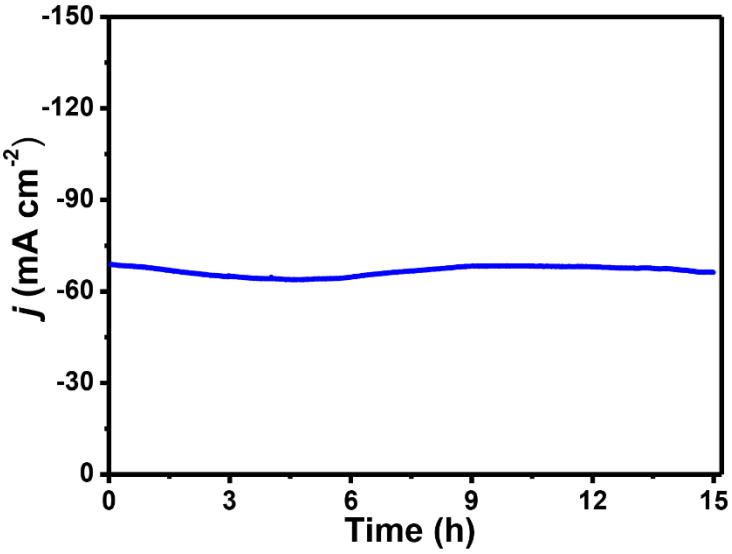

Figure 6.18 Chronoamperometry (*j*–t) curve of S-CoO_x/NF for the HER electrolysis at the constant potential of -0.21 V.

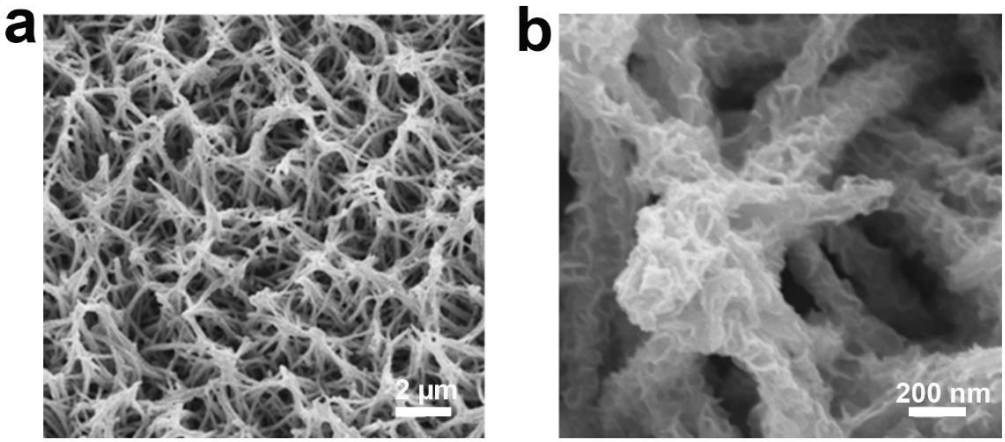

Figure 6.19 (a and b) SEM images of S-CoO_x/NF after long-term HER cyclic test in 1.0 M KOH electrolyte.

To further explore the HER process, electrochemical impedance spectroscopy (EIS) Nyquist plots were recorded at the overpotential of 200 mV. The charge transfer resistance (R_{ct}) value of S-CoO_x/NF is 7.5 Ω, while the R_{ct} value of CoO_x/NF and blank NF is 21.6 Ω and 45 Ω, respectively. The R_{ct} value of S-CoO_x/NF is the smallest, thus revealing a

facilitated HER charge transfer kinetics (**Figure 6.14**). To evaluate the effective

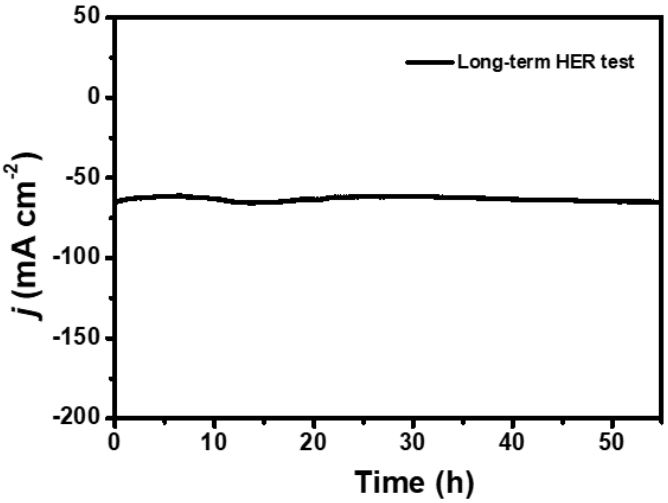

Figure 6.20 Chronoamperometry (*j*–t) curve of S-CoO_x/NF for the long-term HER electrolysis when the current density is about 60 mA cm^{-2}.

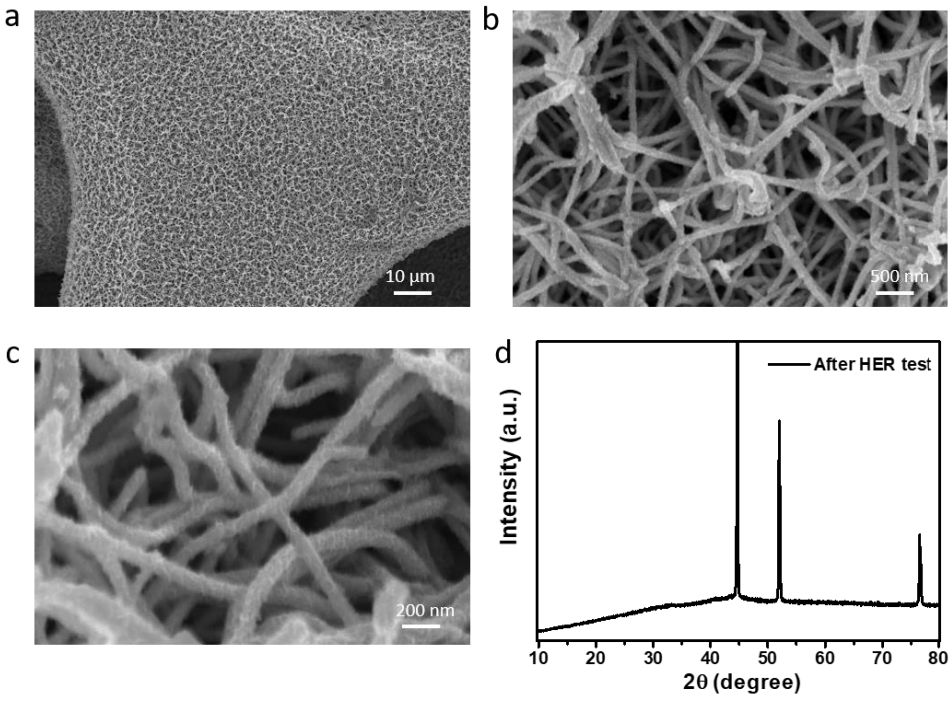

Figure 6.21 (a-c) SEM images and (d) XRD patterns of the S-CoO_x/NF after long-term HER electrolysis. The diffraction peaks in the XRD patterns is the peaks from the nickel foam substrate, no other peaks were formed.

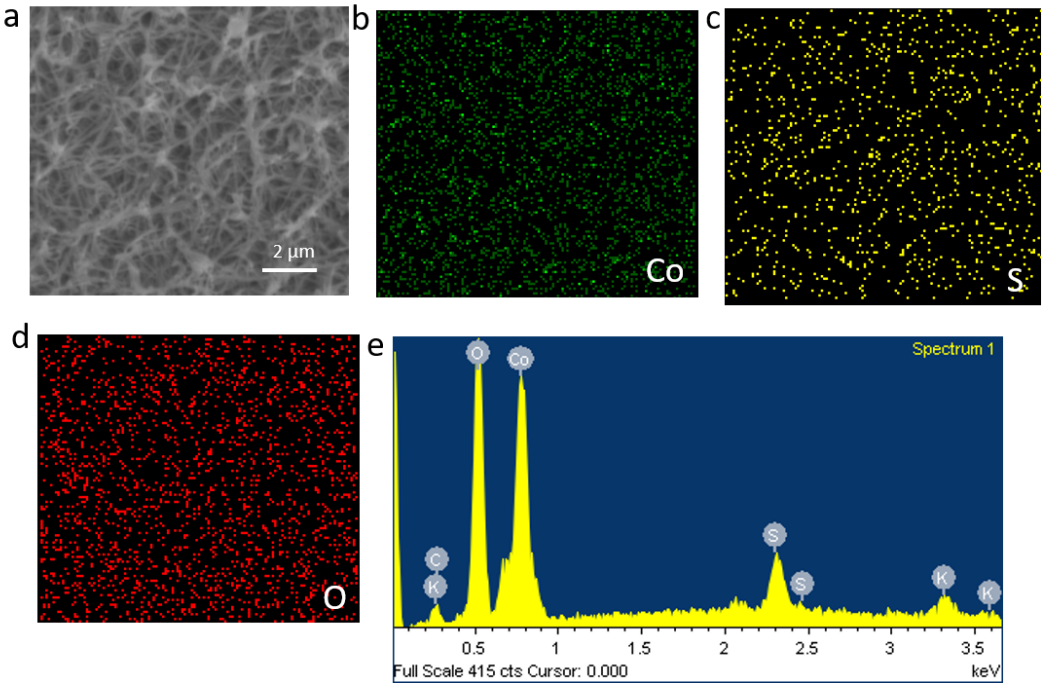

Figure 6.22 (a-d) SEM mapping images and (c) EDX patterns of the S-CoO_x/NF after long-term HER electrolysis.

electrochemically active surface area of the catalysts, the double-layer capacitance (C_{dl}) was measured. The C_{dl} value for S-CoO_x/NF is 70.6 mF cm^{-2}, which was much bigger than 33.5 mF cm^{-2} for CoO_x/NF and 5.0 mF cm^{-2} for blank NF, respectively (**Figure 6.15-6.16**). The result exhibits that the S-CoO_x/NF catalyst possesses more accessible active sites than the prepared CoO_x/NF. Polarization curves and EIS Nyquist plots for the control experiments including S-CoO_x-0.5h/NF and S-CoO_x-24h/NF also confirm the enhanced HER activities after sulfur incorporation compared to that of CoO_x/NF catalyst (**Figure 6.17**). Another important parameter is the stability which was also explored. During HER process, the stability of S-CoO_x/NF catalyst was identified via the accelerated cyclic voltammetry cycling tests composing of 1000 cycles and the long-term chronoamperometry (j–t) curve operated at the current density > 60 mA cm^2 (**Figure 6.13c** and **Figure 6.18**). SEM images of the S-CoO_x/NF catalyst after long-term HER test also show that no change

in morphology was observed after the long-term HER electrolysis (**Figure 6.19**). The various characterizations including long-term chronoamperometry curves, SEM images, XRD patterns, SEM mapping images and EDX patterns for the S-CoO_x/NF catalyst which was collected after the longer long-term electrolysis (more than 50 h, current density > 50 mA cm^{-2}), all further proved its excellent stability (**Figure 6.20-22**). The marked HER activity and stability of S-CoO_x/NF catalyst represent one of the most promising low-cost alternatives to platinum for the HER catalysis in alkaline solution (**Table 6.2**).

Table 6.2 Comparison of the electrocatalytic performance during HER process among the highly active non-precious catalysts.

Catalyst	Tafel slope (mV dec^{-1})	η@10 mA cm^{-2} (mV)	Onset potential (mV vs. RHE)	Substrate	Electrolyte	Reference
S-CoO_x	80	136	-86	Ni foam	1.0 M KOH	This work
N-Ni_3S_2	NA	110	NA	Ni foam	1.0 M KOH	43
Co_3O_4-MTA	98	<190	-100	Ni foam	1.0 M KOH	39
CP/CTs/Co-S	131	190	NA	Cabon paper	1.0 M KOH	46
MoP	NA	~130	NA	Glassy carbon	1.0 M KOH	47
$NiFeO_x$	84.6	88	-40	Carbon fiber paper	1.0 M KOH	4
Fe-Ni@NC-CNTs	113.7	202	NA	Glassy carbon	1.0 M KOH	48
$NiSe_2$	76.6	184	NA	Carbon paper	1.0 M KOH	49
CoO_x@CN	NA	<134	NA	Ni foam	1.0 M KOH	50
Co_1Mn_1CH	NA	180	NA	Ni foam	1.0 M KOH	51
Ni_3S_2	NA	223	NA	Ni foam	1.0 M NaOH	52
Ni_5P_4	53	150	NA	Ni foil	1.0 M KOH	53
Co-NRCNTs	NA	370	-160	Glassy carbon	1.0 M KOH	54
$Cu_{0.3}Co_{2.7}P$/NC	122	220	NA	Glassy carbon	1.0 M KOH	55
Co-NC@Mo_2C	65	99	NA	Glassy carbon	1.0 M KOH	56
Ni:Co_3S_4	91	199	NA	Ni foam	1.0 M KOH	57
Co-MoS_2	158	203	NA	Glassy carbon	1.0 M KOH	58

6.3.3 Electrochemical OER Performances

Table 6.3 Comparison of the electrocatalytic performance during OER process among the highly active non-precious catalysts.

Catalyst	Tafel slope (mV dec^{-1})	η@10 mA cm^{-2} (mV)	Onset potential (V vs. RHE)	Substrate	Electrolyte	Reference
S-CoO_x	109	270	1.48	Ni foam	1.0 M KOH	This work
N-Ni_3S_2	70	~300	NA	Ni foam	1.0 M KOH	43
Co_3O_4-MTA	84	~310	1.51	Ni foam	1.0 M KOH	39
CP/CTs/Co-S	72	306	NA	Cabon paper	1.0 M KOH	46
$NiFeO_x$	31.5	<270	1.43	Carbon fiber paper	1.0 M KOH	4
CoO_x@CN	NA	260	NA	Ni foam	1.0 M KOH	50
NiOOH/Ni_5P_4	40	290	NA	Ni foil	1.0 M KOH	53
Co-NC@Mo_2C	61	347	NA	Glassy carbon	1.0 M KOH	56
Ni:Co_3S_4	65	293	NA	Ni foam	1.0 M KOH	57
Ni/Mo_2C-PC	NA	368	1.50	Glassy carbon	1.0 M KOH	59
Porous MoO_2	54	260	1.43	Ni foam	1.0 M KOH	60
$Co(OH)_2$/BP 5:1	57	276	NA	Glassy carbon	1.0 M KOH	61
Co-P film	47	345	1.53	Cu foil	1.0 M KOH	62
Porous Co_3O_4	25	~400	NA	Glassy carbon	1.0 M KOH	63
$NiCo_2O_4$	90	420	1.52	FTO	1.0 M KOH	64
CoP Hollow Polyhedrons	57	400	1.53	Glassy carbon	1.0 M KOH	65
NiFe@NC	NA	~300	~1.50	Glassy carbon	1.0 M KOH	66

The OER activities of the catalysts were evaluated under the same three-electrode electrolysis set-up system. The polarization curves of these catalysts in **Figure 6.13d** indicate that the overpotential of S-CoO_x/NF catalyst was 370 mV when the current density is 100 mA cm^{-2}, which was much lower than the 450 mV of the prepared CoO_x/NF. Moreover, the catalytic activity of S-CoO_x/NF was also superior to that of commercial Ir/C (20 wt%) catalyst which was coated onto a nickel foam substrate (Ir/C/NF) (470 mV

overpotential at 100 mA cm^{-2}). As shown in **Figure 6.13e**, the corresponding Tafel slope of S-CoO_x/NF catalyst was 109 mV dec^{-1}, which was lower than 160 mV dec^{-1} for CoO_x/catalyst. This result indicates a promoted OER kinetics of S-CoO_x/NF. The

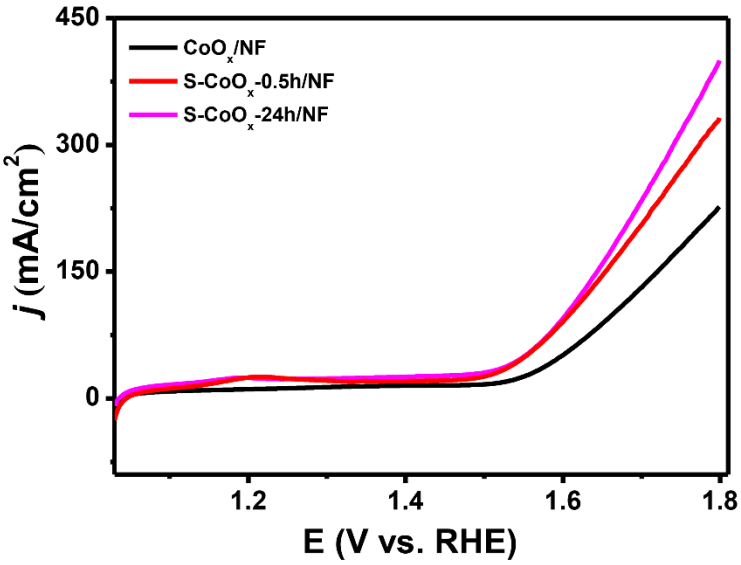

Figure 6.23 Polarization curves of CoO_x/NF, S-CoO_x-0.5h/NF and S-CoO_x-24h/NF, respectively, at 5 mV s^{-1} in 1.0 M KOH electrolyte.

polarization curves in **Figure 6.23** show that the control experiments including S-CoO_x-0.5h/NF and S-CoO_x-24h/NF experiments including S-CoO_x-0.5h/NF and S-CoO_x-24h/NF also demonstrate the enhanced OER activities compared with that of CoO_x/NF. During OER process, the stability factor is also very important. The stability of S-CoO_x/NF catalyst during OER was verified using the accelerated polarization curve cycling tests (1000 cycles) and the long-term chronoamperometry (*j*-t) curve (about 1200 min at the potential of 1.6 V) (**Figure 6.13f** and **Figure 6.24**). Besides, SEM images of S-CoO_x/NF catalyst used after long-term OER cyclic test show that no obvious changes in the morphology was observed (**Figure 6.25**). The longer long-term chronoamperometry curves of S-CoO_x/NF catalyst exhibit that no apparent current decay was observed after more than 80 h OER electrolysis

at a high current density (> 100 mA cm^{-2}) (**Figure 6.26**). The various postmortem characterizations including SEM images, XRD patterns, SEM mapping images and EDX patterns of S-CoO_x/NF confirm its superior stability (**Figure 6.27** and **6.28**). These features make S-CoO_x/NF one of the highly active OER electrocatalysts (**Table 6.3**).

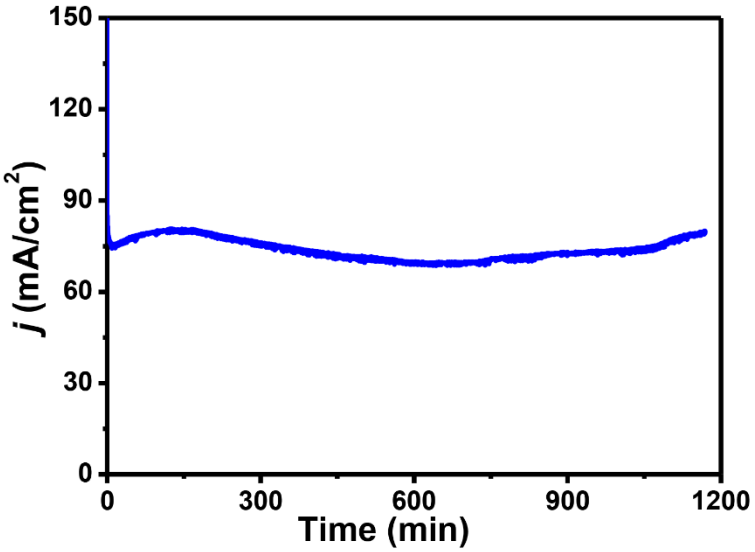

Figure 6.24 Chronoamperometry (*j*–t) curve of S-CoO_x/NF for the OER at the potential of 1.6 V.

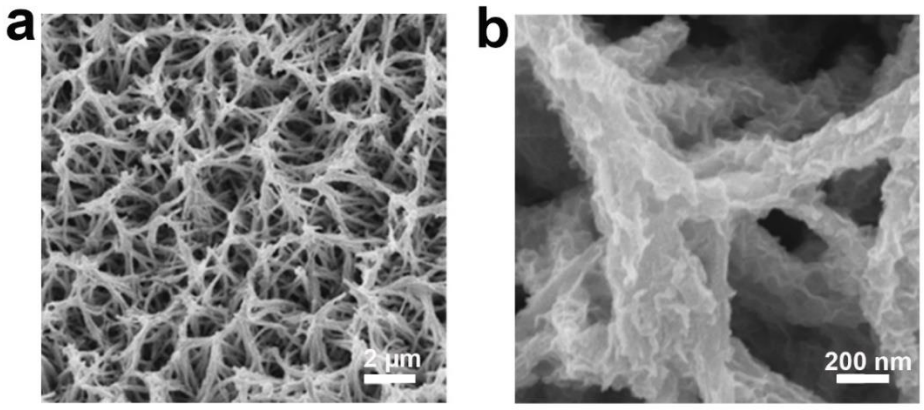

Figure 6.25 (a and b) SEM images of S-CoO_x/NF after long-term OER cyclic test in 1.0 M KOH electrolyte.

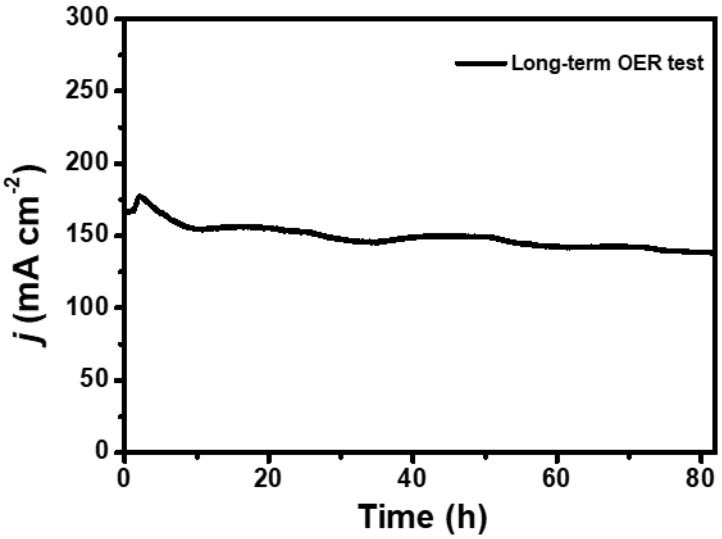

Figure 6.26 Chronoamperometry (*j*–t) curve of S-CoO_x/NF for the long-term OER electrolysis when the current density is about 150 mA cm^{-2} at the potential of 1.64 V.

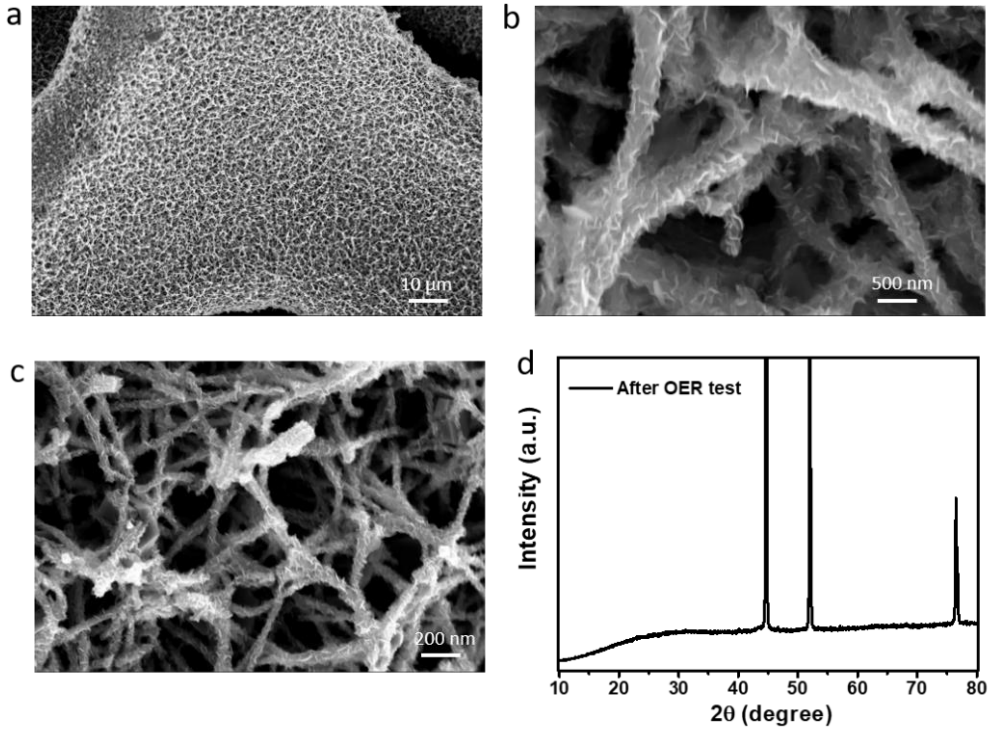

Figure 6.27 (a-c) SEM images and (d) XRD patterns of the S-CoO_x/NF after long-term OER electrolysis. The diffraction peaks in the XRD patterns is the peaks from the nickel foam substrate, no other peaks were formed.

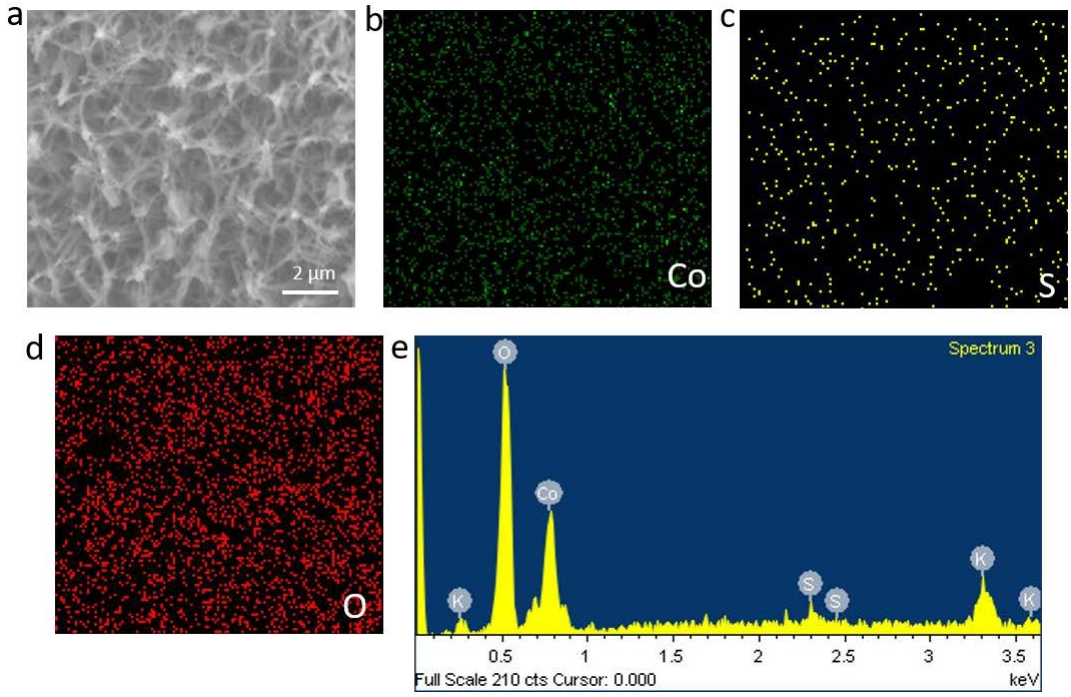

Figure 6.28 (a-d) SEM mapping images and (c) EDX patterns of the S-CoO_x/NF after long-term OER electrolysis.

6.3.4 Electrochemical Overall Water Splitting

An alkaline water electrolyser was assembled using S-CoO_x/NF as both the anode and the cathode (S-CoO_x//S-CoO_x) to evaluate the overall water splitting catalytic performance in 1 M KOH aqueous solution, the schematically illustration was as shown in **Figure 6.13g**. Polarization curves of the catalysts operated in two-electrode system was demonstrated in **Figure 6.13h**. The results show that the catalytic activities of S-CoO_x//S-CoO_x electrode exhibit a poor performance compared with the electrolyser assembled with benchmark Ir/C/NF and Pt/C/NF as the anode and the cathode (Ir/C//Pt/C) under low current densities. However, the catalytic performance of S-CoO_x//S-CoO_x becomes better than that of Ir/C//Pt/C when current density is higher (> 85 mA cm^{-2}). For examples, the required cell voltages for S-CoO_x//S-CoO_x were 1.85 V and 1.93 V, respectively, at the current densities

of 100 and 170 mA cm^{-2}. Under the same current density conditions, the higher cell voltages of 1.90 V and 2.13 V would be needed for Ir/C//Pt/C. Control experiments using S-CoO_x-0.5h/NF (or S-CoO_x-24h/NF) as the anode and the cathode, were named as S-CoO_x-0.5h // S-CoO_x-0.5h (or S-CoO_x-24h// S-CoO_x-24h). The polarization curves of the

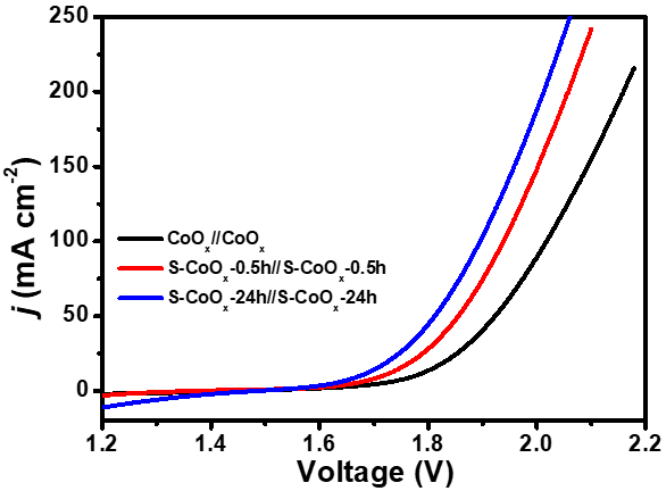

Figure 6.29 Polarization curve for overall water splitting during the control experiments in a two-electrode setup. Eletrolyte: 1 M KOH. Scan rate: 10 mV s^{-1}.

control experiments prove that the overall water splitting activities were enhanced after sulfur incorporation, using the electrolyzer made of CoO_x/NF as the anode and the cathode (CoO_x//CoO_x) as comparison (**Figure 6.29**). Stability is the crucial factor for the potential practical applications. The stability of S-CoO_x//S-CoO_x two-electrode system was confirmed via a long-term chronoamperometry test at the voltage of 1.6 V (~ 30 h) (**Figure 6.30**). Besides, there is also no obvious change of the EIS Nyquist plots before and after the long-term electrolysis, further proving its excellent stability (**Figure 6.31**). The water splitting performance of our alkaline electrolyser driven by S-CoO_x//S-CoO_x catalyst was very remarkable, which was also superior to the catalytic overall water splitting activities of

most previously reported literatures (**Figure 6.13i** and **Table 6.4**). Furthermore, the obtained samples also demonstrate the superior electrocatalytic activities in the neutral solution (**Figure 6.32).** We also prepared other cobalt sulfides such as Co-S as comparison, the results further prove that the enhanced catalytic performances on the structural disorder S-CoO_x catalyst (**Figure 6.33-6.36)**.

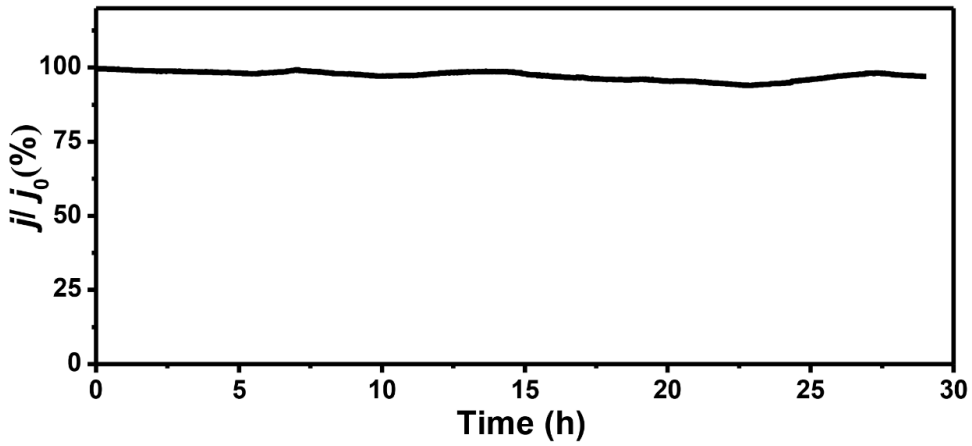

Figure 6.30 Chronoamperometry (*j*–t) curve using S-CoO_x/NF catalysts as both the anode and the cathode for the overall water splitting at the voltage of 1.6 V.

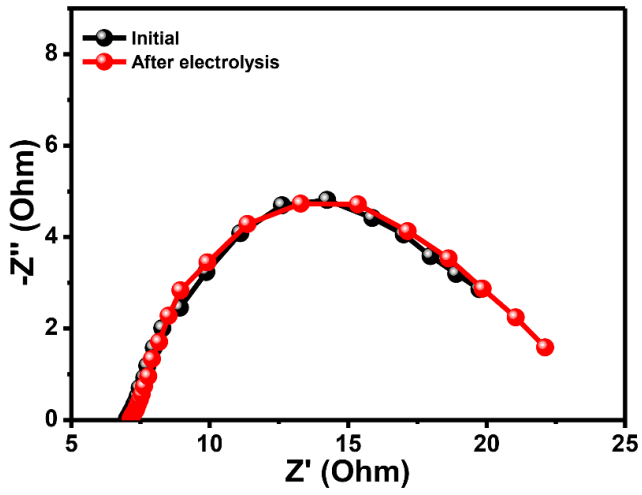

Figure 6.31 EIS Nyquist plots of S-CoO_x//S-CoO_x at the voltage of 1.75 V before and after long-term electrolysis during overall water splitting.

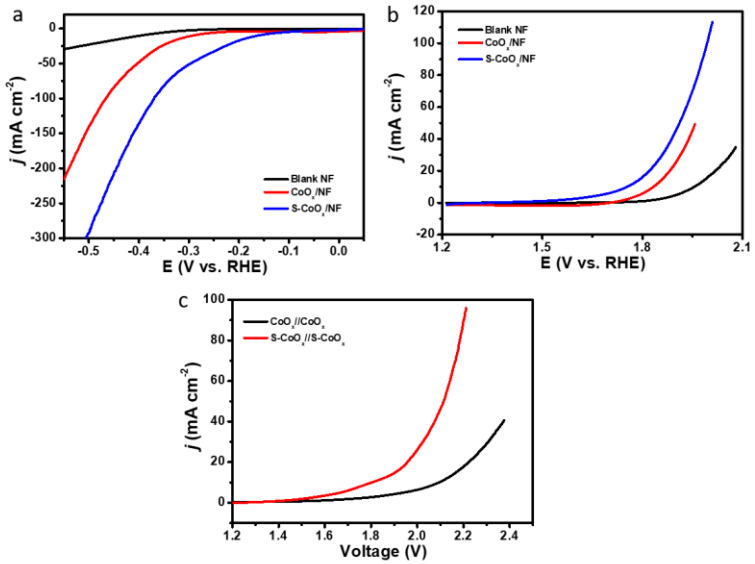

Figure 6.32 Electrocatalytic activities in the neutral solution (1M PBS). (a and b) Polarization curves of the prepared Co-S catalysts during (a) HER, (b) OER and (c) overall water splitting systems in the 1 M PBS (pH = 7.0) electrolyte. Scan rate is 10 mV s^{-1}.

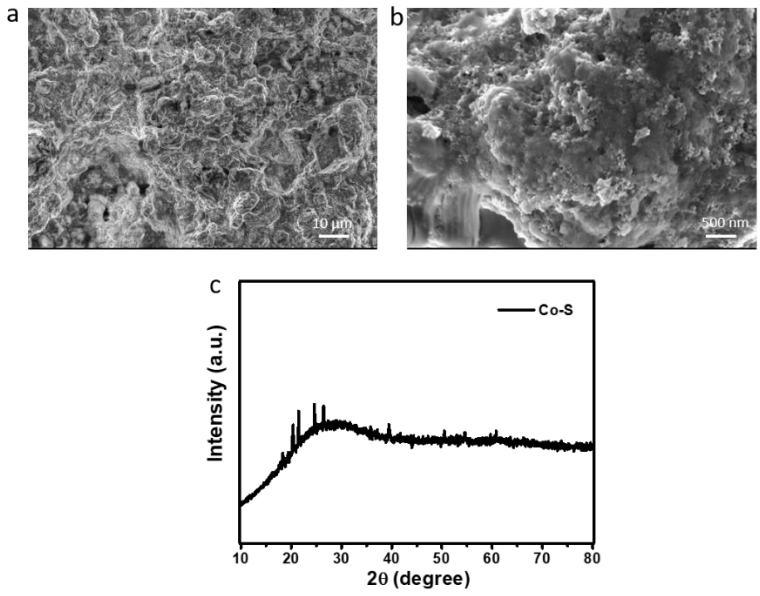

Figure 6.33 (a and b) SEM images and (c) XRD patterns of the prepared Co-S. The Co-S material was prepared via the direct reaction between the Co^{2+} and S^{2-} under aqueous solution. In details, the 7 mL 0.5 M $Co(NO_3)_2{\cdot}6H_2O$ aqueous solution was prepared, then 8 mL 0.5 M Na_2S aqueous solution was added at room temperature. After 30 min, the black product was collected.

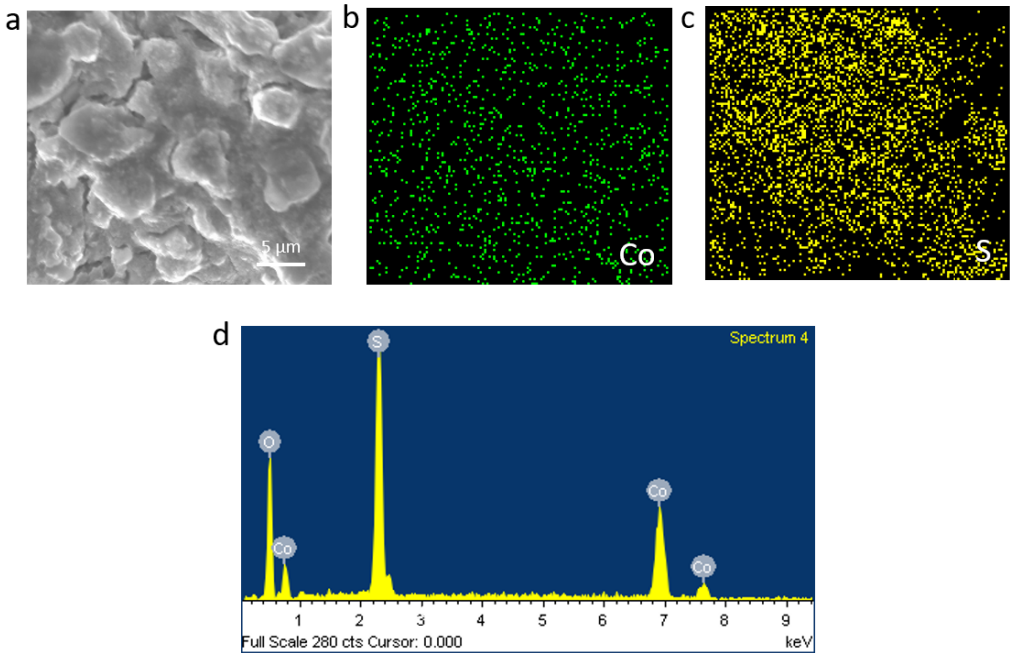

Figure 6.34 (a-c) SEM mapping images and (d) EDX patterns of the prepared Co-S.

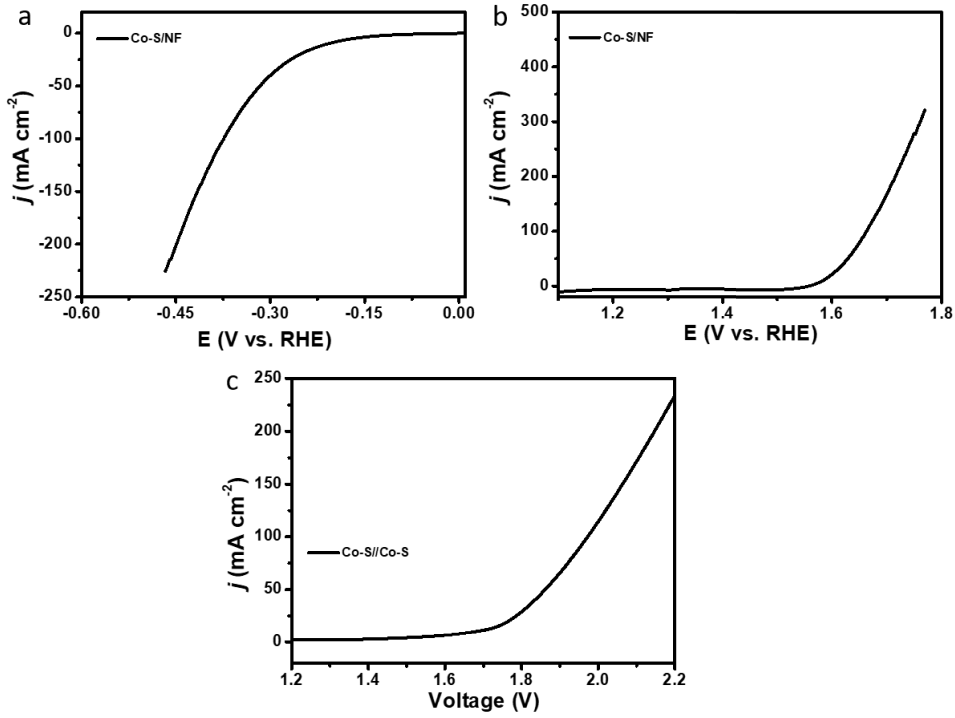

Figure 6.35 Electrocatalytic activities. (a and b) Polarization curves of the prepared Co-S catalysts for (a) HER, (b) OER and (c) overall water splitting activities in the 1 M KOH electrolyte. Scan rate is 10 mV s^{-1}.

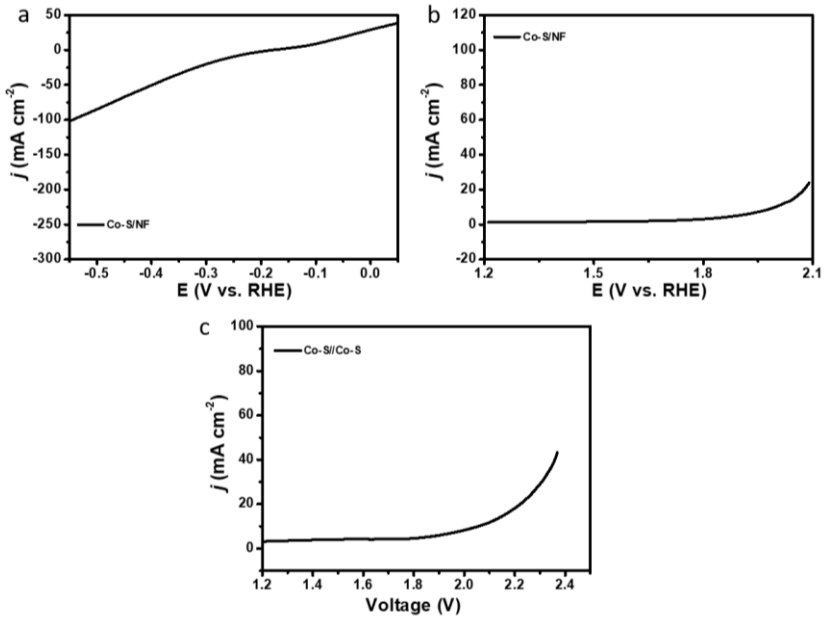

Figure 6.36 Electrocatalytic activities. (a and b) Polarization curves of the prepared Co-S catalysts for (a) HER, (b) OER and (c) overall water splitting activities in the 1 M PBS (pH = 7.0) electrolyte. Scan rate is 10 mV s^{-1}.

Table 6.4 Summary of recently reported bifunctional non-precious electrocatalysts for highly efficient catalytic overall water splitting in a two-electrode system.

Catalyst	Potential@10 mA cm^{-2} (V)	Substrate	Electrolyte	Reference
S-CoO_x//S-CoO_x	1.63	Ni foam	1.0 M KOH	This work
Co_3O_4-MTA//Co_3O_4-MTA	1.63	Ni foam	1.0 M KOH	39
CP/CTs/Co-S//CP/CTs/Co-S	1.74	Cabon paper	1.0 M KOH	46
$Ni(OH)_2$//$NiSe_2$	1.78	Carbon paper	1.0 M KOH	49
Co_1Mn_1CH//Co_1Mn_1CH	1.68	Ni foam	1.0 M KOH	51
Ni_5P_4//Ni_5P_4	<1.70	Ni foil	1.0 M KOH	53
Co-NC@Mo_2C//Co-NC@Mo_2C	1.685	Glassy carbon	1.0 M KOH	56
Ni:Co_3S_4//Co_3S_4	1.70	Ni foam	1.0 M KOH	57
Ni/Mo_2C-PC//Ni/Mo_2C-PC	1.66	Ni foam	1.0 M KOH	59
Co-P film//Co-P film	~ 1.64	Cu foil	1.0 M KOH	62
CoMnO@CN//CoMnO@CN	~ 1.52	Ni foam	1.0 M KOH	67

6.3.5 Theory Calculations

Density functional theory (DFT) calculations were performed to provide more insights about the influence of sulfur incorporation on the structure that leads to the enhanced

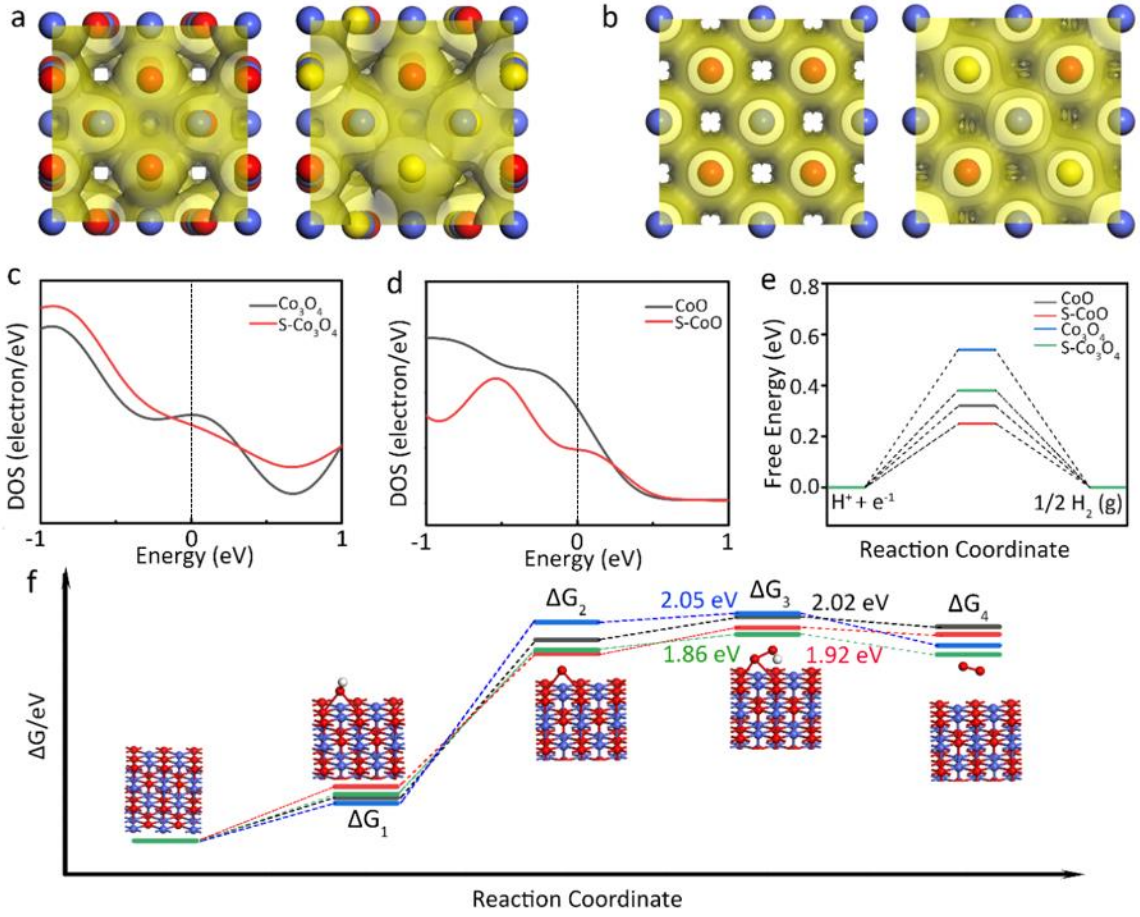

Figure 6.37 DFT calculations on S-CoO_x. (a) Calculated charge density distribution of Co_3O_4 (left) and S-Co_3O_4 (right) with (010) surface. (b) Calculated charge density distribution of CoO (left) and S-CoO (right) with (100) surface. (c and d) Calculated total densities of states of Co_3O_4, S-Co_3O_4 and CoO, S-CoO. (e) Free energy diagrams for hydrogen adsorption on (100) surface of Co_3O_4, S-Co_3O_4, CoO and S-CoO, respectively. (f) Gibbs free energy change diagrams of the OER process on surface of the Co_3O_4 (blue line), S-Co_3O_4 (green line), CoO (black line), S-CoO (red line) and the corresponding intermediates during each step. Co blue, O red, H white and S yellow.

Table 6.5 Gibbs free energy changes for the samples of the four steps revealed by DFT calculations. The unit is: eV.

System	ΔG1	ΔG2	ΔG3	ΔG4
CoO	0.39	1.81	2.02	1.93
S-CoO	0.49	1.69	1.92	1.86
Co_3O_4	0.34	1.97	2.05	1.76
S-Co_3O_4	0.42	1.72	1.86	1.68

electrochemical activities. Because the CoO_x was made of two phases including cubic CoO and cubic Co_3O_4, thus for the convenience of simulation, we chose the two constituents (cubic CoO and cubic Co_3O_4) to represent the prepared CoO_x. And the sulfur ion was incorporated into both cubic CoO and cubic Co_3O_4 to simulate the S-CoO_x. During surface adsorption calculations, a 2 x 2 x 3 supercell with (100) surface for CoO model and a 1 x 1 x 2 supercell with (010) surface for Co_3O_4 model were used along with a 20 Å vacuum. After S incorporation, a higher charge density of S-Co_3O_4 and S-CoO was achieved compared to Co_3O_4 and CoO, demonstrating the enhanced electron environment (**Figure 6.37a** and **Figure 6.37b**). The calculated density of states (DOS) show that the changed modulated electronic states of S-Co_3O_4 and S-CoO, compared with that of Co_3O_4 and CoO, are close to the Fermi level (**Figure 6.37c** and **Figure 6.37d**). In addition, the hydrogen adsorption Gibbs free energy (ΔG_H) was calculated to evaluate the HER activities. The values of ΔG_H were reduced by 0.07 eV for S-CoO, and 0.16 eV for S-Co_3O_4, revealing a modified HER energetics after S incorporation (**Figure 6.37e**).

Additionally, the Gibbs free energy changes (ΔG) during OER were also studied. During DFT calculation, the OER process includes four elementary steps (see details in Experimental Sections). Among them, the ΔG_3 is relevant to the formation of activated *OOH intermediates, and thus is the rate-determining step during the whole process (**Table 6.5**). As shown in **Figure 6.37f**, a reduced ΔG_3 of 0.19 eV and 0.1 eV are acquired compared to the pure models of Co_3O_4 and CoO after S incorporation, indicating that a more active *O was provided. According to the above calculations, the enhanced energetics for HER and the reduced Gibbs free energy change for OER were offered in the disordered S-CoO_x catalyst, therefore, resulting in high-efficiency electrochemical water splitting activities.

6.4 Conclusions

In summary, we have reported a unique structurally disordered S-CoO_x catalyst, which was synthesized via a facile room-temperature sulfur ion exchange method. After the electronegative sulfur incorporation, the long-range order of crystalline CoO_x has been distorted, which causes the modulated electron densities around Co atoms. The structural disorder in the formed S-CoO_x catalyst was found to bring more highly exposed active surface defect sites and increased low oxygen coordination. These merits enable the new disordered S-CoO_x to exhibit an outstanding catalytic activity and stability for both OER and HER in the alkaline electrolyte, substantially outperforming the catalytic performances of crystalline CoO_x. Besides, the electrolyzer made of S-CoO_x// S-CoO_x also shows the excellent overall water splitting catalytic activities. This work affords a direct and facile ion incorporation approach to tune the structure of catalysts for efficient water splitting and other energy conversion systems.

6.5 References

1. Kanan, M.W. and D.G. Nocera, *In situ formation of an oxygen-evolving catalyst in neutral water containing phosphate and Co^{2+}.* Science, 2008. **321**(5892): p. 1072-1075.

2. Li, F., et al., *Macroporous inverse opal-like Mo_XC with incorporated Mo vacancies for significantly enhanced hydrogen evolution.* Acs Nano, 2017. **11**(7): p. 7527-7533.

3. Yin, J., et al., *Oxygen vacancies dominated NiS_2/CoS_2 interface porous nanowires for portable Zn–air batteries driven water splitting devices.* Adv. Mater., 2017. **29**(47): p. 1704681.

4. Wang, H., et al., *Bifunctional non-noble metal oxide nanoparticle electrocatalysts through lithium-induced conversion for overall water splitting.* Nat. Commun., 2015. **6**: p. 7261.

5. Lu, C.B., et al., *Molybdenum carbide-embedded nitrogen-doped porous carbon nanosheets as electrocatalysts for water splitting in alkaline media.* Acs Nano, 2017. **11**(4): p. 3933-3942.

6. Luo, J., et al., *Water photolysis at 12.3% efficiency via perovskite photovoltaics and earth-abundant catalysts.* Science, 2014. **345**(6204): p. 1593-1596.

7. Jin, H., et al., *In situ cobalt–cobalt oxide/N-doped carbon hybrids as superior bifunctional electrocatalysts for hydrogen and oxygen evolution.* J. Am. Chem. Soc., 2015. **137**(7): p. 2688-2694.

8. Qin, J.-F., et al., *Facile synthesis of V-doped CoP nanoparticles as bifunctional electrocatalyst for efficient water splitting.* J. Energy Chem., 2019. **39**: p. 182-187.

9. You, B., et al., *Universal molecular-confined synthesis of interconnected porous metal oxides-NC frameworks for electrocatalytic water splitting.* Nano Energy, 2018. **48**: p. 600-606.

10. Wu, D., et al., *$Co(OH)_2$ nanoparticle-encapsulating conductive nanowires array: room-temperature electrochemical preparation for high-performance water oxidation electrocatalysis.* Adv. Mater., 2018. **30**(9): p. 1705366.

11. Ling, T., et al., *Activating cobalt(II) oxide nanorods for efficient electrocatalysis by strain engineering.* Nat. Commun., 2017. **8**: p. 1509.

12. Indra, A., et al., *Unification of catalytic water oxidation and oxygen reduction reactions: amorphous beat crystalline cobalt iron oxides.* J. Am. Chem. Soc., 2014. **136**(50): p. 17530-17536.

13. Zhang, R., et al., *Surface amorphization: a simple and effective strategy toward boosting the electrocatalytic activity for alkaline water oxidation.* ACS Sustainable Chem. Eng. , 2017. **5**(10): p. 8518-8522.

14. Zhang, L., et al., *Facilitating active species generation by amorphous NiFe-Bi layer formation on NiFe-LDH nanoarray for efficient electrocatalytic oxygen evolution at alkaline pH.* Chem. Eur. J., 2017. **23**(48): p. 11499-11503.

15. Ren, X., et al., *An amorphous $FeMoS_4$ nanorod array toward efficient hydrogen evolution electrocatalysis under neutral conditions.* Chem. Commun., 2017. **53**(64): p. 9000-9003.

16. Xie, M., et al., *An amorphous Co-carbonate-hydroxide nanowire array for efficient and durable oxygen evolution reaction in carbonate electrolytes.* Nanoscale, 2017. **9**(43): p. 16612-16615.

17. Lu, Z., et al., *Electrochemical tuning of layered lithium transition metal oxides for improvement of oxygen evolution reaction.* Nat. Commun., 2014. **5**: p. 4345.

18. Zhuang, L.Z., et al., *Ultrathin iron-cobalt oxide nanosheets with abundant oxygen vacancies for the oxygen evolution reaction.* Adv. Mater., 2017. **29**(17): p. 1606793.

19. Gao, J.J., et al., *Breaking long-range order in iridium oxide by alkali ion for efficient water oxidation.* J. Am. Chem. Soc., 2019, **141**(7): p. 3014–3023.

20. Rhodes, D., et al., *Disorder in van der Waals heterostructures of 2D materials.* Nat. Mater., 2019. **18**(6): p. 541.

21. Chattot, R., et al., *Surface distortion as a unifying concept and descriptor in oxygen reduction reaction electrocatalysis.* Nat. Mater., 2018. **17**(9): p. 827.

22. Xie, J., et al., *Controllable disorder engineering in oxygen-incorporated MoS_2 ultrathin nanosheets for efficient hydrogen evolution.* J. Am. Chem. Soc., 2013. **135**(47): p. 17881-17888.

23. Zheng, Y.R., et al., *Doping-induced structural phase transition in cobalt diselenide enables enhanced hydrogen evolution catalysis.* Nat. Commun., 2018. **9**: p. 2533.

24. Lukowski, M.A., et al., *Enhanced hydrogen evolution catalysis from chemically exfoliated metallic MoS_2 nanosheets.* J. Am. Chem. Soc., 2013. **135**(28): p. 10274-10277.

25. Clark, S.J., et al., *First principles methods using CASTEP.* Z. Kristallogr., 2005. **220**(5-6): p. 567-570.

26. Blochl, P.E., *Projector augmented-wave method.* Phys. Rev. B, 1994. **50**(24): p. 17953-17979.

27. Perdew, J.P. and W. Yue, *Accurate and simple density functional for the electronic exchange energy – Generalized gradient approximation.* Phys. Rev. B, 1986. **33**(12): p. 8800-8802.

28. Zhou, C., et al., *Construction of high-capacitance 3D CoO@polypyrrole nanowire array electrode for aqueous asymmetric supercapacitor.* Nano Lett., 2013. **13**(5): p. 2078-2085.

29. Wang, H.F., et al., *Bifunctional transition metal hydroxysulfides: Room-temperature sulfurization and their applications in Zn-Air batteries.* Adv. Mater., 2017. **29**(35): p. 1702327.

30. Wang, J.B., et al., *Raman study of N^+-implanted ZnO.* Appl. Phys. Lett., 2006. **88**(10): p. 101913.

31. Wang, Q., et al., *Oxysulfide photocatalyst for visible-light-driven overall water splitting.* Nat. Mater., 2019. **18**: p. 827-832.

32. Kim, H., et al., *Highly reversible Co_3O_4/graphene hybrid anode for lithium rechargeable batteries.* Carbon, 2011. **49**(1): p. 326-332.

33. Ma, L.T., et al., *Initiating a mild aqueous electrolyte Co_3O_4/Zn battery with 2.2 V-high voltage and 5000-cycle lifespan by a Co(III) rich-electrode.* Energy Environ. Sci., 2018. **11**(9): p. 2521-2530.

34. Xu, C.Y., P.X. Zhang, and L. Yan, *Blue shift of Raman peak from coated TiO_2 nanoparticles.* J. Raman Spectrosc., 2001. **32**(10): p. 862-865.

35. Ye, J.D., et al., *Raman study of lattice dynamic behaviors in phosphorus-doped ZnO films.* Appl. Phys. Lett., 2006. **88**(10): p. 101905.

36. Wang, Q., et al., *Oxysulfide photocatalyst for visible-light-driven overall water splitting.* Nat. Mater., 2019. **18**: p. 827-832.

37. Dou, Y.H., et al., *Graphene-like holey Co_3O_4 nanosheets as a highly efficient catalyst for oxygen evolution reaction.* Nano Energy, 2016. **30**: p. 267-275.

38. Yang, X.L., et al., *Highly acid-durable carbon coated Co_3O_4 nanoarrays as efficient oxygen evolution electrocatalysts.* Nano Energy, 2016. **25**: p. 42-50.

39. Zhu, Y.P., et al., *Self-templating synthesis of hollow Co_3O_4 microtube arrays for highly efficient water electrolysis.* Angew. Chem., Int. Ed., 2017. **56**(5): p. 1324-1328.

40. Zhang, Z. and J.T. Yates, *Band bending in semiconductors: Chemical and physical consequences at surfaces and interfaces.* Chem. Rev., 2012. **112**(10): p. 5520-5551.

41. Marco, J., et al., *Characterization of the nickel cobaltite, $NiCo_2O_4$, prepared by several methods: an XRD, XANES, EXAFS, and XPS study.* J. Solid State Chem., 2000. **153**(1): p. 74-81.

42. Yu, Z.Y., et al., *Ni-Mo-O nanorod-derived composite catalysts for efficient alkaline water-to-hydrogen conversion via urea electrolysis.* Energ. Environ. Sci., 2018. **11**(7): p. 1890-1897.

43. Chen, P.Z., et al., *3D nitrogen-anion-decorated nickel sulfides for highly efficient overall water splitting.* Adv. Mater., 2017. **29**(30): p. 1701584.

44. Guo, P., et al., *CoS nanosheet arrays grown on nickel foam as an excellent OER catalyst.* J. Alloy. Compd., 2017. **723**: p. 772-778.

45. Qiu, L.M. and G.T. Xu, *Peak overlaps and corresponding solutions in the X-ray photoelectron spectroscopic study of hydrodesulfurization catalysts.* Appl. Surf. Sci., 2010. **256**(11): p. 3413-3417.

46. Wang, J., et al., *Integrated three-dimensional carbon paper/carbon tubes/cobalt-sulfide sheets as an efficient electrode for overall water splitting.* Acs Nano 2016, **10**: p. 2342-2348.

47. Xiao, P., et al., *Molybdenum phosphide as an efficient electrocatalyst for the hydrogen evolution reaction*, Energy Environ. Sci. 2014, **7**: p. 2624-2629.

48. Zhao, X. J., et al., *Bifunctional electrocatalysts for overall water splitting from an iron/nickel-based bimetallic metal-organic framework/dicyandiamide composite*, Angew. Chem. Int. Ed. 2018, **57**: p. 8921-8926.

49. Liang, H. F., et al., *Porous two-dimensional nanosheets converted from layered double hydroxides and their applications in electrocatalytic water splitting*, Chem. Mater. 2015, **27**: p. 5702-5711.

50. Jin, H. Y., et al., *In situ cobalt-cobalt oxide/N-doped carbon hybrids as superior bifunctional electrocatalysts for hydrogen and oxygen evolution*, J. Am. Chem. Soc. 2015, **137**: p. 2688-2694.

51. Tang, T., et al., *Electronic and morphological dual modulation of cobalt carbonate hydroxides by Mn doping toward highly efficient and stable bifunctional electrocatalysts for overall water splitting*, J. Am. Chem. Soc. 2017, **139**: p. 8320-8328.

52. Feng, L. L., et al., *High-index faceted Ni_3S_2 nanosheet arrays as highly active and ultrastable electrocatalysts for water splitting*, J. Am. Chem. Soc. 2015, **137**: p. 14023-14026.

53. Ledendecker, M., et al., *The synthesis of nanostructured Ni_5P_4 films and their use as a non-noble bifunctional electrocatalyst for full water splitting*, Angew. Chem. Int. Ed. 2015, **54**: p. 12361-12365.

54. Zou, X. X., et al., *Cobalt-embedded nitrogen-rich carbon nanotubes efficiently catalyze hydrogen evolution reaction at all pH values*, Angew. Chem. Int. Ed. 2014, **53**: p. 4372-4376.

55. Song, J. H., et al., *Bimetallic cobalt-based phosphide zeolitic imidazolate framework: CoP_x phase-dependent electrical conductivity and hydrogen atom adsorption energy for efficient overall water splitting*, Adv. Energy Mater. 2017, **7**: p. 1601555.

56. Liang, Q. R., et al., *Metal-organic frameworks derived reverse-encapsulation Co-NC@Mo_2C complex for efficient overall water splitting*, Nano Energy 2019, **57**: p. 746-752.

57. Tang, S. S., et al., *Combining Co_3S_4 and Ni:Co_3S_4 nanowires as efficient catalysts for overall water splitting: an experimental and theoretical study*, Nanoscale 2019, **11**: p. 2202-2210.

58. Zhang, J., et al., *Engineering water dissociation sites in MoS_2 nanosheets for accelerated electrocatalytic hydrogen production*, Energy Environ. Sci. 2016, **9**: p. 2789-2793.

59. Yu, Z. Y., et al., *A one-dimensional porous carbon-supported Ni/Mo_2C dual catalyst for efficient water splitting*, Chem. Sci. 2017, **8**: p. 968-973.

60. Jin, Y. S., et al., *Porous MoO_2 Nanosheets as Non-noble Bifunctional Electrocatalysts for Overall Water Splitting*, Adv. Mater. 2016, **28**: p. 3785-3790.

61. Li, Y. J., et al., *Cobalt hydroxide-black phosphorus nanosheets: A superior electrocatalyst for electrochemical oxygen evolution*, Electrochimica Acta 2019, **297**: p. 40-45.

62. Jiang, N., et al., *Electrodeposited cobalt-phosphorous-derived films as competent bifunctional catalysts for overall water splitting*, Angew. Chem. Int. Ed. 2015, **54**: p. 6251-6254.

63. Sun, Y. F., et al., *Atomically-thin non-layered cobalt oxide porous sheets for highly efficient oxygen-evolving electrocatalysts*, Chem. Sci. 2014, **5**: p. 3976-3982.

64. Yu, X. X., et al., *Direct growth of porous crystalline $NiCo_2O_4$ nanowire arrays on a conductive electrode for high-performance electrocatalytic water oxidation*, J. Mater. Chem. A 2014, **2**: p. 20823-20831.

65. Liu, M. J., Li, J. H., *Cobalt phosphide hollow polyhedron as efficient bifunctional electrocatalysts for the evolution reaction of hydrogen and oxygen*, Acs Appl. Mater. Interfaces 2016, **8**: p. 2158-2165.

66. Zhang, Z. P., et al., *One-step conversion from Ni/Fe polyphthalocyanine to N-doped carbon supported Ni-Fe nanoparticles for highly efficient water splitting*, Nano Energy 2016, **30**: p. 426-433.

67. Li, J., et al., *Nanoparticle superlattices as efficient bifunctional electrocatalysts for water splitting*, J. Am. Chem. Soc. 2015, **137**: p. 14305-14312.

Chapter 7 Conclusions and Future Perspective

7.1 Conclusions

7.1.1 The Design of "Superaerophobic" Nickel Phosphide Nanoarray Structure

The unique "superaerophobic" nickel phosphide nanoarrays were prepared using a facile hydrothermal-then-annealing method. The simple nanowire array structure was achieved via the direct reaction of diammonium hydrogen phosphate and nickel foam during a hydrothermal process. Then during another hydrothermal process, the reaction solution was KOH aqueous solution. The morphology transformation happens from the smooth nanowire arrays to the unique hybrid structural architectures with the nanowires as the second frame, and nanosheets were evenly distributed on the nanowire arrays. Simultaneously, the hexagonal nickel hydroxide (JCPDS 14-0117) was successfully achieved when the hydrothermal temperature was higher.

Afterwards, the unique nickel phosphide materials were prepared during a facile phosphorization annealing strategy. The ingredients include: the optimized nickel hydroxide which was obtained at 120 ^{o}C and chemicals sodium hypophosphite monohydrate ($NaH_2PO_2 \cdot H_2O$). During the annealing process, the formed PH_3 was used to enable the transformation from hexagonal $Ni(OH)_2$ to hexagonal Ni_2P (JCPDS 03-0953) under the inert atmosphere flowing argon. The morphology of Ni_2P was totally inherited from the nanoarray structure of $Ni(OH)_2$. SAED patterns further verify the crystalline form changed from single crystal like feature in $Ni(OH)_2$ to the polycrystalline form of Ni_2P. Contact angle methodology demonstrates that the unique "superaerophobic" peculiarity of Ni_2P nanoarray structure. The hydrogen bubbles were easily and extremely fast released

from the surface of Ni_2P materials while the hydrogen bubbles were effortlessly absorbed onto the surface when using the blank nickel foam as comparison. The "superaerophobic" property was crucial and necessary to exclude the in-situ hydrogen bubbles during electrochemical water splitting system, especially at the high current densities.

7.1.2 "Superaerophobic" nickel phosphide nanoarray catalysts for hydrogen generation at large current densities

This work focuses on the application of the "superaerophobic" nickel phosphide in the area of electrochemical water splitting producing hydrogen at large current densities to meet the requirement of the hydrogen energy industrialization. A standard three-electrode system was employed to evaluate the electrochemical hydrogen evolution, with KOH aqueous solution as the alkaline electrolyte. To provide a much more indicative view of the HER properties, the commercial Pt/C (20 wt%) catalyst was chosen as comparison. The unique structure of Ni_2P/NF catalyst displays an inferior activity compared to the Pt/C catalyst when the current density is low (such as at the current density of 100 mA cm^{-2}). The phenomena could be attributed to the excellent intrinsic catalytic property of noble metal platinum. However, the situation altered fundamentally at the high current densities. When the current densities were 1000 mA cm^{-2} or 1500 mA cm^{-2}, the required overpotentials for Ni_2P/NF were 306 mV and 368 mV, respectively. While, the needed overpotentials for Pt/C/NF were 575 mV and 758 mV. This shift could not be independent from the unique "superaerophobic" morphology structure of the Ni_2P/NF catalyst, which can effectively release the in-situ generated hydrogen bubbles, ensuring the continuous contact interface between the electrolyte and the catalysts.

To further verify our conjecture and build a simulated industrial equipment, a lab-made two-electrode system was established. The two-electrode system consisting of the commercial noble metal Ir/C (20 wt%) and Pt/C (Pt/C||Ir/C) as the anode and cathode, respectively, was selected to be the systematic comparison. Our self-made Ni_2P/NF was as the cathode and the as-synthesized Ni-Fe LDH was used as the anode (Ni_2P||Ni-Fe LDH). The electrochemical performance tendency of the two-electrode system is similar with the above HER activities. At the low voltages (such as 1.7 V), the noble metal combination of Pt/C||Ir/C exhibits a superior catalytic activity than the self-made Ni_2P||Ni-Fe LDH combination, which also could be resulted from the active intrinsic nature of the noble metals. Meanwhile, a swift reverse happens at high current densities. The Ni_2P||Ni-Fe LDH combination gradually overwhelms the noble metal combination Pt/C||Ir/C when the current densities were > 600 mA cm^{-2}. The violently choppy electrochemical curve of the Pt/C||Ir/C catalyst further indicates the inferior solid-liquid contact interface due to the "bubble effect" causing by the pinned hydrogen bubbles on the catalyst surface. These phenomena uncover the huge potential of the design of "superaerophobic" structure to enable large-scale hydrogen generation at high current densities.

7.1.3 Sulfur-induced disordered cobalt oxide nanostructure for highly efficient water splitting

The development of water splitting electrolyzers was suffocated by the high cell voltage (1.8-2.0 V) requirement. Highly active bifunctional non-noble catalysts for both OER and HER as the key to proceed overall water splitting system has attracted the researchers' attention. Among them, transition metal oxides are the most promising bifunctional alternatives. However, the crystalline transition metal oxides were suffering from their

limited catalytic capability. In this work, crystalline cobalt oxide was chosen to be further investigated. To boost its intrinsic catalytic activities, the electronegative sulfur was incorporated into the crystalline cobalt oxide to form a structural disordered S-CoO_x via a facile sulfur ion exchange strategy with the usage of Na_2S aqueous solution at room temperature. In the disordered S-CoO_x, the high crystalline form of cobalt oxide was destroyed and the long-range lattice arrangement was changed into disorganized state. This disordered structure also brings more defect sites and more active oxygen coordination, which were preferable to the electrochemical water splitting system.

The electrochemical HER and OER activities were checked in a three-electrode system under alkaline condition. HER activities demonstrate that a superior catalytic activity was obtained via using S-CoO_x/NF catalyst, the overpotential of S-CoO_x/NF was 136 mV, much lower than the 313 mV for the crystalline CoO_x/NF at the current density of 10 mA cm^{-2}. Besides, the OER activities of S-CoO_x/NF catalyst show that the overpotential of S-CoO_x/NF was 370 mV at the current density of 100 mA cm^{-2}, which was also lower than 450 mV of crystalline CoO_x/NF catalyst. These results indicate that the promoted HER properties and facilitated OER activities for S-CoO_x/NF catalyst, which could be caused by the highly active disordered structure in S-CoO_x. To examine the overall water splitting properties, an alkaline water electrolyser consisting of S-CoO_x/NF as the anode and cathode (S-CoO_x//S-CoO_x) was built via a two-electrode device. The noble metal commercial Ir/C and Pt/C catalysts were used as the anode and the cathode (Ir/C//Pt/C) to be the benchmark. The catalytic activities of S-CoO_x//S-CoO_x were superior than the noble metal combination Ir/C//Pt/C at the high current densities > 85 mA cm^{-2}. For example, at the current densities of 100 and 170 mA cm^{-2}, the needed voltages for S-CoO_x//S-CoO_x were 1.85 V and 1.93 V,

much lower than 1.90 V and 2.13 V for Ir/C//Pt/C, respectively. The enhanced catalytic properties could be ascribed to the disordered structure. DFT calculation further reveal a beneficial electronic state was provided in the structural disordered S-CoO_x catalyst. These features work together to ensure the S-CoO_x the excellent catalytic performance. This work highlights an accessible path to tune the crystalline structure electrocatalysts to more disordered state, forming preferable water splitting systems.

7.2 Future Perspective

In this thesis, during the project of the synthesis for "superaerophobic" nickel phosphide, we developed a self-reaction method which directly reacted between $(NH_4)_2HPO_4$ and nickel foam to prepare the precursor with a nanowire array architecture. This self-reaction product has tighter connectivity with the substrate and usually shows an excellent stability. This method could be broadened to the preparation of other highly active nanomaterials. For example, we had also tried to realize the direct reaction between sulfur sources and the nickel foam substrate or copper substrate, the prepared transition metal sulfides also exhibit highly efficient catalytic HER in alkaline electrolyte. Besides, the self-reaction precursor could be used as the "second substrate" to form a more complex structure or morphology, resulting in the more flexible and diversified properties. Furthermore, the facile annealing phosphorization approach could also be extended for the development of other transition metal phosphides, such as copper phosphide, iron phosphide or other morphologies of nickel phosphide. The obtained transition metal phosphides could be applied in various fields.

Since 2014, Sun's group reported that nanoporous cobalt phosphide catalysts show huge potential in the area of efficient hydrogen-evolving cathode. Various transition metal phosphides were investigated for hydrogen generation. However, it is still a big challenge to realize the large-scale hydrogen production. Chapter four provides a desirable catalyst design to achieve high current densities to proceed the practical applications of hydrogen energy sources with the usage of "superaerophobic" nickel phosphide. Nickel phosphide has the active intrinsic catalytic property, and the "superaerophobic" morphology structure can maintain its catalytic activities with the rapid release of the in-situ produced hydrogen bubbles at high current densities. This "superaerophobic" surface design demonstrates a promising approach to accelerate hydrogen production industrialization, and it should be remarkable that the studies of "superaerophobic" surface and bubble release could be extended to other gas generation fields. However, how to achieve a proper "superaerophobic" structure and the actual features of "superaerophobic" catalysts during the electrochemical systems still need more efforts to investigate.

During the doctoral study, another project affords a facile strategy to induce the electronegative sulfur into the crystalline cobalt oxide via a sulfur ion exchange method at room temperature, forming a disordered structure in S-CoO_x. This project opens an effortless approach to transform from crystalline state to the disordered form. However, the optimization of the disordered structure was still difficult to control. The uniform distribution of the induced ion exchange and the internal transition process was also crucial and challenging to solve. Thus, we plan to pay more attention focusing on the internal analysis and exploration in the design of the highly effective non-noble electrocatalysts during the future.

APPENDIX: NOMENCLATURE

Abbreviations/Symbols	Full name
a.u.	Arbitrary unit
Ar	Argon
NF	Nickel foam
3D	Three-dimensional
AEL	Alkaline electrolyzer
PEMEL	Proton exchange membrane electrolyzer
HEMEL	Hydroxide exchange membrane electrolyzer
OER	Oxygen evolution reaction
HER	Hydrogen evolution reaction
ORR	Oxygen reduction reaction
DI	de-ionized
CV	Cyclic Voltammetry
FESEM	Field-Emission Scanning Electron Microscopy
g	Gram
mg	Milligram
m	Meter
m^2	Square meter
cm	Centimeter
cm^2	Square centimeter
Hz	Hertz

j	Current density
JCPDS	Joint Committee on Powder Diffraction Standards
M	Molar concentration
mA cm^{-2}	Milliampere per square centimeter
h	Hour
min	minute
μm	Micrometer
nm	Nanometer
C_{dl}	Double-layer capacitances
EIS	Electrochemical Impedance Spectroscopy
R_{ct}	Charge transfer resistance
XPS	X-ray photoelectron spectroscopy
EDX	Energy dispersive X-ray
SAED	Selected area electron diffraction
SEM	Scanning electron microscopy
TEM	Transmission electron microscopy
STEM	Scanning transmission electron microscopy
HRTEM	High-resolution transmission electron microscopy
BET	Brunauer-Emmett-Teller
XRD	X-ray diffraction
°	Degree
Ω	Ohm
℃	Degree Celsius